UNIVERSITÉ DE GENÈVE
Section de Physique
Department of Quantum Matter Physics

FACULTÉ DES SCIENCES
Professeur Dirk van der Marel

Possible phase transitions probed by infrared spectroscopy under high pressure: BiTeI and $Li_{0.9}Mo_6O_{17}$

THÈSE

présentée à la Faculté des Sciences de l'Université de Genève
pour obtenir le grade de docteur ès Sciences, mention Physique

par

Michaël Tran
de
Meyrin (Genève, Suisse)

Thèse n° XXX

GENÈVE
Atelier d'impression ReproMail
2014

Remerciements

Sera rempli lors de la prochaine version.

Résumé

Ce travail de thèse porte sur la spectroscopie optique dans le cas où l'échantillon se trouve dans une cellule de pression. Le chapitre 1 a valeur d'introduction sur la manière dont on réalise cette expérience. La mise en place de ce dispositif expérimental a permis l'étude de deux composés : BiTeI et $Li_{0.9}Mo_6O_{17}$.

Le chapitre 2 présente quelques points expérimentaux de spectroscopie optique ainsi que les méthodes d'analyse des données expérimentales en vue de la détermination de la conductivité optique. Cette dernière est déterminée à la fois, quantitativement par transformation Kramers-Kronig ou par analyse Drude-Lorentz de la réflectivité, mais aussi qualitativement, par l'inversion directe de la réflectivité et de la transmission par exemple. En particulier, la présence de l'enclume diamant lors des expériences à haute pression doit être prise en compte dans l'équation de Fresnel compliquant ainsi la détermination des propriétés optiques.

La conduite d'expériences optiques dans l'infrarouge, à basse température et à haute pression a nécessité le développement de deux dispositifs expérimentaux encore non présents parmi les dispositifs équipant le laboratoire du Prof. Dirk van der Marel. Ceux-ci sont basés sur un modèle commercial d'une cellule de haute pression Betsa utilisant des enclumes diamant et sont couplés à un spectromètre Bruker à transformation de Fourier opérant dans l'infrarouge. Ces dispositifs dédiés étant suffisamment compacts, ils ont pu être transportés à maintes reprises entre Genève et la ligne de lumière infrarouge du Paul Scherrer Institut (PSI). La description de ces dispositifs et de leur mode opératoire fait l'objet du chapitre 3.

Le chapitre 4 est consacré à l'étude optique sous pression du semi-conducteur BiTeI. En raison de l'absence de symétrie d'inversion dans sa structure, ce matériau présente un couplage spin-orbite qui lève la dégénérescence de spin de la dispersion énergétique. La structure de bande de type Rashba qui en résulte, présente alors la séparation de bandes la plus importante reportée pour un matériau tridimensionnel.

Les transitions prenant place dans cette structure de bande et le niveau de Fermi sont observables à travers l'étude de la conductivité optique qui présente notamment, une bande interdite de 0.4 eV. Par ailleurs, des travaux théoriques suggèrent que l'application d'une pression hydrostatique comprise entre 1.7 et 4.5 GPa induit une transition d'un état semi-conducteur vers un état isolant topologique avec une bande interdite inversée. Si notre étude montre bien une fermeture de la bande interdite induite par la pression, aucune réouverture n'est observée. Ces résultats mettent ainsi en avant la mise en défaut d'une condition nécessaire à la réalisation de la transition vers l'état isolant topologique. En effet, le calcul de la structure de bande prenant en compte les effets à $N-$corps et reproduisant de façon plus précise la largeur de la bande interdite, indique que la pression nécessaire pour réaliser cette transition est de l'ordre de 10 GPa. Or cette pression se situant au-delà d'une transition structurale à 9 GPa, également observée par d'autres techniques expérimentales, pourrait ne plus exister dans la nouvelle structure. D'autres études parvenant à la conclusion opposée, présentent néanmoins des disparités quant à la valeur de la pression critique à laquelle la bande interdite est fermée.

Le chapitre 5 est une étude optique sous pression du composé dit *Bronze violet de lithium*, de formule générale $Li_{0.9}Mo_6O_{17}$. Ce composé possède des propriétés de transport électroniques et optiques très anisotropes, la conduction s'effectuant majoritairement le long de chaînes en zigzag quasi unidimensionnelles (le long de l'axe b). C'est cette forte anisotropie qui rend ce matériau très intéressant pour la recherche de physique à une dimension, c.-à-d. les liquides de Tomonaga-Luttinger. La résistivité selon l'axe b du matériau présente une abrupte remontée à 25 K dont l'origine fait encore l'objet d'une controverse. Cette remontée disparaît sous l'application de pression au bénéfice d'une légère augmentation de la température critique de la phase supraconductrice. Le caractère quasi unidimensionnel du matériau et le fort potentiel d'emboîtement de sa surface de Fermi suggèrent la piste d'une instabilité du réseau accompagnée de l'ouverture d'une bande interdite. Cependant, une telle ouverture n'est pas observée en optique et aucune singularité n'est observée en susceptibilité magnétique, ce qui amène à considérer d'autres scénarios tels que la localisation des porteurs de charge ou un changement de dimensionnalité. Notre étude révèle une métallisation de la direction perpendiculaire à l'axe b concomitante avec une diminution de la conductivité optique de l'axe b. Cela met en avant la forte réduction du caractère anisotrope du matériau ainsi que l'existence de plusieurs transitions structurales. Ceci démontre que le matériau s'éloigne du régime quasi unidimensionnel prévalant à pression ambiante. L'absence d'étude structurale du composé en pression ne permet cependant pas d'évaluer le rôle des chaînes en zigzag dans les phases à haute pression.

Abstract

The present thesis work is focused on optical spectroscopy in the particular case where the sample is contained inside a pressure cell. Chapter 1 serves as an introduction on how such experiment is performed. The development of two experimental setups allowed to study two compounds: BiTeI and $Li_{0.9}Mo_6O_{17}$.

The chapter 2 presents some experimental elements of optical spectroscopy as well as the method of analysis of the data used to determine the optical conductivity. It can be determined either quantitatively by means of Kramers-Kronig transform or by Drude-Lorentz analysis of the reflectivity, or qualitatively by direct inversion of both reflectivity and transmission. The presence of the diamond anvil in the case of high pressure experiments must be taken into account within the Fresnel equation which complicates the determination of the optical properties.

Performing infrared spectroscopy at low temperature and high pressure required the development of two experimental setups because such apparatus were not available in the laboratory of Prof. Dirk van der Marel. These setups are based on a commercial high pressure diamond anvil cell from Betsa coupled to an infrared Fourier transform spectrometer from Bruker. Their rather small form factor allowed their frequent displacement at the infrared beamline of the Paul Scherrer Institut (PSI). The description of the two setups and their operating principle is the subject of chapter 3.

The chapter 4 covers the optical high pressure study of the BiTeI semiconductor. Due to the absence of inversion symmetry the material presents a spin-orbit coupling that lifts the spin degeneracy of the energy distribution. The resulting band structure shows the largest Rashba-type splitting observed for a bulk material. Transition occurring within the bands structure and the Fermi level are seen in the optical conductivity, which features an 0.4 eV energy gap. A theoretical work suggests that the application of an hydrostatic pressure lying in a 1.7-4.5 GPa window turns the material into a topological insulator with an inverted gap. Our study shows indeed

a pressure-induced gap closure which is however not followed by a gap re-opening. These results highlight that a necessary condition for the topological phase transition is not fulfilled. More over, band calculations taking into account many-body corrections, thus producing more actuate estimates of the energy gap, indicate that the pressure required to induce such transition is of the order of 10 GPa. This pressure actually lies above 9 GPa where a structural phase transition – experimentally observed by various techniques – occurs, thus possibly preventing the topological phase. Other studies present different conclusions without however agreeing on the value of the critical pressure at which the gap closes.

The chapter 5 is an optical study under pressure of the Lithium *purple bronze* compound, $Li_{0.9}Mo_6O_{17}$. The electronic transport and optical properties of this material exhibit a high anisotropy: the conduction mostly occurs through quasi one dimensional zig-zag chains along the b axis. Such a high anisotropy attracted much interest as the material offers a promising playground for the investigation of occurrence of one dimensional physics, i.e. Tomonaga-Luttinger liquids. The b axis resistivity shows an upturn at 25 K whose origin is controversial. This features is suppressed by the application of pressure which also slightly enhance the superconducting critical temperature. The one dimensional behavior of the material and its Fermi surface prone to nesting suggest the occurrence of a lattice instability leading to the opening of a charge (or spin) density wave gap. However, neither the opening of such gap in seen in optics nor any singularity in magnetic susceptibility, which leads to consider other scenarii such as charge carrier localization or dimensional crossover. Our study shows the metallization of the direction perpendicular to the b axis concomitant with a decrease of the b axis optical conductivity. The large anisotropy of the material is strongly suppressed by pressure which also revealed the occurrence of several structural phase transition. This demonstrates that the material is driven away from its quasi one dimensional behaviour at ambient pressure. The absence of structural study under high pressure makes the identification of the underling physics causing this dimensional change uneasy.

Contents

CHAPTER 1

Introduction

Mais qu'est ce que c'est que ce guet-apens ?
Hubert Bonisseur de La Bath,
OSS 117 dans "Rio Ne Répond Plus".

To fix the idea of the scale of pressure in said *high pressure* experiment, let us first recall that, at sea level, the ambient pressure due to our atmosphere is of *one* bar. Below ten meters of sea surface, a diver experiences two bars of pressure and near 11 kilometers below the surface, at the bottom of the deepest oceanic trench, the pressure is of almost 1100 bars, equivalent to 1.1 kbar, 0.11 GPa or 0.0011 megabar.

High pressure is nowadays reached in labs or factories and is put to use in various domains, ranging, by increasing pressure magnitude, from food and chemical industry to the earth and planetary sciences and, of course, passing by the condensed matter physics. The ends within these fields are extremely diverse and comprise for example sterilizing purposes in food processing, but also, more unexpectedly, stressless slaughter of live lobsters at ambient temperature in the multi-kilobar range that also results in impeccable shelling [1]. Geology, which has originally pushed the technique to reproduce the extreme pressure-temperature conditions reigning inside planets, aims at multiple megabar range at temperatures above several thousand degrees. Condensed matter physics is focused on the interactions occurring within the crystal structure of the materials and how they affect the material's properties. There the pressure ranges from the kilobar to (almost) megabar range, at low and high temperature.

The application of external hydrostatic pressure is, compared to chemical doping, a *clean* way to tune the interactions between atoms of the crystal since it does not

introduce impurities in the structure. Developments in the fields allowed the remote application (and determination thus control) of the pressure inside the apparatus thus unveiling an exceptional *knob* of the material's properties which ideally could be adjusted *in situ* while a single experiment is running. This seems to be a tremendous advantage over the lengthy systematic measurements campaigns undertaken on series of differently doped samples. Experiments under high pressure lead to a broad series of discoveries such as phase transition of the insulator to metal transition type, dimensionality crossover, pressure-induced superconductivity [2] and the measurement in mercury-based superconductor $HgBa_2Ca_2Cu_3O_{8+\delta}$ of the highest critical superconducting temperature to date, 164 K with the application of 31 GPa of pressure [3].

Optical spectroscopy is a well matured technique which allows to probe a very broad variety of excitations with energies lying within the Terahertz to the visible range such as magnetic excitations, superconducting gaps, optical phonons and electronic excitations (optical gaps, interband transitions, plasmas). Among the applications of the technique in condensed-matter physics are of course the measurement of pseudo-gap in the high-Tc superconductors, determination of electronic dynamics and observation of excitons within band gap.

Combining these two techniques allows to probe the material's new sets of excitations while its structure is strained. Such studies allowed for instance the observation of a dimensional crossover in $LaTiO_{3.14}$ [4], the metal-insulator transition in vanadium dioxide systems [5] and the observation of the shift of the plasma edge in organic superconductors [6] and many others. Such exemplary studies make desirable the availability to perform such kind of measurements in an infrared spectroscopy research group and eventually led prof. Dirk van der Marel to consider such project within his lab. The first traces of such diversification actually occur at the time of the PhD Thesis of Riccardo Tediosi [7] (partially) focused on a high-pressure study of Bismuth, using a setup and a pressure cell reaching 20 GPa at 25 K (piston-type pressure cell) and during which some initial designing was done in order to reach higher pressures with a different cell working in transmission geometry. The present work actually takes over the high pressure project with the combination of a diamond anvil cell reaching 20 GPa and a cryostat allowing to reach a lower temperature. This required the design and development of a whole new experimental setup compact enough so it could *reasonably frequently* be brought to the infrared synchrotron beamline of the Swiss Light Source (hosting the very same spectrometer as the one present in the lab of prof. Dirk van der Marel in Geneva). This is the subject of chapter 3. Eventually, a second setup working in reflection geometry and low temperature using the same high pressure cell was also built and allowed to extend the use of the setup to low temperature Raman spectroscopy. Subsequent (in principle) to experiment is the optical data analysis which for several reasons turned out to be *slightly* more difficult to carry out in comparison to ambient-pressure optical data. The disentanglement of the contribution of the physics taking place in the material and the contribution

inherent from the mechanical details of the experiment requires special attention and is discussed in chapter 2.

However, the constraints imposed by one technique are in opposition to those of the other technique, and this applies in particular to the size of the sample in the present case. Since by definition:

$$\text{Pressure} = \frac{\text{Force}}{\text{Surface}}$$

one could *in principle* for a given sample with a certain surface, *simply* apply the force required to reach the desired pressure. However, technical reasons limit the force one can apply with real materials, instead the size of the sample is reduced in order to reach the so desired high pressure. In optics, the size of the sample is also an important issue. On a pragmatic level, it is easier to detect the light that has interacted with a sample if the surface that was exposed to the spectrometer's incident light is large. On a more fundamental level, since the photon travels at a fixed velocity, its wavelength is linked to the photon's frequency (or equivalently energy):

$$\text{wavelength} = \frac{\text{speed of light}}{\text{energy}}$$

which indicates that if the energy of the incident light goes low enough (as it is often desired in infrared spectroscopy), its corresponding wavelength will reach a similar magnitude than the sample's dimension and interference effects appear; this is the diffraction limit. For instance, a frequency of 100 cm^{-1} amounts to a wavelength of 100 μm. Hence, to keep some *safety distance* from this limit, one should work with sample sizes at least three to five times greater than the wavelength.

Reconciliation between the contradictory requirements of these two techniques results of course in a number of compromises. For instance, the sample is still large enough (on the order of 0.1 mm) to be able to focus enough light on its surface, and yet small enough to fit into a pressure cell able to reach tens of GPa.

Instead of infrared, one might think of using higher energy photons in other optical spectroscopy techniques. Among the important differences between a sample at ambient condition and a sample inside a pressure cell is the presence of a window sitting on top of the sample's surface. Its very presence prevents by nature different kind of surface-sensitive experiments such as angle-resolved photoemission spectroscopy, ellipsometry and, for even more obvious reasons, scanning tunneling microscopy/spectroscopy. For instance, during ARPES measurements, the photo-electron capture occurring inside the sample renders the technique only surface-sensitive and requires an ultra-high vacuum environment around the sample to prevent further photo-electron capture, thus making (high) pressure studies impossible.

The first material presented in this work is the layered polar semiconductor BiTeI which attracted much attention in the past few years due to the prediction followed by the direct observation by ARPES of a Rashba spin-split band structure. Further

more, another prediction stated that by a modest application of $1.7 - 4.7$ GPa of hydrostatic pressure the material would turn from a semi-conductor into a topological insulator. Since ARPES cannot be used under high pressure, other ways of probing the material's band structure have to be employed to assess the pressure-induced topological properties. Since infrared spectroscopy is a bulk sensitive technique, it is not expected to be sensitive to the conducting surface states characteristic of a topological insulator. However, as electronic transitions occur within the band structure of the material with corresponding energies lying in the infrared, one can follow their evolution with pressure, and in particular, the one corresponding to the energy gap of the material which *has* to close and re-open under pressure. The fulfillment of such a necessary condition for a topological insulator scenario is investigated in chapter 4.

The second material investigated in this thesis is lithium molybdenum purple bronze, $Li_{0.9}Mo_6O_{17}$, which belongs to a broad family of material called *bronzes* due to their shiny appearance. It features extreme anisotropic transport properties and has therefore drawn much attention in the previous decades. It was unveiled that although the structure of the material is tridimensional the material's properties are much more reminiscent of a one-dimensional material where charge carriers are *locked* along (quasi) one dimensional chains. Physics occurring at low dimensions is intrinsically different from the one at higher dimensions. The single particle excitations celebrated in the Fermi liquid theory simply do not apply in one dimensional system. The predominance of strong interactions renders only collective excitations possible in the material. This system was therefore extensively investigated in search of manifestations of such exotic physics and substantial evidences were gathered, in particular in ARPES where the theoretically predicted spin-charge separation, power-law behavior and scaling properties were observed. This material features an upturn in its b-axis resistivity which is subject of a strong and long-lasting debate as to its origin and several (mutually excluding) scenarii are proposed. The strong influence of pressure on this upturn and the very strong anisotropy observed in optics motivates an infrared and high pressure study of this compound. This is the subject of chapter 5.

CHAPTER 2

Optical data analysis under pressure

Hâtez-vous lentement, et sans perdre courage,
Vingt fois sur le métier remettez votre ouvrage,
Polissez-le sans cesse, et le repolissez,
Ajoutez quelquefois, et souvent effacez.
Extrait du Chant I de "L'Art poétique" de Nicolas Boileau, 1674

The basics is the propagation of light in vacuum, matter and at interfaces. Therefore, at the beginning of this chapter, we will start by summarize the purpose-related essentials elements. For more details, refer to excellent electrodynamics/optics textbook such as [8, 9].

Then, we will present the main experimental techniques used in classical infrared spectroscopy at ambient pressure followed by different possibilities to extract information from the experimental data.

Last but certainly not least, we will describe the main experimental difference that working at high pressures implies regarding optical spectroscopic data and how it might affect the possible ways to extract meaningful information, i.e. optical conductivity.

In both ambient and high pressure cases, examples of spectra and results of analysis are discussed on the BiTeI compound.

2.1 Principles of electrodynamics

2.1.1 Maxwell's equations in vacuum and matter

The well-known four Maxwell's equations in vacuum for space and time-varying electric and magnetic fields $\mathbf{E}(\mathbf{r},t)$ and $\mathbf{B}(\mathbf{r},t)$ are in Gaussian units expressed as:

$$\nabla \cdot \mathbf{E}(\mathbf{r},t) = 4\pi\rho(\mathbf{r},t) \tag{2.1}$$

$$\nabla \cdot \mathbf{B}(\mathbf{r},t) = 0 \tag{2.2}$$

$$\nabla \times \mathbf{E}(\mathbf{r},t) = -\frac{1}{c}\frac{\partial \mathbf{B}(\mathbf{r},t)}{\partial t} \tag{2.3}$$

$$\nabla \times \mathbf{B}(\mathbf{r},t) = \frac{4\pi}{c}\mathbf{J}(\mathbf{r},t) + \frac{1}{c}\frac{\partial \mathbf{E}(\mathbf{r},t)}{\partial t} \tag{2.4}$$

where c is the speed of light in vacuum, ρ and $\mathbf{J}$ are the charge and current density respectively which include both external and induced charges and currents. In the special case of free space, where there is no charge nor current, one is left with gradient-less fields. Using the identity for any vector $\mathbf{Z}$:

$$\nabla \times (\nabla \times \mathbf{Z}) = -\nabla^2\mathbf{Z} + \nabla(\nabla \cdot \mathbf{Z}) \tag{2.5}$$

one takes the curl of (2.3) and (2.4) and obtains two differential equations

$$\nabla^2\mathbf{E}(\mathbf{r},t) = \frac{1}{c^2}\frac{\partial^2}{\partial t^2}\mathbf{E}(\mathbf{r},t) \qquad \nabla^2\mathbf{B}(\mathbf{r},t) = \frac{1}{c^2}\frac{\partial^2}{\partial t^2}\mathbf{B}(\mathbf{r},t) \tag{2.6}$$

which consist of two wave equations which can be solved with the harmonic wave Ansatz where for instance the electric fields has the form of

$$\mathbf{E}(\mathbf{r},t) = \mathbf{E}_0 e^{i(\mathbf{q}\cdot\mathbf{r}-\omega t)} \tag{2.7}$$

where the wavevector $\mathbf{q}$ indicates the direction of propagation of the wave in reciprocal space and ω its only oscillatory frequency. One sees more easily in reciprocal space that (2.7) combined with (2.3) constrains the electric and magnetic fields as:

$$\mathbf{B}(\mathbf{q},\omega) = \frac{c}{\omega}\mathbf{q} \times \mathbf{E}(\mathbf{q},\omega) \tag{2.8}$$

Such a linearly polarized electromagnetic wave is represented in fig. 2.1 where the propagation occurs along the $\mathbf{z}$ axis ($\mathbf{q} = \mathbf{z}$), electric field lies along $\mathbf{x}$ and magnetic field along $\mathbf{y}$.

To derive some of the more general properties from equations (2.1) to (2.4), one usually assumes the existence of a scalar $\Phi(\mathbf{r},t)$ and vector $\mathbf{A}(\mathbf{r},t)$ potentials such that

$$-\nabla\Phi(\mathbf{r},t) = \mathbf{E}(\mathbf{r},t) + \frac{1}{c}\frac{\partial \mathbf{A}(\mathbf{r},t)}{\partial t} \tag{2.9}$$

$$\nabla \times \mathbf{A}(\mathbf{r},t) = \mathbf{B}(\mathbf{r},t) \tag{2.10}$$

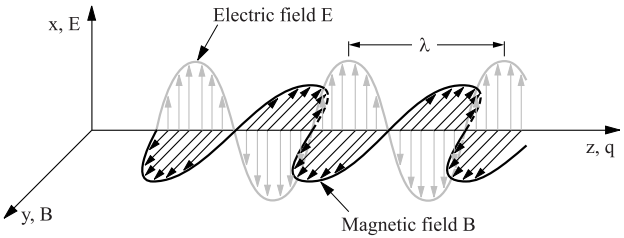

Figure 2.1 – Linearly polarized electromagnetic wave travelling in the **z** direction, from [8].

Taking the gradient of (2.9) to express (2.1) in terms of these new potentials gives:

$$\nabla \cdot \mathbf{E}(\mathbf{r},t) = 4\pi\rho = -\nabla^2\Phi(\mathbf{r},t) - \frac{1}{c}\frac{\partial}{\partial t}(\nabla \cdot \mathbf{A}(\mathbf{r},t)) \tag{2.11}$$

The so-called Coulomb gauge allows to cancel the last term on the right since it imposes a vector potential with no divergence:

$$\nabla \cdot \mathbf{A}(\mathbf{r},t) = 0 \tag{2.12}$$

and one ends-up with Poisson equation for the charge density

$$\nabla^2\Phi(\mathbf{r},t) = -4\pi\rho(\mathbf{r},t) \tag{2.13}$$

Taking the curl for a second time of (2.10) with (2.5) one finds that the curl of (2.4) can be written as function of the potentials $\Phi(\mathbf{r},t)$ and $\mathbf{A}(\mathbf{r},t)$ using (2.12), as:

$$\nabla^2\mathbf{A}(\mathbf{r},t) - \frac{1}{c^2}\frac{\partial^2\mathbf{A}(\mathbf{r},t)}{\partial t^2} = -\frac{4\pi}{c}\mathbf{J}(\mathbf{r},t) + \frac{1}{c}\nabla\frac{\partial\Phi(\mathbf{r},t)}{\partial t} \tag{2.14}$$

Inserting the time derivative of (2.9) and assuming a static electric field, one finds the analog of (2.13) for the current density:

$$\nabla^2\mathbf{A}(\mathbf{r},t) = -\frac{4\pi}{c}\mathbf{J}(\mathbf{r},t) \tag{2.15}$$

One can take the time derivative of (2.1) and inject the term of the electric field into the gradient of (2.4) to obtain

$$\nabla \cdot (\nabla \times \mathbf{B}(\mathbf{r},t)) = \frac{4\pi}{c}\nabla \cdot \mathbf{J}(\mathbf{r},t) + \frac{4\pi}{c}\frac{\partial\rho(\mathbf{r},t)}{\partial t} \tag{2.16}$$

Assuming that the all functions are twice continuously differentiable (as it is the case for the plane-wave Ansatz in (2.7)), the lefthand side simplifies to zero and hence the continuity equation linking the densities of charge and current:

$$\nabla \cdot \mathbf{J}(\mathbf{r},t) = -\frac{\partial\rho(\mathbf{r},t)}{\partial t} \tag{2.17}$$

which holds separately for both external or induced densities.

In the presence of matter, i.e. when the electromagnetic wave propagates into a medium, one has to account for the changes provoked by such phenomena such as polarization, magnetization and currents, one usually redefines the useful electromagnetic fields used as: the electric displacement field $\mathbf{D}$ instead of the electric field $\mathbf{E}$ and the magnetic field $\mathbf{H}$ instead of the magnetic induction field $\mathbf{B}$. The charge density in (2.1) has now two terms:

$$\rho(\mathbf{r},t) = \rho_{\text{ext}}(\mathbf{r},t) + \rho_{\text{pol}}(\mathbf{r},t) \tag{2.18}$$

the first accounts for charges forced into the material whereas the second accounts for the redistribution of bound charges into the material, i.e. polarization:

$$\rho_{\text{pol}}(\mathbf{r},t) = -\nabla \cdot \mathbf{P}(\mathbf{r},t) \tag{2.19}$$

In the case where no current is forced into the system, the current density also has two terms:

$$\mathbf{J}(\mathbf{r},t) = \mathbf{J}_{\text{cond}}(\mathbf{r},t) + \mathbf{J}_{\text{bound}}(\mathbf{r},t) \tag{2.20}$$

where the first term accounts for the displacement of charges due to the electric field $\mathbf{E}$ and could be rewritten as Ohm's law:

$$\mathbf{J}_{\text{cond}}(\mathbf{r},t) = \sigma_1 \mathbf{E}(\mathbf{r},t) \tag{2.21}$$

The seconds term of (2.20) regroups contributions coming from changes in polarization $\mathbf{P}(\mathbf{r},t)$ and magnetization $\mathbf{M}(\mathbf{r},t)$ of the system:

$$\mathbf{J}_{\text{bound}}(\mathbf{r},t) = \frac{\partial \mathbf{P}(\mathbf{r},t)}{\partial t} + c\nabla \times \mathbf{M}(\mathbf{r},t) \tag{2.22}$$

Inserting (2.18) and (2.20) into the first and last Maxwell's equation (2.1) and (2.4) gives:

$$\begin{aligned} \nabla \cdot \mathbf{E}(\mathbf{r},t) &= 4\pi \left(\rho_{\text{ext}}(\mathbf{r},t) - \nabla \cdot \mathbf{P}(\mathbf{r},t)\right) \\ \nabla \times \mathbf{B}(\mathbf{r},t) &= \frac{4\pi}{c}\left(\mathbf{J}_{\text{cond}}(\mathbf{r},t) + \frac{\partial \mathbf{P}(\mathbf{r},t)}{\partial t} + c\nabla \times \mathbf{M}(\mathbf{r},t)\right) + \frac{1}{c}\frac{\partial \mathbf{E}(\mathbf{r},t)}{\partial t} \end{aligned}$$

thus suggesting the form of the relations between $\mathbf{E}-\mathbf{B}$ fields and $\mathbf{D}-\mathbf{H}$ fields in the framework of linear response theory to retrieve the original structure of Maxwell's equations:

$$\mathbf{D}(\mathbf{r},t) = \epsilon_1 \mathbf{E}(\mathbf{r},t) = (1+4\pi\chi_e)\,\mathbf{E}(\mathbf{r},t) = \mathbf{E}(\mathbf{r},t) + 4\pi \mathbf{P}(\mathbf{r},t) \tag{2.23}$$

$$\mathbf{B}(\mathbf{r},t) = \mu_1 \mathbf{H}(\mathbf{r},t) = (1+4\pi\chi_m)\,\mathbf{H}(\mathbf{r},t) = \mathbf{H}(\mathbf{r},t) + 4\pi \mathbf{H}(\mathbf{r},t) \tag{2.24}$$

where ϵ_1 and μ_1 are called dielectric constant and magnetic permeability respectively and χ_e and χ_m are the dielectric and magnetic susceptibilities; ϵ_1, μ_1, χ_1 and χ_2 are

dimensionless quantities. With these expressions, (2.1-2.4) become:

$$\nabla \cdot \mathbf{D}(\mathbf{r},t) = 4\pi\rho_{\text{ext}}(\mathbf{r},t) \tag{2.25}$$
$$\nabla \cdot \mathbf{B}(\mathbf{r},t) = 0 \tag{2.26}$$
$$\nabla \times \mathbf{E}(\mathbf{r},t) = -\frac{1}{c}\frac{\partial \mathbf{B}(\mathbf{r},t)}{\partial t} \tag{2.27}$$
$$\nabla \times \mathbf{H}(\mathbf{r},t) = \frac{4\pi}{c}\mathbf{J}_{\text{cond}}(\mathbf{r},t) + \frac{1}{c}\frac{\partial \mathbf{D}(\mathbf{r},t)}{\partial t} \tag{2.28}$$

Using the plane wave Ansatz, the absence of external current, (2.23) and Ohm's law (2.22), the expression of (2.28) becomes

$$c\nabla \times \mathbf{H}(\mathbf{r},t) = 4\pi\sigma_1\mathbf{E}(\mathbf{r},t) - i\omega\epsilon_1\mathbf{E}(\mathbf{r},t) = -i\omega\tilde{\epsilon}\mathbf{E}(\mathbf{r},t) \tag{2.29}$$

where the complex dielectric function is defined as

$$\tilde{\epsilon} \equiv \epsilon_1 + i\frac{4\pi\sigma_1}{\omega} = \epsilon_1 + i\epsilon_2 \tag{2.30}$$

which in turns allows to define a more general Ohm's law where the conductivity $\tilde{\sigma}$ is also a complex quantity:

$$\tilde{\sigma} \equiv \sigma_1 + i\sigma_2 \tag{2.31}$$

and is related to $\tilde{\epsilon}$ with:

$$\tilde{\epsilon} \equiv 1 + \frac{4\pi i}{\omega}\tilde{\sigma}. \tag{2.32}$$

Now both these quantities are in general function of frequency ω and momentum $\mathbf{q}$ and constitute the properties of the material one aims to determine. Inside a medium one needs to work out the value taken by the wavenumber $\mathbf{q}$ introduced in (2.7) which is done by substituting the Ansatz into the Maxwell's equation expressed in reciprocal space and looking for the restrictions implied upon $\mathbf{q}$. If one defines the complex refractive index as

$$\tilde{n} = n_1 + in_2 \equiv \left(\epsilon_1\mu_1 + i\frac{4\pi\mu_1\sigma_1}{\omega}\right)^{1/2} = (\tilde{\epsilon}\mu_1)^{1/2} \tag{2.33}$$

one can write $\tilde{q}$, the magnitude of wavevector $\mathbf{q} = \tilde{q}\hat{\mathbf{q}}$, as:

$$\tilde{q} = \frac{\omega}{c}\tilde{n} = \frac{n_1\omega}{c} + i\frac{n_2\omega}{c} \tag{2.34}$$

where both components $n_{1,2}$ are real and defined as:

$$n_{1,2}^2 \equiv \frac{\mu_1}{2}\left(\sqrt{\epsilon_1^2 + \left(\frac{4\pi\sigma_1}{\omega}\right)^2} \pm \epsilon_1\right) \tag{2.35}$$

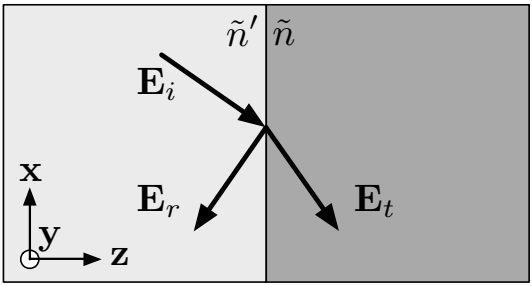

Figure 2.2 – Interface between two media in the $\mathbf{xy}$ plane where the arrows represent the $\mathbf{q}$ vector for each wave. $\mathbf{E}_i$, $\mathbf{E}_t$ and $\mathbf{E}_r$ are the incident, transmitted and reflected electric fields respectively. The magnetic fields $\mathbf{H}_i$, $\mathbf{H}_t$ and $\mathbf{H}_r$ are not represented but it is obvious that $\mathbf{H}_r$ will undergo a phase shift of π in order to stay perpendicular to $\mathbf{E}_r$.

with the properties

$$n_1^2 - n_2^2 = \epsilon_1 \mu_1 \tag{2.36}$$

$$2n_1 n_2 = \frac{4\pi\mu_1\sigma_1}{\omega} \tag{2.37}$$

Inserting (2.34) into the plane wave (2.7) and separating real and imaginary parts of the exponents one gets

$$\mathbf{E}(\mathbf{r}, t) = \mathbf{E}_0 e^{i\omega(\hat{\mathbf{q}}\cdot\mathbf{r}n_1/c - t) - \omega(\hat{\mathbf{q}}\cdot\mathbf{r}n_2/c)} \tag{2.38}$$

which shows an exponential damping of the wave's magnitude as a function of its penetration into the medium with a characteristic lenghscale δ_0 called skin depth defined by the imaginary part of the refractive index as

$$\delta_0 \equiv \frac{1}{\mathrm{Im}(\tilde{q})} = \frac{c}{\omega n_2}. \tag{2.39}$$

2.1.2 Interfaces

We consider here the simple case where an electromagnetic wave traveling in a medium 1 (with properties $\tilde{n}'$) in the $\mathbf{z} \parallel \hat{\mathbf{q}}$ direction reaches the interface with a medium 2 (with properties $\tilde{n}$) lying in the $\mathbf{xy}$ plane, i.e. normal incidence (we assume $\mu = 1$). Let us consider the electric $\mathbf{E} \parallel \mathbf{x}$ and magnetic field $\mathbf{H} \parallel \mathbf{y}$ of said wave as depicted in Fig. 2.2: a part of the incident wave (composed of $\mathbf{E}_i = \mathbf{E}_{0i} e^{i(\mathbf{q}\cdot\mathbf{r} - \omega t)}$ and $\mathbf{H}_i$) is transmitted ($\mathbf{E}_t$ and $\mathbf{H}_t$) into the material whereas another part ($\mathbf{E}_r$ and $\mathbf{H}_r$) gets reflected. The boundary conditions of the system impose continuity of the

amplitudes of tangential components of both fields

$$E_{0i} + E_{0r} = E_{0t} \tag{2.40}$$
$$H_{0i} - H_{0r} = H_{0t}. \tag{2.41}$$

Using Ansatz (2.7) in (2.34) and the Maxwell's equations, one obtains from the above conditions and some algebra the expression of the complex reflectivity coefficient $\tilde{r}$ and the complex transmission coefficient $\tilde{t}_{n'n}$ as a function of the materials refractive indices, i.e. the Fresnel equations:

$$\tilde{r} \equiv \frac{E_{0r}}{E_{0i}} = \frac{\tilde{n}' - \tilde{n}}{\tilde{n}' + \tilde{n}} = |\tilde{r}|\, e^{i\phi_r} \tag{2.42}$$
$$\tilde{t}_{n'n} \equiv \frac{E_{0t}}{E_{0i}} = \frac{2\tilde{n}'}{\tilde{n}' + \tilde{n}} = \left|\tilde{t}\right| e^{i\phi_t} \tag{2.43}$$

2.2 Measurements

In the usual reflectivity $R(\omega)$ or transmission $T(\omega)$ measurements, standard infrared detectors are only sensitive to the intensity I or the electromagnetic wave. Hence, one only gets access to the the complex conjugate of the complex quantities (2.42-2.43) thus resulting in the loss of the phase:

$$R(\omega) = |\tilde{r}|^2 \tag{2.44}$$
$$T(\omega) = \left|\tilde{t}_{n'n}\right|^2 \left|e^{i\omega\tilde{n}d/c}\right|^2 \left|\tilde{t}_{nn'}\right|^2 \tag{2.45}$$

where in (2.45) two interfaces are actually involved and the middle term stands for the propagation of light in a slab of thickness d of the material. In practice for reflectivity measurement, one shines light onto the surface of a sample and measures the intensity I_{sample} of the reflected light (Fig. 2.3(a)). A layer of gold (which has a reflectivity of almost 1 in the infrared range) is then evaporated *in situ* on the surface of the sample. One then measures the intensity I_{gold} of the light reflected by the gold layer (Fig. 2.3(b)). This additional measurement allows to suppress, in principle, all geometrical and equipment-induced spectral contributions thus only capturing spectral information related to the material at study. The reflectivity at vacuum-sample interface $R(\omega)$ is defined as

$$R(\omega) = \frac{I_{\text{sample}}}{I_{\text{gold}}} \tag{2.46}$$

The transmission is measured in a geometry where light is shined into one side of a sample and one measures the intensity I_{sample} of the light beam emerging on the other side. The renormalisation is performed with the same measurement without the sample and one gets I_{ref}, allowing to calculate the transmission

$$T(\omega) = \frac{I_{\text{sample}}}{I_{\text{ref}}} \tag{2.47}$$

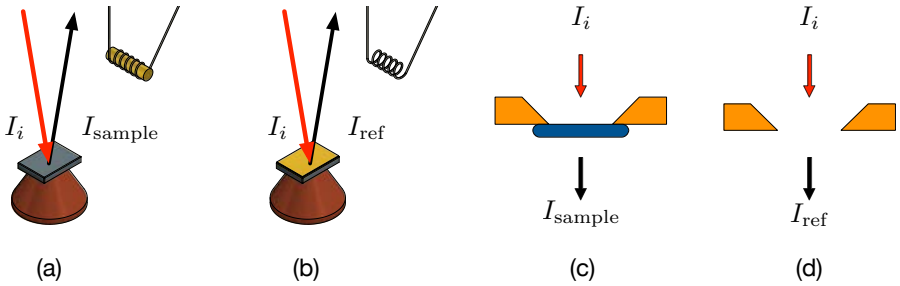

Figure 2.3 – Principle of optical spectra determination. Reflectivity geometry measurement: (a): the sample's spectrum (b) the reference spectrum after a gold layer deposition. Transmission geometry measurement: (c) sample spectrum and (d) the *hole* spectrum obtain without the sample.

In fact, in the special case where the sample is a thin layer resting on a (thicker) substrate, one performs twice the same experiment: the first time is to determine the sample+substrate response and the second time is to determine the substrate response in order to isolate the sole contribution of the sample layer. However, this geometry might induce intrinsic spectral features such as cavity interferences (Fabry-Perot) which complicates the interpretation of the spectrum. These interferences might also occur in reflectivity in the so called transparent regime above the plasma frequency in the case of a thin sample with two parallel opposed surfaces.

Additional experimental difficulties also arise due to the limited spectral range covered by each component embedded in an infrared Fourier Transform spectrometer. This imposes a different choice of hardware depending on the energy region as listed in Tab. 2.1. These differences imply that in order to cover a broad range spectrum one will have to perform the *same* experiment in every energy region (with overlaps) twice (sample and reference spectra). Fig. 2.4 shows the optical layout of a Bruker 66/v spectrometer with the Michelson's interferometer in its heart . It features two internal light sources and two detectors than can be remotely selected. Extension ports allow to add an external light source and one external detector which in our case are a synchrotron light source (as shown in Fig. 3.14(b) and discussed in section 3.5 of the the next chapter) and a bolometer detector.

The infrared range can be extended to the visible range by the ellipsometry technique, for instance with a Wollam Vase monochromator-based spectrometer, operating between 4000 and 45000 cm^{-1}. This technique has the advantage of giving access to both the amplitude and the phase of the reflectivity without having to perform a reference spectrum. The low energy part of the IR spectrum is extended by time-domain spectroscopy in the Terahertz, for example on the Teraview system which allows to probe the 10-100 cm^{-1} region and give access to both amplitude

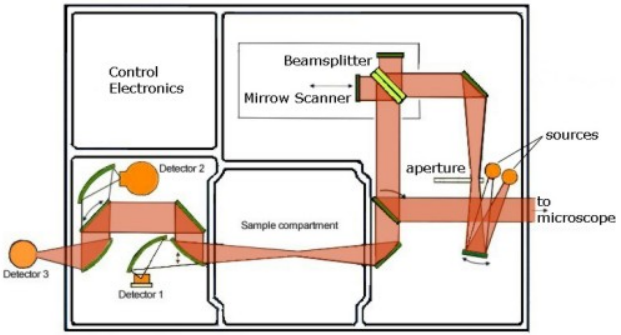

Figure 2.4 – Optical layout of a Bruker 66/v Infrared spectrometer with its remotely selectable light source and detectors, from [10].

Table 2.1 – Hardware selection for infrared spectroscopy for different spectral range (not exhaustive)

	X-FIR	FIR	MIR	NIR/VIS
ω (cm^{-1})	10-100	50-650	650-8000	10000-25000
Detector	X-FIR Bolo	Bolo	MCT/Bolo MIR/DTGS	Si/Ge Diode
Source	Hg lamp	Globar	Globar	W lamp
Beamsplitter	Si	6 μm Mylar	KBr	CaF_2

and phase (with sample and reference spectra). However in both cases, in order to perform the standard Kramers-Kronig analysis of reflectivity over a broad energy range (as described below in 2.3.1.1), only the amplitude of the reflectivity is kept and merged with the IR portion of the spectrum.

2.3 Data analysis at ambient pressure

Since one aims to determine the optical conductivity but one essentially only measures the amplitude of the reflectivity (and/or transmission), one needs to perform an additional analysis which might be undertaken through different ways as described below.

2.3.1 Reflectivity

The objective here is to restore the phase of the reflectivity by *inverting* the Fresnel equations in (2.42) and (2.44) where $\tilde{n} = \sqrt{\tilde{\epsilon}}$ thus yielding $\tilde{\sigma}$. This is a problem that can be tackled from different angles.

2.3.1.1 Kramers-Kronig Transformation

The Kramers-Kronig relations is a mathematical trick based on Cauchy's theorem and the principle of causality and eventually constrains the real part of a complex response function at a given frequency ω from its imaginary part at all frequencies as, for instance in the case of the optical conductivity:

$$\sigma_1(\omega) = \frac{2}{\pi}\mathcal{P}\int_0^\infty \frac{\sigma_2(\omega')}{\omega'^2 - \omega^2}d\omega' \tag{2.48}$$

$$\sigma_2(\omega) = -\frac{2\omega}{\pi}\mathcal{P}\int_0^\infty \frac{\sigma_1(\omega')}{\omega'^2 - \omega^2}d\omega' \tag{2.49}$$

where $\mathcal{P}$ is the principle value. If one writes the logarithm of $\tilde{r}$ from equations (2.44) and (2.42):

$$\ln \tilde{r} = \ln \sqrt{R(\omega)} + i\phi_r \tag{2.50}$$

and applies to ϕ_r the second Kramers-Kronig relation (2.49):

$$\phi_r = -\frac{2\omega}{\pi}\mathcal{P}\int_0^\infty \frac{\ln \sqrt{R(x)}}{x^2 - \omega^2}dx + \phi_r(0) \tag{2.51}$$

one sees than the phase can be numerically restored thus retrieving $\tilde{\epsilon}(\omega)$ and eventually $\tilde{\sigma}(\omega)$. However, since the integral (2.51) runs over all frequencies and one has only data within a limited spectral range, one is forced to perform some assumptions on the behavior at the limits of $R(\omega)$ and do extrapolations with a power-law: above the

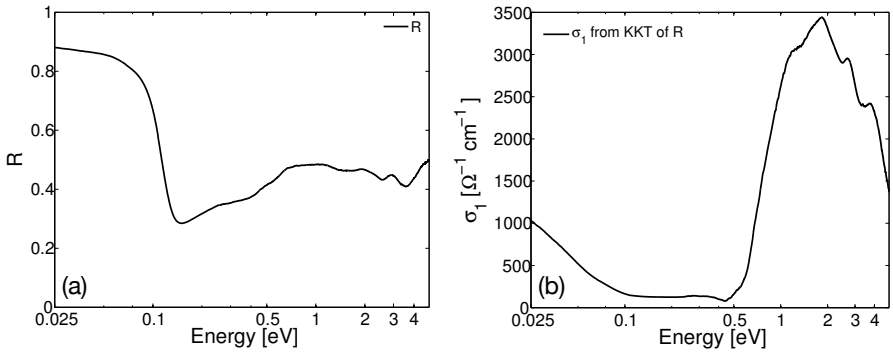

Figure 2.5 – (a) Reflectivity of BiTeI at sample-vacuum interface and (b) real part of the optical conductivity obtained by Kramers-Kronig transformation.

highest frequency data point, a free-carrier behavior is assumed with a reflectivity decreasing as ω^{-2} or ω^{-4} whereas at low frequency a choice has to be done over several type of extrapolations depending on the type of material under study. For instance, in the case of an insulator, one assumes a constant reflectivity and in the case of a metal, one assumes a Hagen-Rubens behavior where the reflectivity decreases from unity proportionally to $\omega^{-1/2}$.

For example, Fig. 2.5(a) shows the reflectivity of BiTeI measured from FIR to VIS range and Fig. 2.5(b) shows the real part of the optical conductivity obtained with such a Kramers-Kronig transformation.

2.3.1.2 Drude-Lorentz model

Another way of using the reflectivity data $R(\omega)$ to determine the complex dielectric function $\tilde{\epsilon}(\omega)$ of the material is to model it by a Drude-Lorentz (DL) sum:

$$\tilde{\epsilon}(\omega)_{\mathrm{DL}} = \epsilon_\infty + \sum_i \frac{\omega_{p,i}^2}{\omega_{0,i}^2 - \omega^2 - i\gamma_i\omega} \tag{2.52}$$

where in each term of the sum– also called Lorentzian – the parameters ω_p, ω_0 and γ are the plasma frequency, the oscillator frequency and the damping respectively. These are fitted so that the Fresnel equation used to calculate the corresponding theoretical reflectivity $R_{\mathrm{DL}}(\omega)$ agrees with $R(\omega)$:

$$R(\omega) \simeq R_{\mathrm{DL}}(\omega) \equiv \left| \frac{1 - \sqrt{\tilde{\epsilon}(\omega)_{\mathrm{DL}}}}{1 + \sqrt{\tilde{\epsilon}(\omega)_{\mathrm{DL}}}} \right|^2 \tag{2.53}$$

We note the special case for the Lorentzian oscillator $\omega_0 = 0$, which corresponds to a Drude oscillator. One notes that by construction this model complies with the

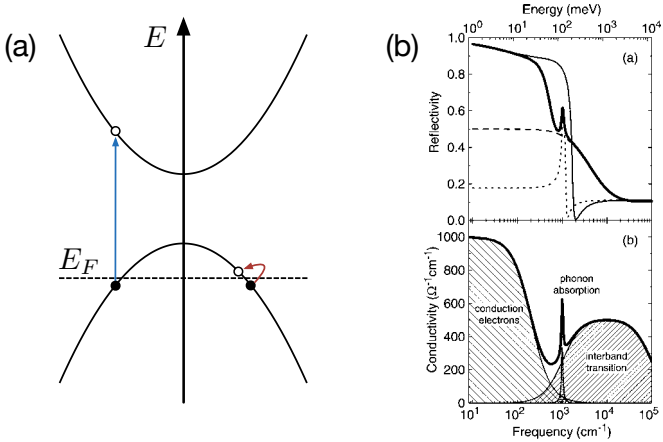

Figure 2.6 – (a) Direct intra (red) and inter (blue) band transitions (b) Example of calculated reflectivity and conductivity based on a dielectric function containing one Drude term and two Lorentzian oscillators, taken from [11].

Kramers-Kronig relations.

Lorentzians terms (insulator) are usually attributed to the interband transitions occurring at higher energy (or well defined phonons) while the Drude terms fall into the intraband transition regime characteristic of metal. For instance, Fig. 2.6(a) shows a simple two band configuration of a semi-conductor in the metallic regime. One considers direct transitions: the low energy excitation (red arrow) around the Fermi energy and the higher energy inter band transition (in blue). An example of reflectivity and conductivity spectrum calculated from a dielectric function modeled by a three term Drude-Lorentz sum is shown in Fig. 2.6(b). The contribution of conduction electrons is modeled by a Drude peak whereas a narrow Lorentzian stands for the phonon peak and a Lorentzian oscillator describes the interband transition[1] [11].

This approach may however turn to be unhelpful in certain cases, in particular in the absence of sharp spectroscopic features. The interband transitions are very sensitive to the band structure of the material and might be difficult to capture with a Lorentzian. For this reason, a Kramers-Kronig transformation might be better suited to calculate the optical conductivity. For example, the reflectivity of Rashba spin-split semiconductor BiTeI shown in Fig. 2.7(a) is rather well reproduced with five oscillators. However, the corresponding optical conductivity shown in Fig. 2.7(b) hardly compares with the conductivity obtained with a Kramers-Kronig transformation (of the same reflectivity) and in particular completely misses the gap above 0.4 eV.

[1] Usually a combination of narrow oscillators is used for the transitions.

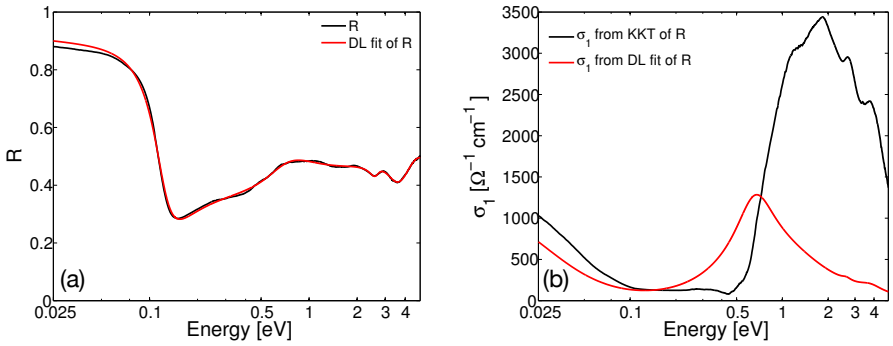

Figure 2.7 – (a) Reflectivity of BiTeI and (b) real part of the optical conductivity obtained by a Drude-Lorentz model.

2.3.1.3 Variational Dielectric Function Fitting

As mentioned above, the reflectivity can not always be well-reproduced by the calculated reflectivity from a Drude-Lorentz modeling of $\tilde{\epsilon}(\omega)$. This is because all physical mechanisms[2] can not be accounted for in such a model exclusively constituted of a relatively small number of a superposed smooth bell-like shaped curves. However, the first approximation of $\tilde{\epsilon}(\omega)$ can be further refined up to a point where all spectral features are reproduced. This is achieved using a Kramers-Kronig consistent variational dielectric function [12], as implemented in RefFIT [13], where the number of Lorentzian oscillators of the sum now tends to the number of points in the reflectivity curve, thus incidentally suppressing the individual physical meaning of each oscillator. In practice, one first builds a DL model whose parameters are fitted to globally mimic the overall shape of the reflectivity data. That first fit is used as a starting point for the VDF procedure; this is crucial for the convergence of the solution. This method produces the same result as a numerical Kramers-Kronig transform of $R(\omega)$, provided that the fit is perfect.

2.3.2 Transmission

The expression of $T(\omega)$, the measured transmission through a sample of thickness d placed in vacuum, is given by:

$$T(\omega) = |t_{vs}(\omega)|^2 \left| e^{i\omega\sqrt{\epsilon(\omega)}d/c} \right|^2 |t_{sv}(\omega)|^2 \tag{2.54}$$

Where $t_{vs}(\omega)$ and $t_{sv}(\omega)$ are the complex transmission coefficients at the vacuum-sample and sample-vacuum interfaces given by (2.43). We disregard the internal

[2] I.e. in addition to the intrinsic geometrical artifacts such as Fabry-Perot oscillations and noise.

Fabry-Perot reflections, assuming that the magnitude of the middle modulus is small. Using $\sqrt{\epsilon} = n_1 + in_2$ in the exponential and developing the modulus gives:

$$T(\omega) = \left| \frac{4\tilde{n}}{(1+\tilde{n})^4} \right| e^{-\omega n_2 2d/c} \left| e^{i\omega n_1 d/c} \right|^2 = \left| \frac{4\tilde{n}}{(1+\tilde{n})^4} \right| e^{-\omega n_2 2d/c} \tag{2.55}$$

since the last modulus contains only oscillatory terms and amounts to 1. Taking the logarithm and re-arranging for n_2 yields

$$n_2 = -\frac{c}{2d\omega} \ln T(\omega) + \frac{c}{2d\omega} \ln \left| \frac{4\tilde{n}}{(1+\tilde{n})^4} \right| \simeq -\frac{c}{2d\omega} \ln T(\omega) \tag{2.56}$$

since the content of the logarithm tends to 1. Using (2.37) the expression for n_2 is

$$n_2 = \frac{4\pi\mu_1\sigma_1}{\omega n_1} \tag{2.57}$$

which means that a comparison of (2.56) and (2.57) for highly conductive metals (for n_1 and μ_1 constant), the frequency behavior of the real part of the optical conductivity is given by the logarithm of the transmission

$$\sigma_1(\omega) \propto -\ln T(\omega) \tag{2.58}$$

This approximation allows to grasp solely from transmission data, for instance here for a 6 micron-thin flake shown in Fig. 2.8(a), the behavior of sharp spectroscopic features in the optical conductivity, as in this case the location of energy gap. However it does not allow to perform a quantitative analysis of the conductivity. This is well exemplified in Fig. 2.8(b) where one sees that the energy gap is rather well reproduced but also that the trend is wrong at the border of the data range, where the real refraction index n_1 can no longer be approximated with a constant. This corresponds to the spectral region where the reflectivity is predominant.

2.3.3 Direct Inversion

When both transmission and reflectivity data are available in the same spectral range and the geometrical details of the sample are well determined (such as the thickness d of the sample), a direct inversion process can be undertaken with certain assumptions. One starts by using the transmission to extract the complex refractive index n_2 as done in (2.56) and one calculate the expression of $R(\omega) = |\tilde{r}|^2$ using (2.42) with $\tilde{n}_1 = n_1 + in_2$ and $\tilde{n}'_1 = n'_1 + in'_2$:

$$R(\omega) = \frac{(n'^2_2 - 2n_2n'_2 + n_2{}^2) + (n_1 - n'_1)^2}{(n'^2_1 + 2n_2n'_2 + n_2{}^2) + (n_1 + n'_1)^2} \tag{2.59}$$

In the simpler case where the first medium is the vacuum, $n'_1 = 1, n'_2 = 0$ and one is left with

$$R(\omega) = \frac{n_2{}^2 + (n_1 - 1)^2}{n_2{}^2 + (n_1 + 1)^2} \tag{2.60}$$

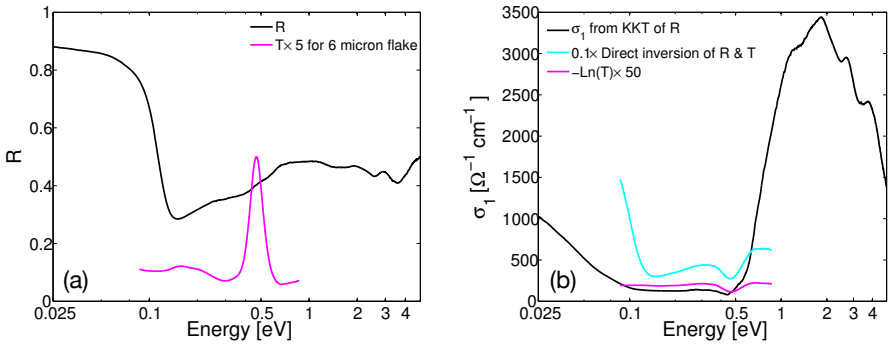

Figure 2.8 – (a) Reflectivity of BiTeI at sample-vacuum interface and transmission (black) of a 6 micron-tick flake, magnified five times (magenta). (b) Optical conductivity obtained by Kramers-Kronig transformation on R (black), by direct inversion of R and T scaled by a factor or 10 (cyan) and $-\ln(T)$ magnified 50 times (magenta).

and one solve for n_1 :

$$n_1 = \frac{-R - 1 \pm \sqrt{-n_2^2 R^2 + 2n_2^2 R - n_2^2 + 4R}}{R - 1} \tag{2.61}$$

Knowing d, one can insert (2.56) into (2.61) and thus obtain the frequency dependence of the complex refractive index $\tilde{n}(\omega) = n_1(\omega) + in_2(\omega)$. Such procedure was used on transmission and reflectivity data of BiTeI in the shared spectral region as shown in Fig. 2.8(a). The results shown in Fig. 2.8(b) is a conductivity which qualitatively agrees well with σ_1 obtained by Kramers-Kronig transform, in particular the uprise towards low energy, presence of the energy gap and a slight increase of σ_1 between α and β transitions (as discussed in more detail in chapter 4 devoted to the study of BiTeI). What is *not* well captured is the steep rise of σ_1 above the gap which is replaced by a flat response very reminiscent of the behavior of $-\ln T(\omega)$.

2.4 Data analysis at high pressure

The major physical difference from this type of measurement is the immediate surrounding of the sample which has now one of it's surface directly placed behind a diamond anvil as shown in Fig. 3.11 and is otherwise surrounded by the pressure transmitting media. In some cases, a very thin layer of the pressure transmitting media manages to go between the sample surface and the diamond, thus leading to fast Fabry-Perrot oscillations. The main effect of this geometry is that the property that we measure does not only depend on the sample properties but also on the properties

of the diamond anvil(s) of the DAC which need to be disentangled in order to draw physical conclusion relative to the sample only.

Hopefully, diamonds of type IIac are optically mostly transparent in the infrared [14, 15] except in a narrow region near 2000 cm^{-1} (where two strong absorption peaks are lying) which forces us to discard this region. The refractive index of diamond is essentially constant with $n_{1,d} \approx 2.4$ in the infrared and in the following work we'll use $\tilde{\epsilon}_d = n_{1,d}^2$ so that we can calculate the reflectivity $R(\omega)_{sd}$ at the sample-diamond interface using the Fresnel equation (2.42) now involving the dielectric function of both media:

$$R(\omega)_{sd} = \left| \frac{\tilde{\epsilon}(\omega)_d - \tilde{\epsilon}(\omega)}{\tilde{\epsilon}(\omega)_d + \tilde{\epsilon}(\omega)} \right|^2 \tag{2.62}$$

which we will use in the same fashion as in the previous section in order to obtain the optical conductivity of the material under pressure. However, the limited spectral range accessible to us and the difficulty to measure absolute reflectivity and/or transmission significantly complicate this task and, as we'll see in the following chapters, might therefore affect the quantitative accuracy of the results.

2.4.1 Drude-Lorentz Model

Just as described in 2.3.1.2, the dielectric function is modeled with a Drude-Lorentz sum and is used to calculate the reflectivity at the sample-diamond interface $R(\omega)_{sd}$ in (2.62) and the parameters of this sum are adjusted so that the experimental reflectivity $R(\omega)_{\text{DAC}}$ is well reproduced. One might attempt to deal with the problem of the accuracy of the magnitude of the high pressure data by allowing it to deviate from the best fit obtained in (2.62) by introducing a frequency independent constant C such as

$$R(\omega)_{\text{DAC}} \approx C \times R(\omega)_{sd} \tag{2.63}$$

Lets consider a set of ascending-sorted pressures $\{p_1, p_2, \ldots, p_N\}$ and the corresponding dataset of reflectivity curves $\{R(\omega)_{p_1}, \ldots, R(\omega)_{p_N}\}$. If one compares $R(\omega)_{p_1}$ to $R(\omega)$ the ambient-pressure reflectivity curve and finds that the spectroscopic features of both curves are very close (beside magnitude), one might think that the dielectric function at ambient pressure, $\tilde{\epsilon}$, and the one at p_1, $\tilde{\epsilon}_{p_1}$, might only slightly differ due to the application of pressure. Therefore, injecting (2.62) in (2.63) one could attempt to benefit from the wider spectral range of $R(\omega)$ in (2.53) to complement the high pressure data by simultaneously fitting the two reflectivity spectra with a common dielectric function $\tilde{\tilde{\epsilon}}$ and the constant C. The parameters of the oscillators falling outside the spectral range of the high pressure data are then fixed and a dielectric function $\tilde{\epsilon}_{p_1}$ is determined by adjusting the remaining free parameters so that a good agreement is reached in (2.63). The resulting parameters are used as starting parameters for the next reflectivity $R(\omega)_{p_2}$ and so on, unless a change is induced by the

pressure which requires to modify the model by adding or removing one (or several) oscillators.

Again, this method of analysis does not always work, especially in the case where the ambient pressure data at vacuum-sample interface were not well reproduced due to inter band transitions being not well captured with a Drude-Lorentz model.

2.4.2 Direct inversion

In subsection 2.3.3, we previously came to the observation that the direct inversion only leads to qualitative results already at ambient pressure for the case of BiTeI (we did not perform transmission experiments on the purple bronzes[3]). In the case of high pressure, the measured data are not absolute (contrary to ambient pressure) and one needs to estimate the thickness of the sample for all pressures. We approximated the latter by using a theoretical Bulk modulus and assuming an isotropic compression:

$$d(P) = d_0 \left(\frac{P - 0.001}{K} \right)^{-1/3} \tag{2.64}$$

where $K = 219$ kbar is the bulk modulus of the material, d_0 the thickness of the sample at ambient pressure and P the pressure applied onto the sample. In addition, when using a pressure cell, the primary medium is not the vacuum but the diamond which changes $\tilde{n}_1'$ in (2.59). For these reasons, the results obtained with this method were not used to carry out a quantitative analysis of our data although they provide qualitatively valid information as shown in Fig. 2.10(a) and 2.10(c)

2.4.3 Variational Dielectric Function Fitting

This procedure is very close to the one described and used by Okamura *et al.* [16, 17] and mainly differs by the fact that we do not benefit from a reference spectrum as reliable as the reflectivity of a gold-diamond interface. Therefore, we introduced a frequency-independent proportional constant C.

In practice, just as in subsection 2.4.1, one starts the analysis of $R(\omega)_{p_1}$ to model the dielectric function so that the reflectivity (2.63) at the sample-diamond interface is estimated by a Drude-Lorentz model which was (at first) simultaneously fitted to ambient-pressure reflectivity.

Here, as schematized in Fig. 2.9, one performs an additional Kramers-Kronig-consistent variational dielectric function analysis as described in 2.3.1.3 on $R(\omega)_{p_1}$ and $R(\omega)$ simultaneously allowing to extract the value of C and a common dielectric function $\tilde{\tilde{\epsilon}}$. Then, using the numerical solution $\tilde{\tilde{\epsilon}}$, one performs *once again* the analysis with C fixed on $R(\omega)_{p_1}$ thus yielding the dielectric function corresponding to the

[3] This is due to a technical problem encountered on the Bruker 66/v of the beamline which prevented its use during our beam time.

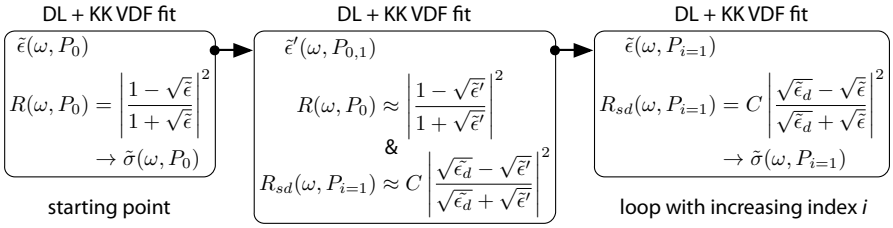

Figure 2.9 – VDF fitting workflow. $\tilde{\epsilon}_d$ is the dielectric function of diamond.

lowest pressure $\tilde{\epsilon}_{p_1}$. This numerical solution is then used as a starting point for the analysis of $R(\omega)_{p_2}$, and so on.

For example, lets consider the case of BiTeI (whose reflectivity both at ambient and high pressure are shown in Fig. 2.10(a)) and define $X(\omega)$ as the ratio of the experimental data $R_{p_1}(\omega)$ over the reflectivity at sample-diamond interface $R_{sd}(\omega)$ at ambient pressure, calculated from the variational dielectric function:

$$X(\omega) = \frac{R_{p_1}(\omega)}{R_{sd}(\omega)} \tag{2.65}$$

For a pressure of 0.2 GPa , $X(\omega)$ has a mean value x close to 2 and we show the frequency dependance of $X(\omega)/x$ in Fig. 2.10(b). One mostly notices the strong oscillations (due to the resonances in the sample cavity, that are not taken into account in the calculation of R_{sd}) on top of a rather monotonic increase. Such a value of 2 is very close to the frequency-independent value of C determined in the method described above which gives a value of 2.015 while allowing an excellent reproduction of experimental data as indicated in Fig. 2.10(b) by the ratio $Q(\omega)$ defined as

$$Q(\omega) = \frac{R_{p_1}(\omega)}{C \times R_{sd}(\omega)} \tag{2.66}$$

which barely deviates from 1. The dielectric function $\tilde{\epsilon}_{p_1}$ allows to determine the optical conductivity as shown in Fig. 2.10(c) which is comparable to the ambient pressure conductivity and greatly facilitates its interpretation. One notes the presence of oscillations in the conductivity which is in fact an artifact due to the Fabry-Perot oscillations in the reflectivity. We propose instead a *smoothed* conductivity curve within that spectral region, shown in navy-blue.

However, since the convergence of this iterative numerical process is very sensitive to the initial variational dielectric function, such technique might not be applicable in the case where abrupt changes occurs between successive high pressure reflectivity curves. The origin of these differences could be due to the occurrence of a phase transition that material undergoes or, more simply, to a too coarse pressure mesh imposed by experimental constrains.

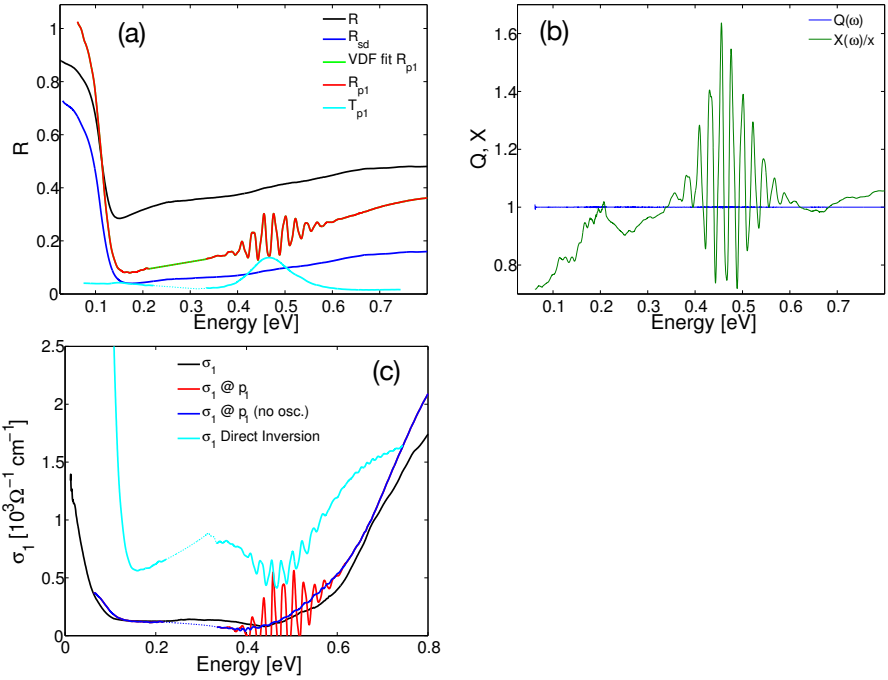

Figure 2.10 – BiTeI under pressure. (a) Reflectivity and transmission data: R (black) is the experimental reflectivity at the sample-vacuum interface. R_{sd} (navy blue) is the calculated reflectivity at the sample-diamond interface. R_{p_1} (red) is the experimental reflectivity under pressure p_1 at sample-diamond interface and it's variational dielectric function fit (green). T_{p_1} is the transmission at pressure p_1. (b) The ratios of curves described in panel (a): $Q(\omega) = R_{p_1}/(C \times R_{sd})$ (navy blue) and $X(\omega) = R_{p_1}/R_{sd}$ (green). (c) Real part of optical conductivity: σ_1 (black) is the ambient pressure optical conductivity from Kramers-Kronig transformation of R, $\sigma_1@p_1$ (red) is the optical conductivity extracted from the variational dielectric function fit of R_{p_1} and the navy blue curve is a smooth of Fabry-Perot oscillations. The cyan curve is the conductivity obtained at pressure p_1 by direct inversion.

CHAPTER 3

High pressure setup for optical spectroscopy at low temperature

Soyez plutôt maçon, si c'est votre talent.
Extrait du Chant IV de "L'Art poétique" de Nicolas Boileau, 1674

In this chapter, we will describe the techniques that were used to perform Infrared and Raman spectroscopy under high pressure and low temperature as well as the experimental apparatus that were specifically designed, built and also assembled from commercial parts, for that purpose during the present PhD thesis work.

Since the pressure P is defined as $P = F/A$, where F is the applied force F on a given surface A, if one looks at reaching high value of P in the GPa range, one has either to apply a huge force on a surface or apply a force on a very small surface. In fact a combination of both is used in practice and as one could expect requires the use of very hard materials that are able to withstand such elevated pressures.

3.1 Diamond anvil cell

3.1.1 Quick historical introduction

The chronology of the technological development of high pressure apparatus is fascinating by itself and the technique passed several milestones in the past few years which occasioned several *historical* papers such as the one from Bassett [18].

To summarize, historically, high pressures of the GPa range were first reached by Bridgman at the beginning of the 20^{th} century with devices pressing two flat pieces (or

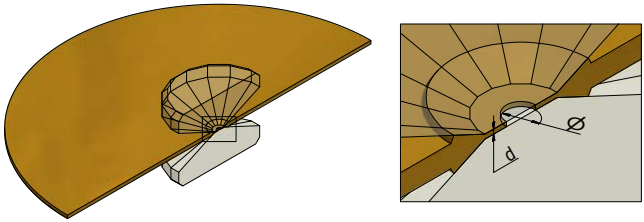

Figure 3.1 – 3D Cut view of two diamond anvils sealing the metallic chamber (proportions are here respected and details are best seen in Fig. 3.5).

anvils) of tungsten carbide one against the other. This concept was later enhanced with the use of the hardest known material to man which is of course diamond thus yielding the Diamond Anvil Cell (DAC). The free of charge access to seized diamond of illegal origin granted by the U.S. government to its research institutions is acknowledged to have undoubtably boosted the activity of the field. The last missing significant ingredient for the reliable use of the technique was a reliable way to determine the magnitude of the pressure applied. One answer was the ruby fluorescence shift acting as a pressure gauge which came two decades later.

3.1.2 Operation principle

The concept of a DAC can be summarized to very few items: two anvils made of diamond are facing each other and are pressed together thus applying strain on whatever is in the middle. The way the pressure is applied onto the sample at study is a concern: one is looking to pressurize the sample in an uniform way or hydrostatically. Just as a diver feels the pressure of the water above (almost) equally around him, one aims to reach a distribution of pressure around the sample as homogeneous as possible, with the difference that the pressure applied on the diver and the one applied on the sample are not of the same order of magnitude at all. Such quasi-hydrostatic conditions can of course not be satisfied if one just puts the sample between the two anvils as the uniaxial stress will by definition not create the desired pressure distribution. Instead, to imitate the diver's environment, one puts the sample in a pressure transmitting medium that will be contained in a sealed chamber by the two anvils as shown in Fig. 3.1. The motion of the diamonds will cause deformation of the chamber and if producing shrinkage (Figs. 3.5(h)-(f)), will result in a pressure increase. The piece constituting the walls of this sealed chamber is the gasket.

The detail of the device however is more complex as detailed by Dunstan and Spain [19, 20]. Starting with the diamond, the first property that immediately comes to mind is its significant cost. In fact in the present case, the use of these gems is two-fold: it has to withstand the force applied and also provide a suitable optical

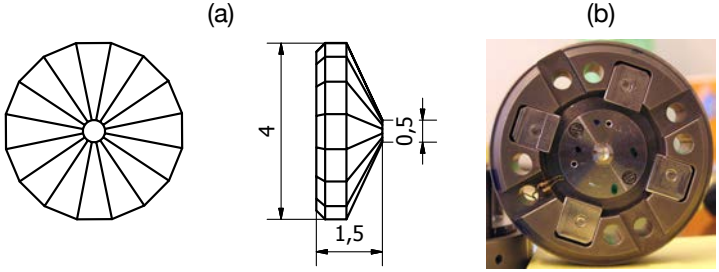

Figure 3.2 – (a) Drawings of type IIac diamonds used in the DAC (dimensions are in mm). (b) Diamond mounted on its seat in the lower part of the DAC (from [21]).

window. The first aspect is in fact inherited from its jewel origin and is related to the varied selection of diamonds cuts: the goal here is to determine the cut that will best provide resistance to the aimed pressure runs and ease *every-day* operations. For this same reason, diamonds with mechanical defects should be discarded. The second aspect is a transparency issue: type I diamonds contain nitrogen impurities that give a yellow tint to the stone and absorb more light in the Infrared region than type IIa diamonds which are of course preferred.

The diamonds used in this work were synthetic type IIac Standard design cut diamonds with 16 facettes and thickness of 1.5 mm from Almax Industries [14] as drawn in Fig. 3.2. As the expected pressure range was below 20 GPa and since no transport experiments were anticipated the 550 μm culet has sharp edges or no bevel that would have reduce the strain and the risk of breakage (in particular of the electrical wiring).

There are many types of devices using diamond as anvil. In all cases, when a pair is involved, huge importance is given for obtaining proper alignment of the two culets and for this purpose modern devices offer translational and rotational corrections diversely attributed to the anvils to insure both parallelism and uniaxial displacement of the two anvils. One can easily check the alignment by looking for fringes when at the same time shining white light through the DAC and by carefully positioning very closely the two culets; alignment is sufficiently good when only one fringe is spread across the whole culet. The way the anvils are "set in motion" mainly differentiates the type of DAC. For instance, there is the piston-cylinder type where one anvil is fixed on the piston and the other on the cylinder. There are screw-actuated cells where the pressure is applied/maintained by the tightening of an array of screws symmetrically placed around the anvils. There are also pneumatic systems were the displacement of the anvil is induced by a variable force applied by the deformation of a membrane by a pressurized element [22]. This last type of cell has the advantage of being rather easily remotely controlled via the intermediate of some tubing which in

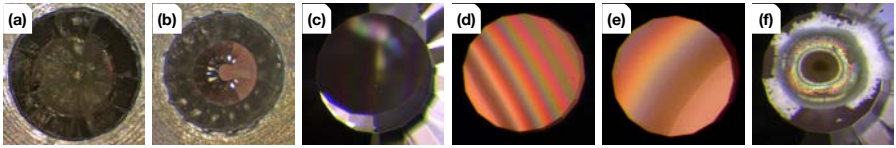

Figure 3.3 – Alignment of diamonds in the DAC. (a) Broken diamond after a problematic pressure run. (b) New diamond set on a new seat. (c) Obvious mismatch of the two culets. (d) Numerous Newton fringes between culets: poor parallelicity. (e) One unique fringe between culets: reasonable parallelicity and good match of the 16 edges. (f) successful check of parallelicity [20, 23] with crushed AgI powder displaying concentric texture.

turn enables *in situ* pressure tuning. Such desirable feature is however sometimes also found in other type of DAC but at the expense of a somewhat larger size footprint.

The DAC used during this Ph.D work is the Membrane Diamond Anvil Cell MDAC-XHP, a commercial model from BETSA [24] which is schematically shown in Fig. 3.4. With dimensions of 50 mm of diameter and 32mm of height and working distance from the top of 13 mm, it's main feature is an helium-gas driven stainless-steel membrane (3) that allows to apply forces op to 10 kN to the upper anvil. Helium is funneled via a low-profile home-made right angle connexion (1) inside the membrane where pressure can reach 200 bar. An interface disk (4)[1] insures that the membrane is tightly in contact between the piston (5) and with the covert (2) when the latter is tightened to the cylinder (14). The two rockers have an opening angle of 60° that allows to benefit from the use of high numerical aperture optics (up to 0.5) thus enabling its use in optical studies where collection of light beam of small intensities is an issue. Translation and tilt/rotation on both lower and upper anvils (11 and 9) can be corrected for matching culet orientation by joint use of the lower diamond seat (12), lower rocker (13), upper rocker (6) and upper diamond seat (8). Each diamond lies free on a flat surface of the rocker that allows tilt correction and is centered (translation) by the seat. The absence of glue facilitates the cleaning of the anvils. The uniaxial displacement of the piston against the cylinder is insured by four precision guides (7) symmetrically placed around the anvils. The gasket (10) can be fixed on one of the diamond seats. Since the cell is assembled by screwing the cylinder on the covert, no electrical feedthrough is possible on the sides of the cover. Four vertical holes in the cylinder can be used for that purpose, keeping however at least two aligned holes free to be able to plug the two guides of the tool needed to open-close the cell and care should be paid to avoid damaging the wires as no protections are embedded in the cell.

[1] Failure to properly put that element in place before a pressure run may result in a permanent damage of the membrane caused by an unreversible deformation thus requiring the replacement of the membrane.

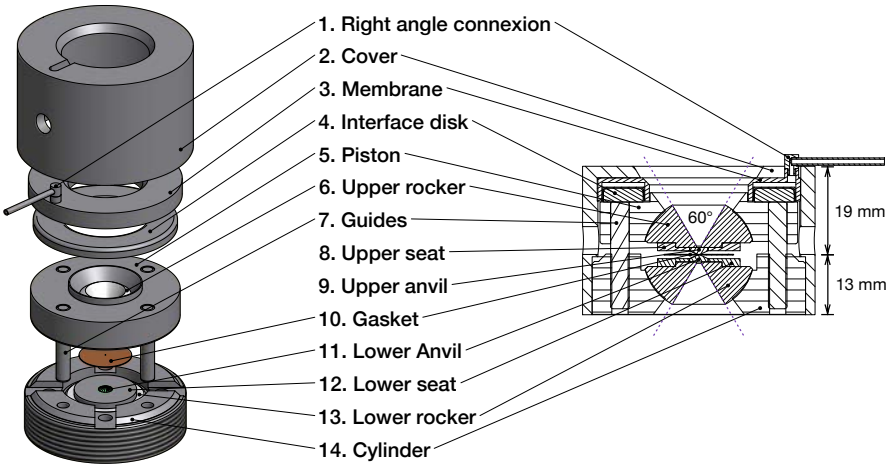

Figure 3.4 – Schematic views of BETSA Diamond Anvil Cell

3.1.3 Pressure transmitting medium

Hydrostatic (or quasi-hydrostatic) conditions cannot be reached for samples in direct contact with the diamonds. Thus, samples are embedded by appropriate substances acting as pressure transmitting media. Depending on the shape and state of the sample, the spectral region, the temperature and pressure ranges of interest, a pressure medium is selected. Liquids are the best choice for their ease of use and hydro-staticity but require more care during the preparation of the cell as the bottom of gasket needs to be tightly in contact with the lower anvil to prevent leakage. Owing to their chemical composition infrared absorption can be strong in the MIR region, therefore markedly reducing their usefulness. However, if the spectral range of interest lies in the far infrared, Daphne oil 7474 is for instance claimed to be a good candidate [25]. The same is valid in NIR above 4000 cm^{-1} above the last absorption peak. Powers can act as their own pressure medium, however in case of strong absorption such powder have to be diluted in a transparent pressure medium.

In our own MIR experiments, we used KBr as a pressure medium. This mineral is of course transparent in the MIR region and is less suspected to undertake a chemical reaction with the sample under study. Ground KBr powders were heated above $100°$C for at least 24 hours to minimize its water content. They were then grounded one more time before been put back in the oven until use.

One disadvantage of KBr (beside being driven away from hydrostatic conditions) is that loading of a sample into the hole of the gasket is tedious: KBr grains agglomerate, tend to move the sample, cannot always be distinguished easily from ruby

chips and the entire loading process needs to be swift in order to limit water up-take[2]. Moreover, the sealing of the gasket requires higher pressure applied to the membrane and the maximum pressure achieved with KBr is smaller than the one for loads using liquid pressure transmitting media. On the optical side, the presence of interfaces and gaps between grains causes a diffusive effect greatly decreasing the intensity of the signal in transmission which lasts until the grains are more tightly put together with increasing pressure. This somewhat reduces the possibility of using Transmission data as an input for a quantitative analysis under pressure. However strong qualitative spectroscopic features can be easily followed during the pressure run.

3.1.4 Gasketing

Gaskets are usually made out of small metallic discs. Several parameters are responsible for the actual sample thickness and the pressure range that a particular experiment can reach. The thickness of the disc, the material's hardness, the external pressure applied to the membrane as well as the diameter of the hole drilled in the gasket, which forms the actual sample chamber, are main parameters. Gasketing is extensively discussed in the two articles of Dunstan and Spain and in the book of Eremets [19, 20, 26].

In our case, disks of 15 mm of diameter were made out of square sheets of semi-hard 98/2 ratio alloy of CuBe of 150 μm of thickness from Goodfellow [27] with the help of a home-made extruding device which allowed to produce, in chain, large quantities of discs of good flatness and reproducible dimension for a very low cost by unit. These disks (as depicted in Fig. 3.5(a)) are imprinted with the shape of the two anvils culet by progressively cranking the pressure in the membrane (Figs. 3.5(b) and (c)) up to a value that will later constitute a limit when performing the actual experiment. Thickness obtained for different pressures are plotted in Fig. 3.6(c). After pressure relaxation (Fig. 3.5(d)), a hole is drilled by spark erosion at the center of the marks of the culets with the commercial Electric Discharge Machine from BETSA (Fig. 3.6(a)) and kerosene as an insulation liquid (represented in blue on Fig. 3.5(e)). The hole (Fig. 3.5(f) and Fig. 3.1) should have a diameter that does not exceed about a third of the size of the culet so that the displacement of the diamonds to induce the desired deformation, reducing the hole's diameter (Fig. 3.5(h)) rather than expanding it, which could lead to breakage by, for instance, dry contact of the anvils (Fig. 3.5(j)). At the end of the pressure run, the relaxed gasket (Fig. 3.5(i)) does not recover its initial shape and depending on the pressure transmitting media (represented in blue within the hole) some stress remains still applied onto the sample as observed during experiments using KBr.

As one can not drill a hole with the gasket seated on the lower anvil, one keeps a permanent marker on both the gasket extremity and on the cylinder so that one is able to precisely put the gasket back with the same orientation in order to retrieve the

[2]Loading in a nitrogen purged glove box can partly solve this problem.

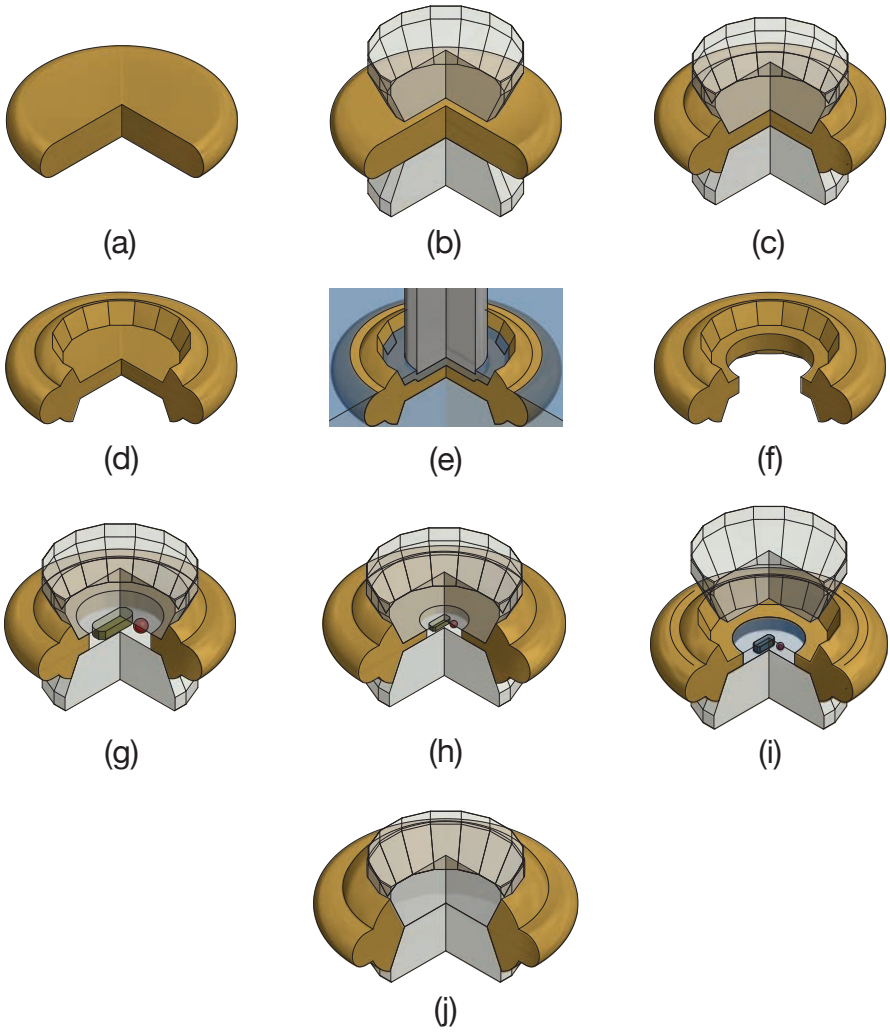

Figure 3.5 – 3D view in $3/4$-cut at different stages of the gaskets manufacturing process and use. The dimensions and proportions of the components are greatly exaggerated to ease visualization.

same match between the anvils and their impressed marks. The fitting can be further increased with a modest application of a few bar of helium pressure of the membrane with a DAC fully reassembled. Although it is possible to attach the gasket to one of the diamond seats by screws plus an additional piece, it was found more practical and faster to use three small balls of adhesive paste "patafix"[28] symmetrically surrounding the lower anvil to secure the gasket's seating.

During this work, on the latest installed membrane, a pressure of 70 bars, a tungsten tip of 200 μm of diameter produces a hole of 220 μm. A lot of remains are left on the border of the hole by the drilling process and have to be thoughtfully cleaned before use, to insure proper sealing.

3.1.5 Membrane pressure control

The pressure of helium gas inside the membrane is controlled by BETSA's Pneumatic Drive System PDS 200 which is equipped with a 0.4 litter Helium gas bottle and a digital display showing the pressure measured by a gauge placed in parallel to the capillary feeding the DAC as schematized in Fig. 3.6(b). A small volume can be brought to the pressure of the bottle before closing the latter, thus acting as a ballast system preventing the involvement of large quantities of gas that could cause damage. The membrane is controlled by two needle-valves: one allowing helium to flow from the ballast and one allowing the release of the gas. An intermediate valve is also located a few centimeters from the membrane.

The exhaust port of the PDS 200 has been modified so that it is possible to connect the capillary network via a KF25 connector to a pump to purge the system. This should prevent the formation of corks of unwanted frozen gases when working at low temperature. In order to make the system more ergonomic and diminish the fatigue on the high-pressure connections, the capillary leading to the membrane has been equipped with Swagelok QM2 miniature quick-connect connectors [31] that are able to withstand the pressure inside the capillary.

It was found that with our two meters-long network of capillaries the ballast needs to be filled quite often thus inducing steps in the pressure sweep. A careful control of the needle-valve "In" in Fig. 3.6(b) before the membrane, and bypass of the ballast by keeping the bottle open, allows to increase the pressure more regularly.

3.2 Cryogenic equipment

The DAC is clamped to the cold finger of a commercially available liquid helium flow cryostat, model ST-100 from Janis, to which is clamped the DAC. The stainless steel capillary line used to adjust the pressure into the membrane is thermally anchored with several windings along the thermal gradient of the cryostat as shown in Fig. 3.7(a). Temperature monitoring is obtained with two thermometers; one is placed at the tip of the cold finger (original diode sensor), another one close to be lower diamond (small

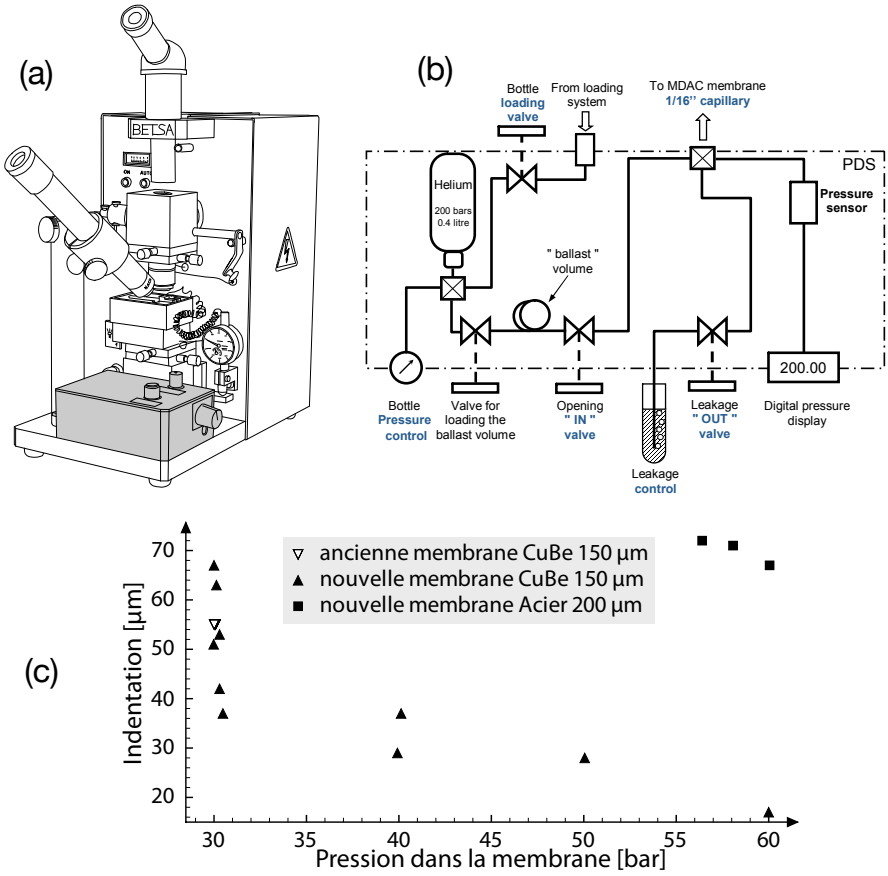

Figure 3.6 – (a) Electric discharge apparatus from BETSA [29]. (b) Schematics of the pneumatic drive system from BETSA [30]. (c) Indentation as a function of pressure in the membrane [21].

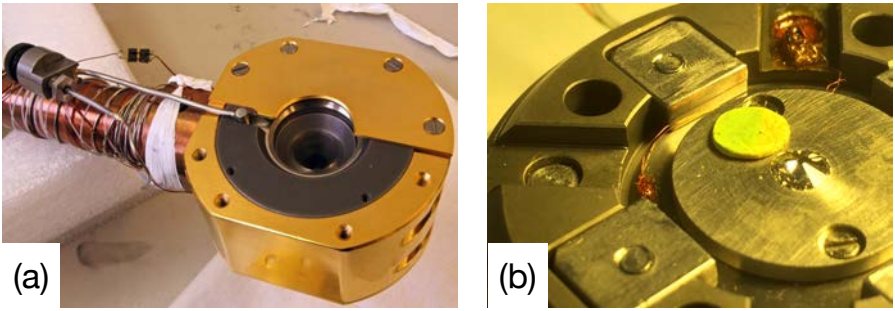

Figure 3.7 – (a) Winded capillary network with micro-valve connection, electrical wiring of internal thermal sensor and DAC clamped on the coldfinger of the cryostat without the last gold-plated radiation shielding piece, from [21]. (b) Open DAC with cernox sensor glued to the lower rocker.

factor bare chip Cernox sensor) on the lower rocker as shown in Fig. 3.7(b). The lowest achieved temperature is 18 K and 13 K in transmission and reflection geometry respectively.

One indicates that during preliminary tests, using the original vacuum shroud of the ST-100 in the vertical orientation [21], the lowest temperature reached was 8 K. However, as discussed later, such shroud is not compatible with the usual working distance of commercial reflective objectives when working in transmission.

3.3 Pressure measurement

It is impossible to predict the pressure within the cell solely by the knowledge of the pressure applied to the membrane. Thus, pressure near the sample is determined by measuring the pressure-dependent wavelength shift $\delta\lambda$ of the R_1 ruby fluorescence's line as shown in Fig. 3.9(a). A green 532 nm 15 mW laser is used as excitation source. The pressure in GPa is calculated [32] with

$$P(\delta\lambda, R_1) = 1884 \left(\frac{\delta\lambda_p}{R_1}\right)\left[1 + 5.5\left(\frac{\delta\lambda_p}{R_1}\right)\right] \tag{3.1}$$

where $\delta\lambda_p = \delta\lambda - \delta\lambda_T$ is the only pressure-dependent contribution to the wavelength shift and $\delta\lambda_T$ is the only temperature dependent shift which has been measured by Occeli in Ref. [33] and is expressed in Å as:

$$\delta\lambda_T = \begin{cases} -8.9, & \text{if } T < 50\text{K}, \\ 6.67 \cdot 10^{-2}\Delta T + 7 \cdot 10^{-5}\Delta T^2 - 2.3 \cdot 10^{-7}\Delta T^3 \end{cases} \tag{3.2}$$

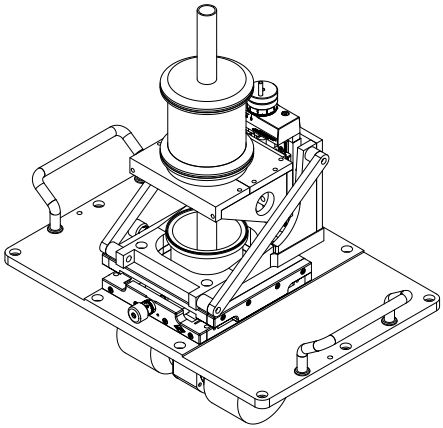

Figure 3.8 – 3D view of the DAC camp mounted onJanis ST-100 cryostat supported by custom designed vacuum-tight triple axis manipulator

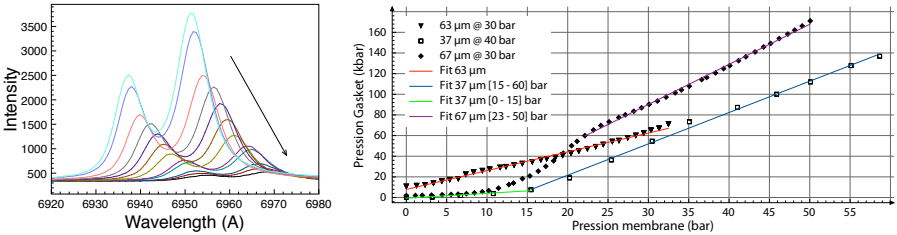

Figure 3.9 – (a) Fluorescence spectra of ruby under pressure with shift of the $R_{1,2}$ lines. (b) Pressure run on two gasket geometry showing different behavior upon membrane pressure increase. From [21].

where $\Delta T = T - T_{ref}$ for $T \leq 300$ K. The pressure can be determined in real-time thanks to an automated workflow implemented in LabView performing in loop the following operations: temperature and fluorescence measurements, multi peaks (gaussians and baseline) fitting for the determination of the position of the R_1 line and finally pressure calculation as described in Appendix A. As one can see in Fig. 3.9(b) displaying the evolution of pressure inside the gasket for increasing membrane pressure for two gaskets geometry, the behavior is rather different which confirms the necessity of such pressure determination while performing an actual measurement.

3.4 High pressure optical setups

The lack of space around the DAC is the issue that was the original motivation to conceive and build an optical setup allowing to reach low temperature while allowing the use of regular objectives. The geometry of the DAC and the working distance of reflective optics (as discussed later in section 3.5) imposed that both have to be placed in a custom vacuum shroud [21]. Because of thermal deformation upon cooling and mechanical strain resulting of the shroud evacuation the DAC, one needs to be able to remotely adjust its position in order to perform proper focus which is achieved by a vacuum-tight XYZ stage shown in Fig. 3.8 supporting the whole cold finger of the ST-100 and designed to withstand the force applied by the atmospheric pressure.

The reflectivity however does not require to have the optics sharing the same environment as the DAC due to its slight asymmetric geometry 3.4.2 and therefore allows the use of a commercially available infrared microscope, which in our case is a Hyperion from Bruker. Since it is impossible to operate the whole system (spectrometer and microscope) under vacuum in order to minimize the optical absorption of various gazes present in ambient air, the interior of the Hyperion is purged by a slight overpressure of nitrogen, which also increases the stability of the signal.

3.4.1 Transmission

The setup itself is shown in Fig. 3.10 and is designed to be placed directly into the sample compartment of a commercial Bruker FTIR 66 v/S spectrometer [34] as pictured in the inset. The IR incoming (1) beam's nominal IR focal point (3) provided by this instrument is steered to the upper vacuum chamber of our set-up and steered back to the nominal optical path of the spectrometer by two gold plated one inch diameter mirrors on kinematic accuators (2). This pair of mirrors can be easily slid away using a translation stage in order to recover the original beam path useful for initial adjustment. The guard vacuum of the cryogenic part of our set-up needs to be better than the lowest pressure reached by the spectrometer (gas bearings of the interferometer ~ 5 mbar). Therefore, the upper chamber is separated from the compartment chamber by a pair of appropriate IR transparent windows (5): Quartz,

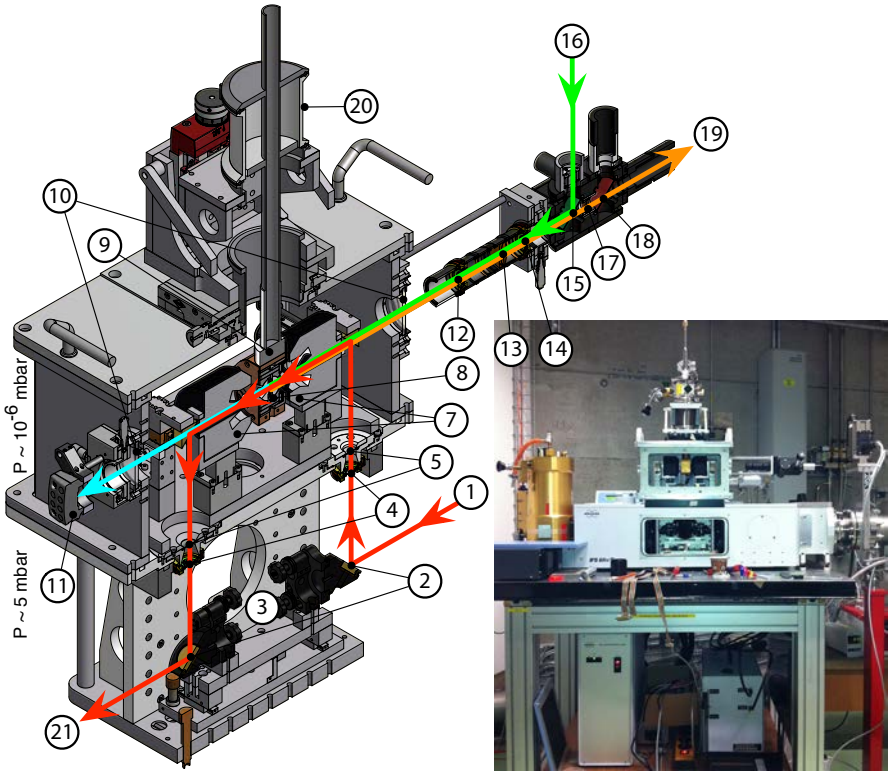

Figure 3.10 – Transmission setup in 3D cut view. Infrared is in red, laser excitation in green, ruby fluorescence in orange and visible light collected by camera in blue. Inset shows the setup mounted on the 66v at SLS IR Beamline. Technical drawings of the major parts are in Appendix B.1.

KBr and Polypropylene for NIR, MIR and FIR spectral region respectively. At the equivalent focal point there is a variable size diaphragm (4) used to adjust the diameter of the illuminated area within the sample chamber inside the DAC (8) in the focal plane of the Cassegrain objective (7). The beam is further steered into the right $15\times$ magnification coefficient Cassegrain objective, $NA = 0.5$ mounted on a 3-axis translation stage. The mirrors of this Cassegrain are aluminum-coated in order to also optimize the spectrum in the visible range for the fluoresence measurement. The original housing (20) of the cold finger (9) is attached to a custom-made XYZ-manipulator, designed to withstand the force resulting from the pressure difference, and used to position with precision the sample into the focal point delivered by the Cassegrain objective. It is of utmost importance to be able to move the DAC independently from the optics, in order to perform *sample* and *reference* measurements as shown in Fig. 3.11(a) and (c). On the left side of the DAC, the outgoing light is collected by a second Cassegrain objective (7) with gold coated mirror and otherwise same specifications. The IR beam is then steered back into the original spectrometer's nominal beam path towards the detectors chamber (21).

The gold-coated one cm^2 steering mirror (6) in front of each Cassegrain objective can be replaced (custom-made miniature motorized linear translation stages) by a beamsplitter which is used to visualize the sample within the DAC with the CCD Camera (11) placed after a Quartz window (10). The translation stages can also completely clear the optical axis to perform the fluorescence measurement which is done in the following way: the parallel laser beam exiting the collimator of an optical fiber (16) is reflected by a green dichroic mirror (15). A variable size diaphragm (14) allows to tune the intensity of the beam which is then collimated by a 50 mm achromatic doublet (13) before passing thru a second size variable diaphragm (12) controlling the size of the laser spot entering into the right Cassegrain. The fluorescence light is collected in reflexion and shares in reverse the same path until the green dichroic mirror that is crossed by the red light which is then collimated by a 50 mm achromatic doublet (17) before crossing a red dichroic mirror (18) and been fed at last to another optical fiber (19) connected to a HR2000+ spectrometer from Ocean Optics that operates in visible light and is optimized for fluorescence measurement (laser excitation rejection).

Optics from (12) to (19) are mounted in a rigid ensemble whose position can be adjusted to match the rear focal point of the right reflective objective hence properly illuminating rubies inside the DAC.

3.4.2 Reflectivity

Although the high pressure Infrared capabilities in reflectivity geometry have already been partially described in Ref. [35], where a Bruker Hyperion 3000 infrared microscope coupled to a Vertex 70V spectrometer is used in combination with a similar DAC, the reflectivity setup presented in Fig. 3.12(a) is actually an adaptation of the

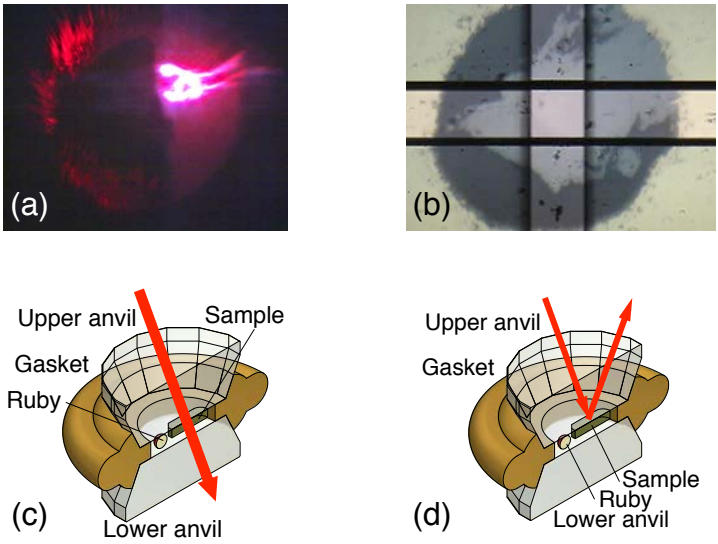

Figure 3.11 – Sample environment in the different geometries (a) Gasket hole with synchrotron light spot next to crystal sample; as seen with the camera (11) in transmission. (b) Hyperion's camera view of sample area delimited by field-stop blades in reflectivity. (c) Cut view of the sample environment with light passing through the sample. (d) Sample environment in cut view with light reflected by the sample.

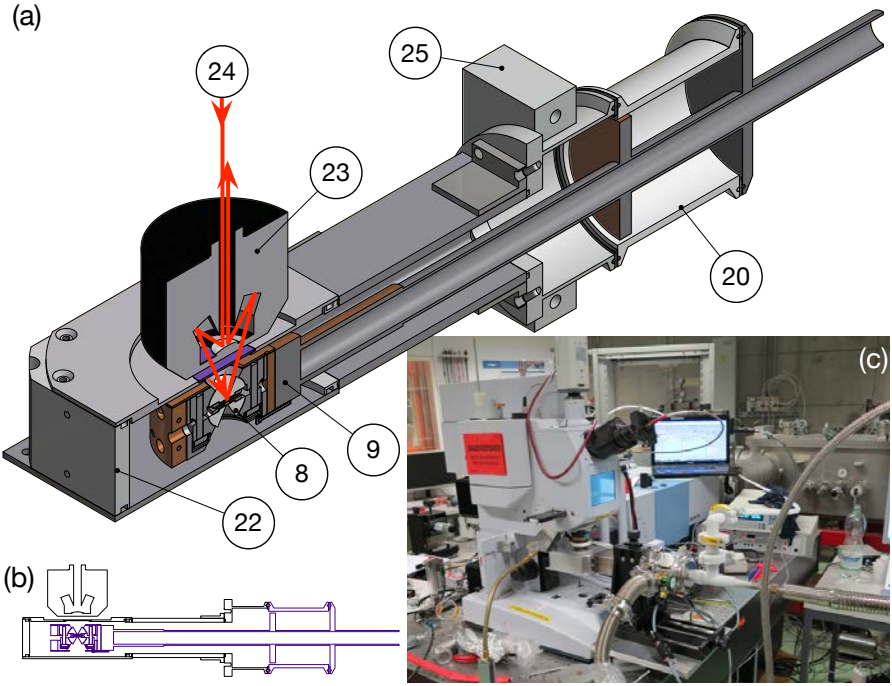

Figure 3.12 – Reflectivity setup (a) in 3D cut view where Infrared is in red. (b) Shared parts with the transmission setup drawn in purple. (c) Reflectivity setup mounted on the Hyperion 3000 microscope at SLS IR beamline. Technical drawings of the major parts are in Appendix B.1.

DAC (8) clamped on the coldfinger (9) housing ensemble (20) of Fig. 3.10 to the geometry of the Hyperion (parts commonly shared with the transmission setup are drown in purple in Fig 3.12(b)). Our home-made vacuum shroud (22) with a geometry of sufficiently low profile allows to use the standard $15\times$ reflective objective of the microscope (23) with working distance of about 24 mm thus keeping its original IR optical path (24). The positioning of the whole cryostat is achieved by an OWIS triple-axis transition stage thus allowing to precisely put the sample at the focal point of the condenser in order to make the sample and reference measurement. A coarse adjustment of the tilt along the axis of the cold finger is possible (25).

Such cryostat can also be used to perform Raman spectroscopy under high pressure and at low temperature.

As described previously [35], ruby excitation is achieved by feeding a laser beam directly into the optical path of the infrared beam at the optical coupling of the spectrometer and the microscope. Fluorescence light is collected into a fiber optics through one of the eyepiece exits of the Hyperion and then analyzed by the same Ocean Optics spectrometer.

3.5 Optical coupling

Working with (infrared) light and bringing it into an area so confined as a sample in a DAC is a difficult task for many reasons. First, in order to reach such elevated pressure the diameter of the hole in the gasket containing the sample is rather small (less than 250 μm). Moreover, in the case of a single crystal study, the sample *has* to be even smaller (less than 100 μm of diameter) which immediately implies that without additional focusing optics, only a tiny portion of the photons that would normally illuminate a sample of more usual size (more than one mm of diameter) got to interact with the sample inside the DAC. Secondly, this technique also implies diamond anvils of 1.5 mm of thickness leading to a strong attenuation of the intensity of the transmitted beam at each pass which decreases again the photon count. Such limitations substantially drag down the intensity of the light that might eventually reach the detector and the only way to overcome this problem is to focus the spectrometer's light beam in order to reduce its spot size. This calls for the use of non diffractive objectives (Schwarzschild type), at least in the infrared. This kind of optics is composed of two aligned spherical mirrors which implies that for the same working distance and numerical aperture as their diffractive counterparts (which work fine in the visible range) they present a much more significant form factor. This immediately stands in opposition with the limited space usually available around the rear of the anvils and thus limits the magnification factor and/or the numerical aperture of objectives that might be used: as shown in Fig. 3.4, the DAC has a construction requiring a minimal working distance of at least 15 mm and its optical access with an conical aperture forming a 60° angle, corresponds to a numerical aperture of 0.5. As presented above in section 3.4, $15\times$ 0.4 N.A. Newport objectives were used in

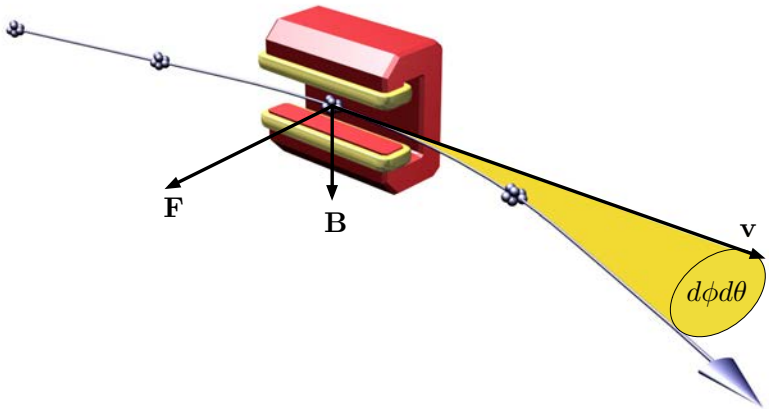

Figure 3.13 – Sketch of a synchrotron light cone production by bending the trajectory of moving charged particles, adapted from [37].

reflectivity on the Bruker 2000/3000 Hyperion microscope [36] whereas in the case of the transmission setup, 15× 0.5 N.A. Ealing objectives were used in our custom made setup allowing more space around the DAC.

The standard coupling between the Bruker Vertex 70v and the Hyperion 3000 microscope has been modified from the original commercial design and is based on two planar mirrors which maintain the size of the light spot, thus reduces losses [35].

3.5.1 Black body light source

The sources discussed in the previous section are either blackbody sources in the case of the MIR (SiC) and NIR/VIS range (tungsten) or in the FIR range a gas-discharge lamps (Hg). In any case, the introduction of new optical components in the light's path will not increase the total *useful* number of photons emitted by the spectrometer's light source that might reach the detector and will only reduce the losses (finite efficiency). This now allows to identify that the remaining limitation is actually the light source itself.

3.5.2 Why synchrotron light?

Synchrotron radiation is the emission of photons provoked by the bending of the trajectory of moving charged particles. This is achieved in large scale synchrotron facilities where these charges are circulating in a storage ring and pass through various stages aiming to successively accelerate and deflect these charges thus producing localized light extraction spots around the ring. Due to the relativistic speed of the charged particle, the photon emission occurs in a very narrow cone tangentially to the

initial particle velocity as shown in Fig. 3.13. These main characteristics of a light source are captured by the so called *brillance* which is conventionally defined as

$$\text{Brillance} = \frac{\Phi}{(d\theta d\phi)(\text{A})(0.1\%\text{bandwidth})} \tag{3.3}$$

where Φ is the total flux of photons per second in the forward direction, $d\theta d\phi$ is the product of the angular dispersion of the beam in mrad^2 and A is the cross section of the beam in mm^2.

The brightness of a synchrotron light source vastly exceeds the one of a thermal source (as one can see in Fig. 3.14(a)) since its angular dispersion and and its source size are much smaller and the photon flux higher[3]. One notices that synchrotron radiation allows a broader energy range, which is particularly useful in low energy part of the spectrum which is probed by FIR-THZ experiments.

For all these reasons, one realizes that when conducting single crystal infrared high pressure spectroscopy the access to a synchrotron light source is a key requirement. During this work, measurements were carried out at the X01DC infrared beamline of the Swiss Light Source, Paul Sherrer Institut in Villigen, where optical diagnostic, alignment and additional hardware conception were conducted. Fig. 3.14(b) shows the Bruker 66/v with the coupling box of the beamline which uses one elliptic and one parabola mirror to perform the injection of synchrotron radiation directly into the interferometer. The general layout of the 70v coupled to the Hyperion is analogous except for the presence of an aperture wheel and the use of the left side exit port of the spectrometer used for coupling to the microscope.

Fig. 3.14(c) shows a comparison in the MIR (MCT detector and KBr beamsplitter) between different spectrometer aperture sizes for the built-in thermal source and the synchrotron light source whose size is of the order of the millimeter. The light is focused by $15\times$ 0.5 N.A. objectives and goes through the DAC with a gasket of 250 μm diameter. The inset shows the analog-to-digital level for all configurations and reveals that the level obtained with synchrotron light is about 12 times higher compared to the one of a similar aperture-defined thermal source. Fig. 3.14(d) shows the transmitted intensity in FIR (helium cooled bolometer and 6 μm mylar beamsplitter) for a 4.8 mm diameter-wide thermal source (with analog gain set to 1000) resulting in a 12'000 photons count, compared to a synchrotron light spot of 1mm (gain 200) with a 16000 photons count. This indicates that, compared to a thermal source, about four times wider, the synchrotron light displays an ADC level 13 times higher.

On both these measurements, one also notices that the synchrotron spectrum displays a higher intensity in the high (and low) energy part as expected from a thermal light source.

[3]Not to mention that since the photon emission happens in very narrow pulses spread in time due to the charge accelerating process, the resulting Φ is also larger during the pulse,

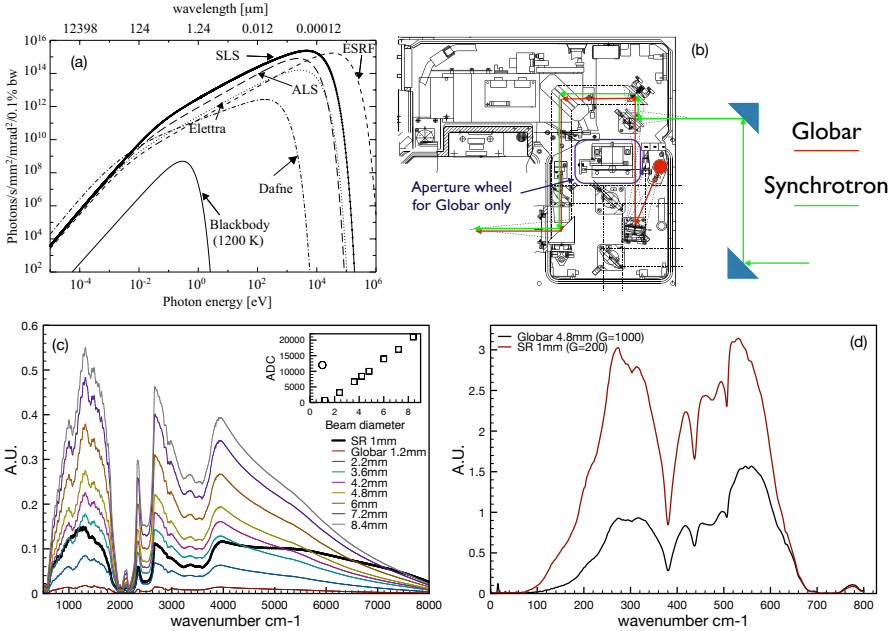

Figure 3.14 – (a) Calculated brillance as a function of frequency for several synchrotron and blackbody light sources from [38]. (b) Parts of the optical layout of the IFS 66v/S with internal light source path and synchrotron light injection (adapted ted from [34]) (c) Single channel intensity spectrum of light passing through a 250 μm diameter gasket by two $15\times$ 0.5 N.A. confocal reflective objectives for different diameters of the thermal light source and comparison with synchrotron light at X01DC infrared beamline of SLS. The inset reports the photons count of the analog-digital-converter of the IFS Bruker 66v/S. (d) Single channel spectrum in FIR.

In order to investigate the focusing performance of the optics used in the transmission geometry, we took profit of the three-axis manipulator of the DAC and precisely moved it in the plane perpendicular to the steered light beam and looked at the effect induced on the signal intensity in FIR (which is in principle the worst case since the wavelength is higher). With synchrotron light, no significant drop of intensity occurs for displacements up to about 90 μm, above which the decrease occurs very quickly thus indicating that the diameter of the spot of synchrotron light is about 70 μm. On the contrary, the slightest displacement of the DAC results in a very fast decrease of signal intensity. Knowing that the focused light spot is of a sufficiently small size, comparable to the one of a sample, and yet still yields a high photons count, makes the access to a synchrotron light source the key ingredient to secure when considering experiment under pressure. Analogous investigations concerning the size of the synchrotron light spot on the Hyperion microscope of the beamline have been conducted and concludes to results in the same order of magnitude [35].

CHAPTER 4

BiTeI: A Topological Insulator under High Pressure?

Les hommes croient ce qu'ils désirent.
L'expérience, voilà le maître en toutes choses.
Jules César

4.1 A brief introduction to Topological Insulators

Topological Insulators (TI) are a very particular type of materials exhibiting several rather exotic properties among which the existence of conducting surface states is the most remarkable. On the band structure side, the simple picture of an insulator is a fully occupied valence band separated from an empty conduction band by the so-called energy gap with the Fermi energy lying within thus forbidding conduction, whereas in contrast, the simple picture for a metal is the location of the Fermi energy either in the conduction or the valence band. The TI have the special property to share a bit of both these pictures: the conducting edge states appear as narrow bands linking the valence band to the conduction band coming from the insulating bulk.

Ever since their theoretical prediction followed by their first experimental manifestation, they have drawn a quickly growing portion of the scientific focus, thus producing a very rapidly increasing number of publications and numerous reviews, as for instance Refs. [39**?**]. On the application side, they nourish strong hopes in the *spin*-tronics domain to one day replace the transistors. In contrast to their cousin in *elec*-tronics acting as switches of currents of charge, TI could act as switches of current of spins that would flow without dissipation, hence potentially solving the

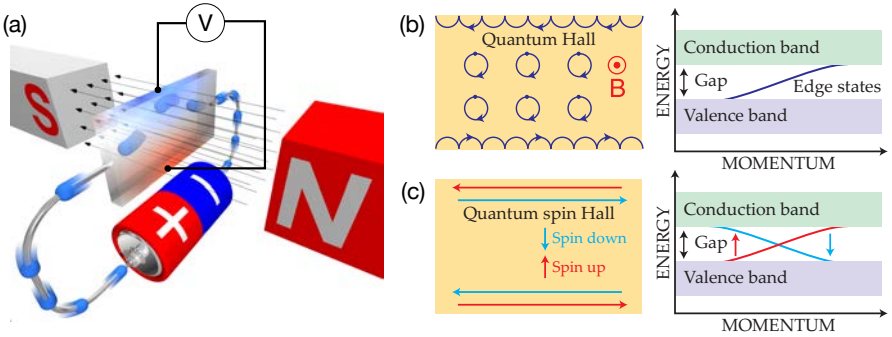

Figure 4.1 – (a) Sketch of the effect induced on charged particles traveling within a material by the application of a perpendicular magnetic field: bending of trajectories and a transversal (Hall) tension appears on the edges. Adapted from [42]. (b) Quantum hall effect with closed cyclotron orbits, charge conduction on both edges of the material and sketch of corresponding band structure (c) Quantum spin hall effect with spin current on the edge. From [43]

problem of Joule heating in todays' microprocessors industry.

Before briefly explaining how one's interest might have been drawn toward BiTeI, one might find useful to make a brief historical excursion by the Quantum Hall effect and the other interesting phenomena its discovery allowed.

4.1.1 Digression (on the Quantum Spin Hall effect)

This effect, discovered in 1980, is the quantized version of the classical hall effect, discovered a little more than a century earlier [40]. Let's consider a parallelepiped wire as shown in Fig. 4.1(a) in which is flowing a current resulting of the motion of charge carriers along the conductor. If a perpendicular magnetic field is applied to the wire, the motion of the charge carriers is affected by the appearance of the Lorentz force which is always perpendicular to the motion of the charge. Carriers of opposite charge sign tends to separate on opposite sides of the conductor by bending their initial trajectories. At equilibrium, this asymmetric charge distribution creates an electric field preventing further charge separation. In the case where the trajectory of the charge carriers is only slightly curved by the magnetic field, the result of this charge separation is the appearance of a transverse potential difference V_H called Hall tension which is linearly dependent on both current intensity and magnetic field. One can also notes that a so called anomalous version of the Hall effect occurs in some ferromagnetic materials, with an often higher amplitude [41].

However, the motion of the carriers can also be strongly driven away from their initial trajectory. If the Lorentz force is of sufficient magnitude, some of the carriers can be forced to circulate in closed orbits (cyclotron motion as shown in Fig. 4.1(b)) thus

ceasing to contribute to both longitudinal and transverse transport properties giving rise to the Quantum Hall Effect (QHE). This was first observed by the application of a large magnetic field of several Tesla on a gaz of electrons confined into a two dimensional plane at very low temperature by von Klitzing on metal-oxide-semiconductor field-effect transistor [44] in 1980. The manifestation of QHE is the appearance of *plateaux* in the Hall conductivity $\sigma_{xy} = I/V_H = \nu e^2/h$, ν being an integer. Also, the resistance in the longitudinal direction exhibits perfect cancellation in-between *plateaux* of conductivity. The semi-classical explanation of this phenomena is found in the quantization of the radius of the orbitals where the trapped charge carriers are confined. The other carriers participate at electrical transport through a half cyclotron motion made possible at the boundaries of the conductor, as shown in Fig. 4.1(b). Moreover, due to the presence of the magnetic field, all carriers of the same sign can only scatter in a given direction at the sample boundary which suppresses the influence of impurities.[1]

Such exotic phenomena happening to charge can also occur for spin, which is in this case the Quantum Spin Hall Effect where no charge separation (so no Hall voltage) but only a spin separation on the edges appears, as represented in Fig. 4.1(c), thus preserving the time-inversion symmetry otherwise broken by the application of a magnetic field which is here effectively replaced by the spin-orbit interaction. Such realization was predicted on Quantum Wells of mercury telluride in 2006 by Bernevig *et al.* [45] then observed one year later by König *et al.* [46]. By varying the thickness of a sandwiched layer of HgTe (negative energy gap of -300eV) surrounded by CdTe (energy gap of 1.6eV) acting as a barrier, it was possible to tune the band structure of the inner layer thus passing from a CdTe-dominated non-inverted band gap (Fig. 4.2(b)) to an inverted gap (Fig. 4.2(b)). However, regardless of the thickness of the sample, a quantized conductance was observed and attributed to conducting surface states, thus proving experimental evidence of the quantum spin Hall effect or the two-dimensional *topological insulator* state.

Such experiments performed under particular conditions (very low temperature and high magnetic field or low temperature and gating) however preclude the use of photo-emission experiments as a probe of the band structure which would be most useful to asses the topological nature – or not – of the materials suspected to exhibits topological insulator properties.

4.1.2 3D Topological Insulators

The alloy of $Bi_{1-x}Sb_x$ which was previously intensively studied for its many peculiar properties such as thermoelectric properties, was the first material to be predicted to be a 3D topological insulator by a prediction by Fu and Kane [48]. Bismuth has a very anisotropic band structure with both hole and electron pockets due to the overlap

[1] A more rigorous description of the QHE phenomena is to be looked at by quantum mechanics but it was deemed unnecessary for the score of this basic approach to the TIs.

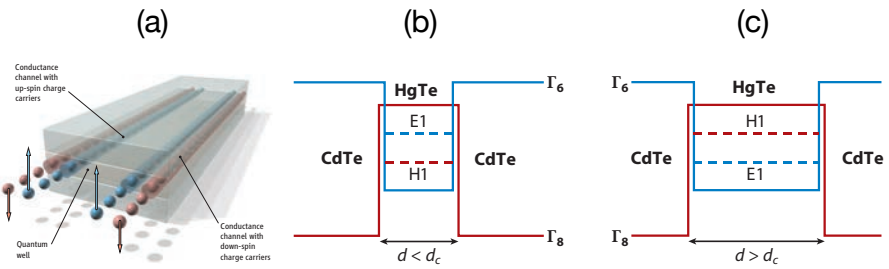

Figure 4.2 – (a) Spin polarized conduction along the edges in a quantum spin hall material, from [46]. (b) Band structure of the CdTe/HgTe/CdTe heterostructure's lowest-lying sub-bands for the trivial insulator state and (c) the nontrivial QSH insulator state, from [47].

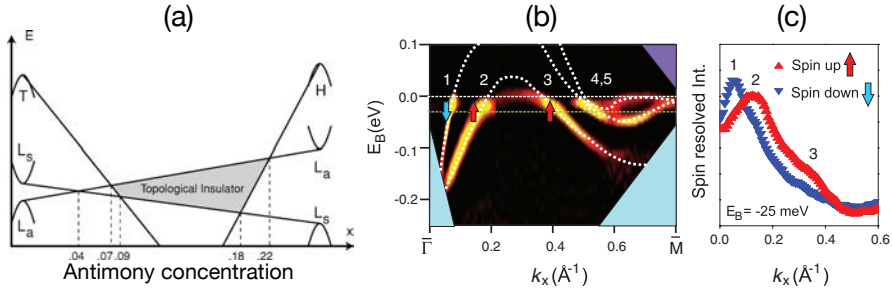

Figure 4.3 – (a) Band structure of $Bi_{1-x}Sb_x$ as a function of doping x, adapted from [48]. (b) ARPES data showing 5 bands crossing the Fermi level and (c) spin-resolved data indicating the spin polarization of the bands, from [49].

of the Fermi level with the conduction band (L point) and valence band (T point). The band structure can be continuously changed when antimony is progressively taking the place of bismuth as shown in Fig. 4.3(a) with the effect of crossing the valence and condition bands at the L point at $x = 0.04$ (thus passing from a semimetal to a semiconductor) while the conduction band of the T point is lowered and crosses at $x = 0.07$ the newly inverted valence band of the L point. While x continues to increase, the hole H band from Sb rises and cross the L conduction band at $x = 18$ and finally the L conduction band at $x = 0.22$ thus turning back into a semimetal. So in the window where $0.07 \leq x \leq 0.22$ the material is a semiconductor with an inverted band gap and therefore would present the properties of a topological insulator with protected surface states. These predictions were quickly followed by ARPES investigations by Hsieh *et al*. [49] imaging the band structure below the Fermi level which reported the observation of bands crossing the Fermi level at five points as shown in Fig. 4.3(b). The spin-resolved study indicated the spin-polarisation of the band attributed to the conducting surface states in Fig. 4.3(c), indeed concluding to the observation of the first 3D topological insulator with a bulk gap 50 meV.

As pointed out by [**?**], since $Bi_{1-x}Sb_x$ is a rather complicated alloyed material, much energy has been spent into finding materials with simpler band structure with only one Dirac point to investigate TI phenomena. Such materials were quickly found in other Bismuth-based compounds: Bi_2A_3 where A = Te or Se. This material has many advantages: Bi_2Te_3 has a larger band gap of 0.3 eV, is easier to synthesize, and best of all, exhibits topological insulator properties at room temperature as reported by Chen *et al.* [50].

Near the Fermi level, the bands structure, as represented on Fig. 4.4(a), shows the usual bulk valence and conduction band (BVB and BCB) separated by the Energy gap, but more interestingly the two bands corresponding to the surface states (SSB) with linear dispersion whose intersection (also called Dirac point) occurs at Γ point of the Brillouin zone. A spin-resolved ARPES study further indicated that the Dirac cone is spin polarized as shown in Fig. 4.4(b) bringing final confirmation of the TI nature of the material.

One notices that the Dirac point lies below the highest value reached by the valence band and that the Fermi level passes through the conduction band. This seems rather distant from the idealized TI having both its Dirac cone and the Fermi level within a well defined gap, *i.e.* a true bulk insulator with conducting surface states [**?**].

4.2 BiTeI

4.2.1 Basic ID

For all the reasons mentioned previously, topological insulators have been at the center of scientific spotlight for about half a decade and their list continues to expand. BiTeI is a rather *old* material and reports in the literature goes back at least to 1951

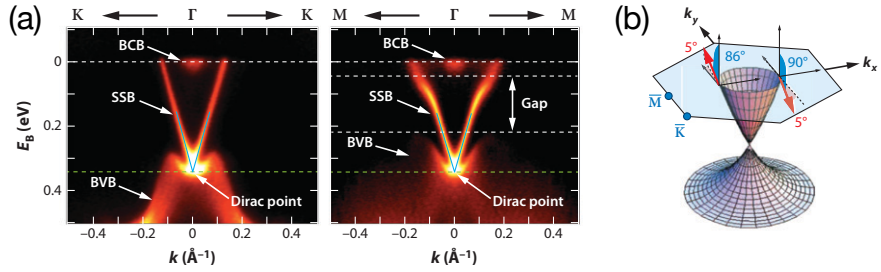

Figure 4.4 – Bi_2Te_3: (a) ARPES data imaging both $\Gamma - K$ and $\Gamma - M$ direction the Bulk valence and conduction bands (BCB and BCB) connected by surface states band (SSB) crossing at the Dirac point. (b) fitted spin polarization of the surface state based on SR-ARPES data. From [39, 50].

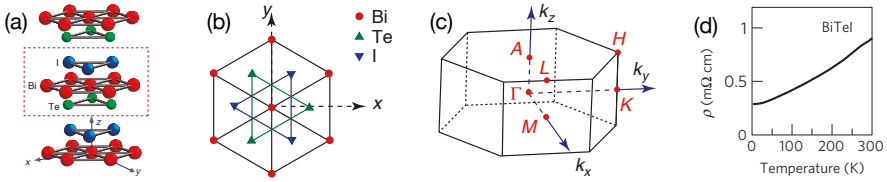

Figure 4.5 – (a) Perspective view enlightening the layered crystal structure of the compound in real space with a unit-cell indicated in dashed lines, (b) top-view of the same hexagonal structure showing the intercalation of atomic layers, (c) Brillouin's zone in reciprocal space. Adapted from [53, 54].

with a crystallographic study reporting an hexagonal structure [51][2]. In 1970, an optical study [52] was perform in reflectivity and transmission and reported an optical gap of 0.4 eV, a carrier density[3] of $3.5 - 7.6 \cdot 10^{19}$ cm^{-3} and a value of the high frequency dielectric function $\epsilon_\infty = 14.5 \pm 1.5$.

The structure, as shown in Fig. 4.5(a), is described by the noncentrosymmetric space group $P3m1$ [55]. The unit cell of BiTeI (Fig. 4.5(b)) is composed of triple layers, Te–Bi–I, stacked along the c-axis. The triple layers are bound by a weak van der Waals interaction. Since the structure lacks inversion symmetry, it is polar and produces an electric polarization along the z direction thus inducing an effective magnetic field in the frame of rest of the relativisticly moving xy plane electrons which will couple to their spin (spin orbit coupling). This field induces a lifting of degeneracy of the spin up and down energy distributions $E_{\uparrow\downarrow}(\mathbf{k})$ by shifting in momentum the otherwise superposed spin-degenerate parabolic dispersion curves as

[2]Interestingly, this structural paper already discusses the structure of nothing else than Bi_2Se_3 and Sb_2Te_3 which are nowadays known to be 3D topological insulators.

[3]Obtained by Hall measurement.

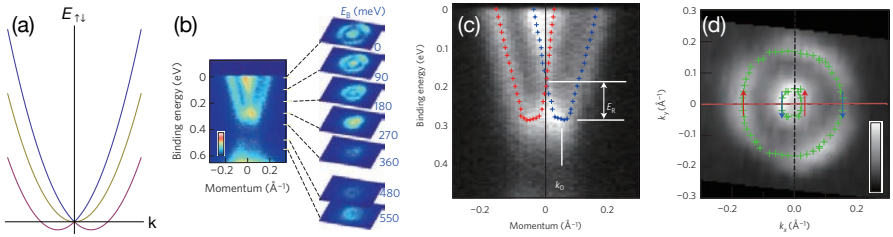

Figure 4.6 – (a) Sketch of the energy distribution of a degenerate parabola and the two spin-polarized parabolae from the RSS. (b), (c) and (d) show ARPES and SR-ARPES data near the Γ point confirming the occuring of Rashba spin splitting in BiTeI. Adapted from [53].

shown in Fig. 4.6(a) which is know as the Rashba spin splitting (RSS) [56–58]:

$$E_{\uparrow\downarrow}(\mathbf{k}) = \frac{\hbar^2\mathbf{k}^2}{2m^\star} \pm \alpha_R\,|\mathbf{k}| \tag{4.1}$$

where $m^\star$ is the effective mass of the electron. From this new dispersion follows, the appearance in constant energy cuts of two concentric circles on which the revolution of polarization vector is opposite. Not only this effect, characterized by the so called Rashba parameter $\alpha_R = 3.8$ eVÅ has been reported in BiTeI [53] with the observation of the two split spin-polarized parabola as shown in Figs. 4.6(b-d) but its magnitude is such that α_R reaches the highest value for a bulk compound which of course triggered much attention, [53, 59, 60] in particular in perspective of spintronic research.

Rashba spin splitting however is not an effect restricted to the surface of the material and would be a property of the bulk. A study with infrared optical spectroscopy [61] was performed over samples of different carrier concentration in order to extract the optical conductivity Figs. 4.7(a-b). Several spectral features in the conductivity are attributed to the energy limits of direct transitions occurring within a Rashba spin split band structure, in agreement with *ab initio* calculation of the optical conductivity. These transitions are represented in Fig. 4.7(c) and are the following: α and β set the upper and lower limits of the intraband transitions occurring between the Fermi level and the conduction bands and γ (respectively δ) sets the lower limit for transitions between the upper (lower) branch of the split valence bands and the Fermi level. The γ onset is associated with the energy gap. Since the penetration depth of infrared radiation is of several microns, the bulk nature of Rashba spin splitting is confirmed.

The symmetry analysis gives four zone-center vibrational modes, with the irreducible vibrational representation

$$\Gamma = 2A_1 + 2E \tag{4.2}$$

All of them are both Raman and infrared active because of the lack of inversion

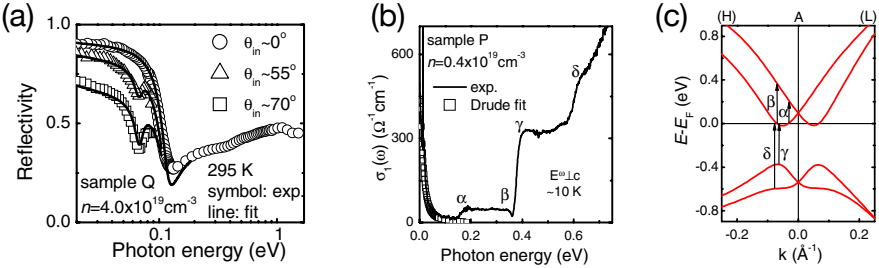

Figure 4.7 – (a) Reflectivity of BiTeI for different angles of incidence and the corresponding (b) optical conductivity where are labeled spectral features related to (c) allowed transitions within Rashba spin split bands. Adapted from [61].

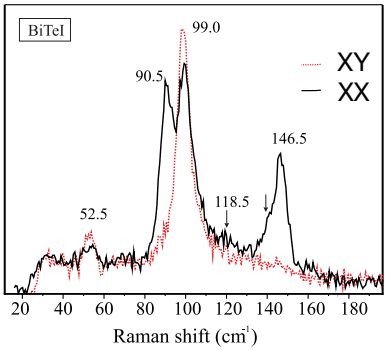

Figure 4.8 – Raman shift spectrum at ambient pressure, from [62].

symmetry and were observed by different Raman studies [62, 63] as shown in Fig. 4.8 and the assignment of these modes is $A_1(1) = 90.5$, $A_1(2) = 146.5$, $E(1) = 52.5$ and $E(2) = 99.0$ cm^{-1}. While both A_1 and E modes are visible in XX polarized light, only E modes are seen in XY polarization.

Noticing the very similar electronic structure of BiTeI with well known Bi_2A_3 topological insulators systems [64, 65], a first principle band structure study [54] predicted that by the application a *moderate* hydrostatic pressure, one might turn this trivial insulator into a topological one by inducing a band touching between the lowest conduction bands of Bi and the highest valence bands of Te or I lying in the $A - H$ direction, as depicted in Fig. 4.9(a). In fact, the decrease of atomic distances would not only affect the crystal field splitting, but also the spin orbit coupling, and therefore the Rashba spin splitting. Such mechanism strongly affects the value of the band gap, as shown in Fig. 4.9(e): below p_c (Fig. 4.9(b)), an increase of pressure induces a reduction of the gap which closes at $p = P_c$ (Fig. 4.9(c)) above which a band

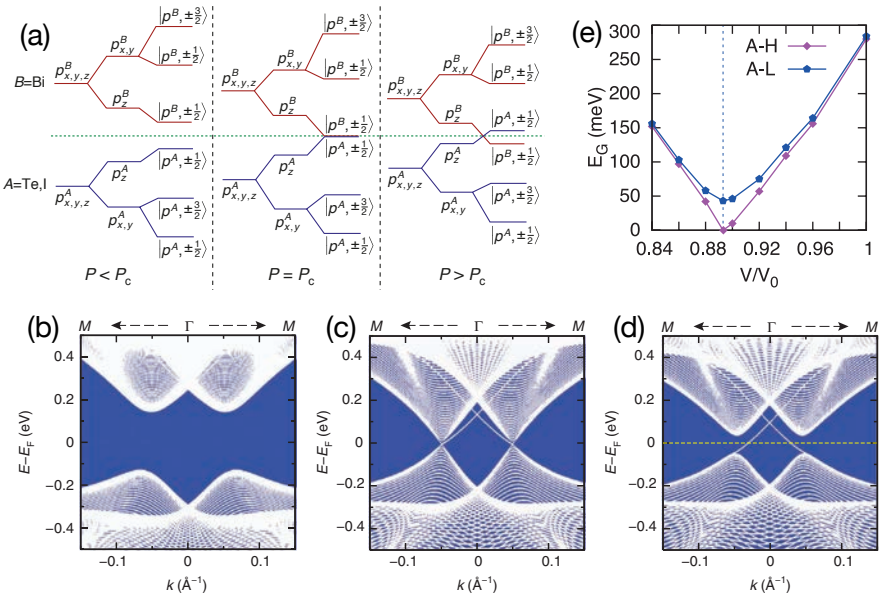

Figure 4.9 – (a) Energy level of p orbitals of Bi, Te and I with successive inclusion of chemical bonding, crystal-field splitting and finally spin orbit coupling for hydrostatic pressure, below, at and above a critical pressure P_c. (b), (c) and (d) show the band structure near the A point for the corresponding pressure regimes. (e) represents the evolution upon pressure increase of the energy Gap. Adapted from [54]

inversion occurs thus opening an inverted band gap (Fig. 4.9(d)). The gap closing is also accompanied with a doubling of the α_R Rashba spin splitting parameter. The critical pressure is estimated to be in the $1.7 - 4.7$ GPa region, which constitutes nowadays a commonly accessible pressure range for high pressure experiments.

If such topological transition were to happen it would promote BiTeI to be the first noncentrosymmetric topological insulator. It would in principle also provide a way to tune *in situ* this material from the insulating to the topological insulator phase thus allowing to conveniently investigate both phases as well as the transition itself which for several reasons [39] has proven to be a difficult task to carry with well known topological insulators such as Bi_2Se_3 since for instance chemical doping isn't an option because it changes of crystal structure. If pursuing on the chemical doping path, one must turn to more complex material like $TlBi(S_{1-x}Se_x)_2$ whose structure remains unaffected by the S/Se ratio [66–68]. However intrinsically, this technique requires a dedicated sample at each concentration and therefore does not allow a reversible and well controlled transition crossing. For that particular reason, BiTeI represents a very interesting playground for investigation.

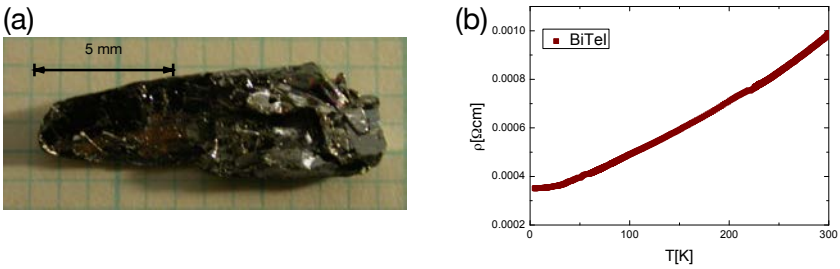

Figure 4.10 – (a) Single crystal of BiTeI grown by the floating zone method provided by A.Ubaldini and (b) its resistivity at ambient pressure as function of temperature.

4.2.2 BiTeI Samples

Single crystals of BiTeI (Fig. 4.10(a)) were grown by the floating zone method, starting from the stoichiometric ratio of metallic bismuth, tellurium and bismuth iodide. The electrical transport shown in Fig. 4.10(b) has a metallic behavior down to low to liquid helium temperature and very well agrees with value of the litterature.

4.2.3 Optical properties at ambient pressure

In view of the previous optical study [61], optical conductivity is well suited to probe the band structure of BiTeI under pressure in order to investigate the influence of pressure over the $\alpha, \beta, \gamma, \delta$ spectral features which are the fingerprints of the Rashba spin splitting effect and look after a possible topological transition. It is, of course, out of the question to probe the existence of surface states rather than *merely* probing the realization (or not) of a necessary condition for the topological insulator phase to occur under pressure which is a gap closure and re-opening.

We start our investigations by an ambient pressure optical study on a freshly cleaved $a-b$ surface. In far and mid-infrared (FIR and MIR), near normal incidence reflectivity measurement with a Bruker 113 evacuated spectrometer in a ultra high vacuum cryostat using a incandescent tungsten light source. MIR measurement in the $600-6000$ cm^{-1} range were made with a MCT liquid nitrogen cooled detector and a KBr beamsplitter while FIR measurements below 650 cm^{-1} required the use of liquid helium cooled bolometer detector and a 6 μm-thick mylar beamsplitter. As discussed in chapter 2, the renormalization of the sample's spectrum is performed by an in-situ gold evaporation. The higher spectral region ranging from $0.6-5.6$ eV was covered with a Wase ellipsometer from Woollam with another UHV cryostat with compatible sample holder and the obtained data was used to extend the reflectivity in the visible range. The level of the MCT data served as reference in respect of the lower and higher energy range data. Transmission was measured on a thin flake of 6 μm with an

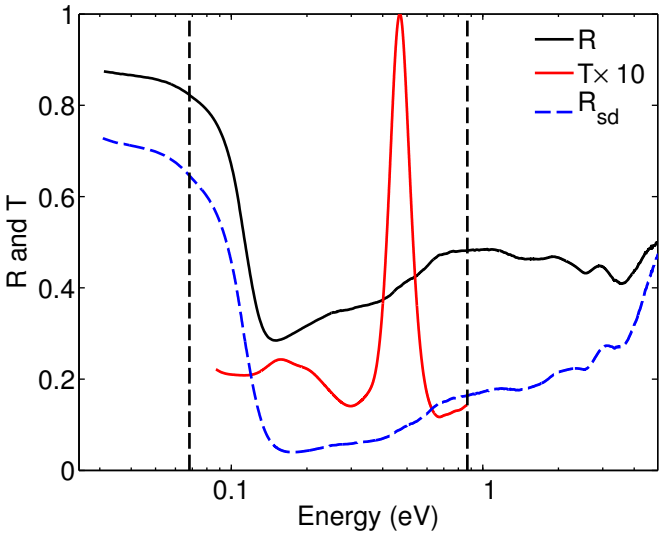

Figure 4.11 – The sample-vacuum interface reflectance and transmission ($10\times$ magnified) and the reflectance calculated at the sample-diamond interface. The dashed vertical lines mark the energy range where the high-pressure reflectivity experiments were performed.

Bruker Hyperion 2000 Infrared microscope. Reflectance and transmission data are shown in Fig. 4.11 at ambient pressure and room temperature. A sharp plasma edge appears in the reflectance at 0.15 eV, and near 0.4 eV a kink is observed. Transmission in the mid infrared range displays a maximum around 0.45 eV, which matches the frequency of the kink in the reflectivity. Another small peak in the transmission is observed at 0.15 eV and concurs with the plasma edge in the reflectance.

Kramers-Kronig transformation of the reflectivity data is used to obtain the complex optical conductivity $\tilde{\sigma}(\omega)$, equivalently yielding the complex dielectric function $\tilde{\epsilon}(\omega)$ which allows to calculate the expected reflectivity $R_{sd}(\omega)$ at the diamond-sample interface that displays similar features as the reflectivity with a plasma edge in the same position.

The real part of the optical conductivity $\sigma_1(\omega)$ shown in Fig. 4.12(a) is gapped below ~ 0.5 eV, which is just above the energy of the maximum in transmission. Simultaneously, a Drude contribution emerges below 0.1 eV which agrees with the metallic behavior of the resistivity as well as with the previous optical studies [61, 69, 70]. This metallic contribution is very likely due to the impurity doping and a slight off-stoichiometry, particularly of iodine because of its high fugacity. We attribute the fine structures in the optical conductivity displayed in the inset of Fig. 4.12(a) to the interband transitions α and β, and the onset of absorption (gap edge) γ, as sketched in the insets of Fig. 4.12(b) [61, 69, 70]. Such transitions represent a good

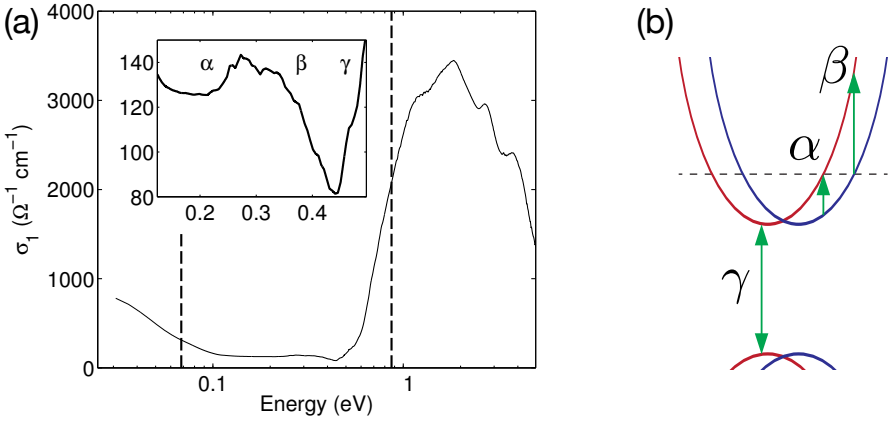

Figure 4.12 – (a) Real part of the complex conductivity $\sigma_1(\omega)$.The inset shows a blow-up from a region of $\sigma_1(\omega)$ containing the spectral features α, β and γ. The dashed vertical lines mark the energy range where the high-pressure reflectivity experiments were performed. (b) Sketched band structure with allowed transitions.

fingerprint of the Rashba spin splitting, and of the energy gap in particular which is a crucial parameter that one required to grasp the topological properties of the material. It is therefore relevant to perform infrared spectroscopy on BiTeI as a function of increasing pressure.

4.2.4 High-Pressure

Optical data at high pressure were acquired up to 15 GPa with a diamond anvil cell at the X01DC IR synchrotron beam line of the Swiss Light Source [35, 71]. Reflectivity was determined in the frequency range from 60 meV to 1 eV for a dense set of pressures. The intensity of radiation reflected from the diamond to sample interface was normalized by the intensity from the interface between the diamond and the metallic (Cu-Be alloy) DAC gasket. Pictures of the sample inside the pressure cell are displayed in Fig. 4.17(b-c) before and after the pressure run.

The reflectivity ratios measured in the DAC were calibrated against $R_{sd}(\omega)$ obtained from the absolute reflectivity measured outside the cell. In order to calculate the complex dielectric function $\hat{\epsilon}(\omega)$ the reflectivity data were fitted for all pressures to a Drude-Lorentz expression with a sufficiently large number of oscillators with the variational dielectric function fitting [12] (as described in the previous chapter) used so as to reproduce all fine details of the reflectivity spectra. Transmission was measured from 80 meV to 1 eV for a fine mesh of pressure points. Raman spectra at high pressure were recorded using the same DAC up to 15 GPa, with daphne oil 7373 as pressure medium and a home-made micro Raman spectrometer.

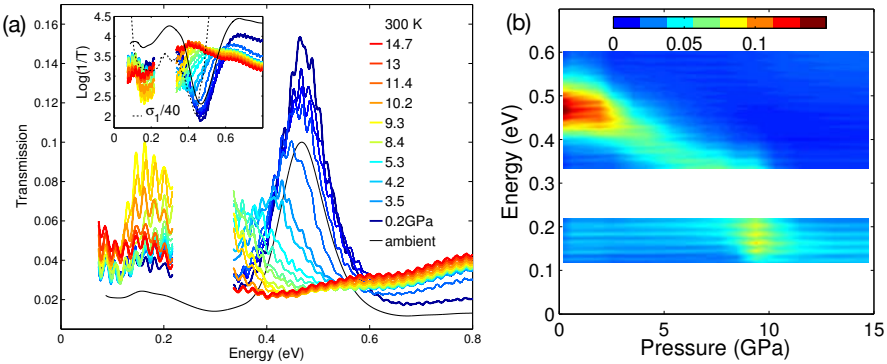

Figure 4.13 – BiTeI under high pressure at room temperature. (a) Transmission curve. The region of the diamond absorption is discarded. The inset shows an approximation of the real part of $\sigma(\omega)$. (b) Colorplot of the same data, best showing the gap closure at 9 GPa.

4.2.4.1 Transmission

The transmission at room temperature, shown in Fig. 4.13(a), features a sharp peak at 0.46 eV at low pressure, just below the band gap. It agrees with the ambient pressure transmission shown in black. The position of the transmission maximum redshifts with pressure and diminishes in intensity. This decrease in the maximum intensity is particularly sharp at 3 GPa. The monotonic decrease terminates in an abrupt disappearance of the peak at 9 GPa which is best seen in a colorplot as displayed in Fig. 4.13(b). The collapse of the transmission peak above 9 GPa suggests that a phase transition is taking place at this pressure. This is in agreement with the reflectivity and the optical conductivity, which indicates that above 9 GPa the gap feature in $\sigma_1(\omega)$ is gone.

One can approximate the optical conductivity based on the transmission data (2.59) as shown in inset of Fig. 4.13(a) along with the actual optical conductivity that has been scaled-down by a factor of 40 to ease the comparison. The overall trend matches well the one of optical conductivity except at both the boundaries of the spectral range where the up turns aren't well reproduced. However, the optical features α, β and γ are easily distinguishable (at least at ambient pressure) and points-out an asymmetric evolution of the gap with pressure where only a closing is observed without re-opening.

At the time of the experiment, only transmission measurements were possible at low temperature and were carried at 20 K. The effect of the temperature does not affect the behavior of the energy gap which is monotonically closing up to 9 GPa as shown in Figs. 4.14 and 4.15 and gives similar qualitative optical conductivity as shown in the insets.

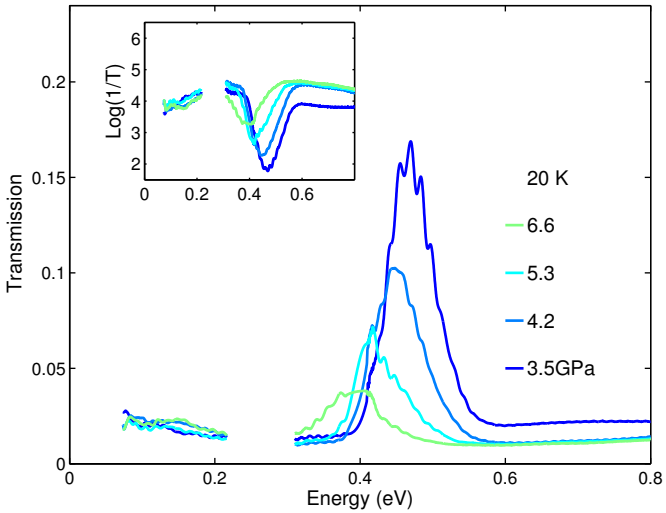

Figure 4.14 – BiTeI Sample A under high pressure at low temperature. Transmission shown for 4 pressures. Inset indicates an approximation of the real part of the optical conductivity.

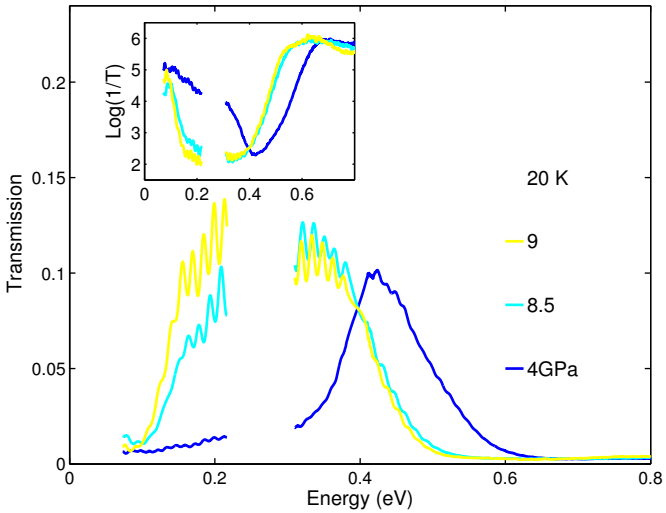

Figure 4.15 – BiTeI Sample B under high pressure at low temperature. Transmission shown for 3 pressures. Inset indicates an approximation of the real part of the optical conductivity.

4.2.4.2 Reflectivity

Figure 4.16(a) shows the reflectivity as a function of photon energy for various pressures. The reflectivity is measured at a sample-diamond interface, and the levels may be compared to the R_{sd} shown in Fig 4.11. The lowest pressure curves contain Fabry-Perot resonances at frequencies just below the gap onset, due to the small sample thickness and the sample transparence. The reflectivity in Fig. 4.16(a) has a sharp plasma edge at 0.15 eV, consistent with Fig. 4.11. Very little change is observed up to 7 GPa, and the plasma edge remains at the same energy. There is, however, a gradual increase of the reflectivity level at frequencies above the plasma edge, and a decrease of the level below the plasma edge. Above $\sim$ 7 GPa, the plasma edge suddenly begins to shift towards lower energies, and at 9 GPa it starts to gradually smooth out. Above 9.5 GPa, the plasma edge disappears, and the reflectivity level now increases across the entire photon energy region. For the highest pressure reached no plasma edge is observed, but the reflectivity has an upturn towards low energies suggesting a metallic state. Overall, the reflectivity experiences a dramatic pressure-induced change in the studied energy range.

Below 9 GPa, the Drude contribution persists almost unchanged, and the high-frequency $\sigma_1(\omega)$ indicates a gradual shift of the absorption edge towards lower energies. This means that below 0.2 eV there is little change in $\sigma_1(\omega)$, whereas above 0.35 eV $\sigma_1(\omega)$ increases as the gapped states become filled. As the absorption edge shifts, the dip in $\sigma_1(\omega)$ at 0.45 eV gradually disappears with increasing pressure. Above 9 GPa, the Drude contribution disappears from our energy window and $\sigma_1(\omega)$ becomes rather flat below 0.2 eV. Around this pressure the slope of $\sigma_1(\omega)$ changes sign at low energies, from negative to positive. As the pressure increases further, the gap edge shifts more rapidly to lower energies. By 12 GPa, the low energy states (below 0.2 eV) have been filled and the gap tends toward very low energies. At the highest reached pressures, the gap in $\sigma_1(\omega)$ appears to be zero or very small. There are two clear limiting cases for the optical gap. At zero pressure, the gap is finite (~ 0.4 eV), and remains above ~ 0.3 eV up to 9 GPa. At 15 GPa the conductivity is not gapped at room temperature. We cannot attach a precise value to the gap above 9 GPa because it is not accompanied by a clear spectroscopic feature.

Figure 4.17(a) shows $\sigma_1(\omega)$ as a function of pressure, for a series of photon energies ranging from 0.068 eV to 0.74 eV. Common to all the curves is a sharp kink at $p \sim 9$ GPa. This confirms that at 9 GPa a phase transition takes place which influences the electronic structure. Above 9 GPa, $\sigma_1(p)$ steeply increases in the whole energy range. The optical conductivity σ_1 at 0.068 eV shown in Fig. 4.17 (corresponding to the lower limit of our experimental window of observation), the optical conductivity spectra shown in Fig. 4.16(b) and the transmission spectra in Figs. 4.13 to 4.15, have a gradual variation as a function of pressure between 0 and 9 GPa.

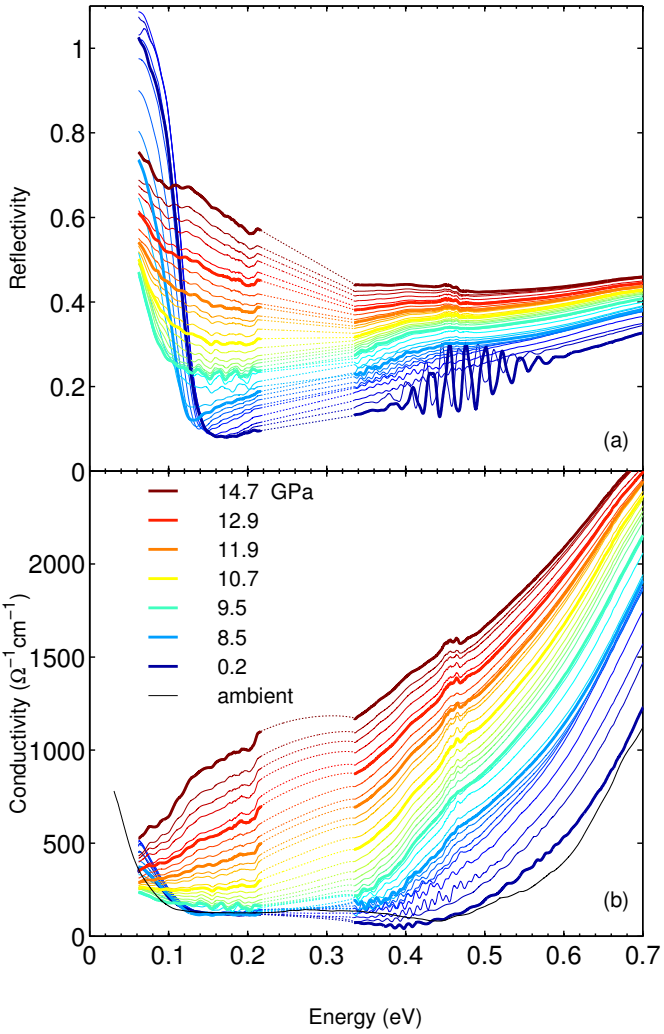

Figure 4.16 – (a) Reflectivity shown for different pressures (legend in panel b). (b) Real part of the optical conductivity, $\sigma_1(\omega)$. In all panels, the data between 0.22 and 0.33 eV are not shown due to strong diamond absorption.

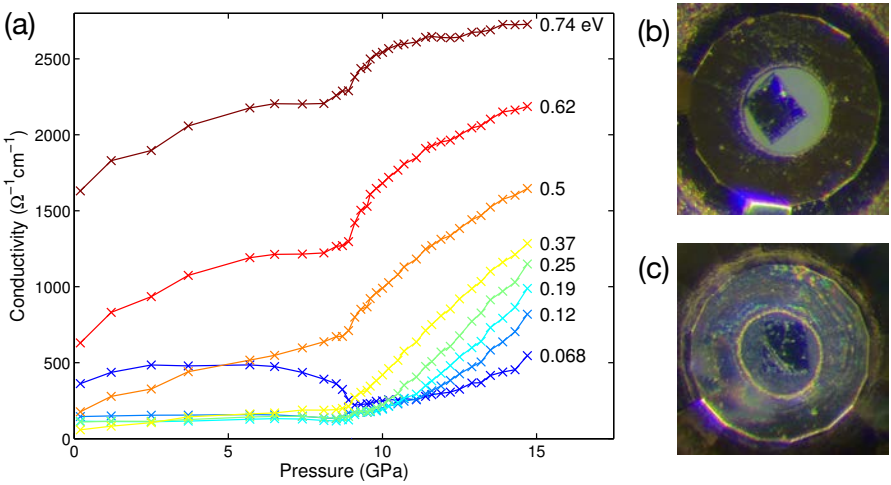

Figure 4.17 – (a) Cut of the conductivity at constant energy. (b) Picture of the sample within the gasket's hole before the pressure run and after (c).

4.2.4.3 Raman Spectroscopy

To gain better understanding of the transition at 9 GPa, we measured the pressure effects on the optical phonons using polarized Raman spectroscopy from 0 to 15 GPa, shown in Fig. 4.18. At ambient pressure, parallel polarization shows $A_1(1) = 94$, $A_1(2) = 150$ and $E = 102$ cm^{-1}, while crossed polarization shows $E = 102$ cm^{-1}, in agreement with the previous studies [62, 63]. Around 2 GPa both A_1 modes diminish in the parallel polarization and at the same time appear in the crossed polarization. While this may be related to a gradual change in the crystal lattice, there is no theoretical argument why a topological phase transition would have this effect on the Raman spectra. Besides the expected blueshift of the Raman modes under pressure, an important effect is observed above 9 GPa: three modes are visible up to 9 GPa, above which the spectrum changes abruptly and several weak peaks appear. The appearance of new vibrational lattice modes points to a change of crystal structure at the pressure where the change in optical conductivity also takes place.

4.3 Discussion

One of the most striking aspects of the presented data is the abrupt disappearance of the plasma edge for $p \simeq 9$ GPa in the reflectivity. The sharp low-pressure plasma edge originates in a well defined Drude peak in $\sigma_1(\omega)$, which suggests a coherent charge transport in the low pressure phase ($p < 9$ GPa). To better illustrate the pressure dependence of the plasma frequency, Figs. 4.19 shows the loss function,

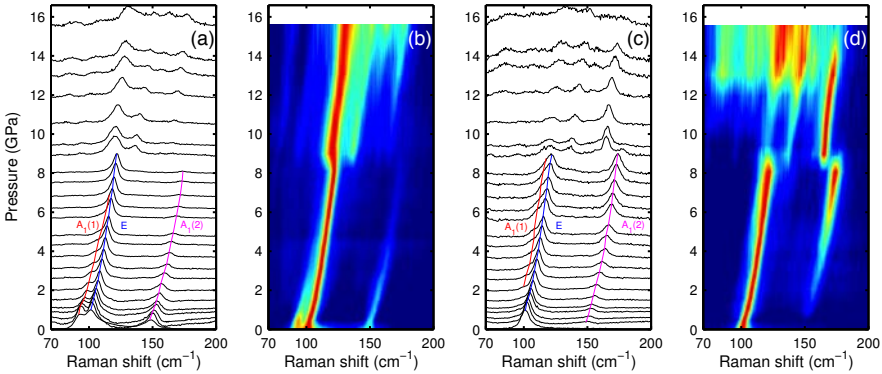

Figure 4.18 – Raman spectra of BiTeI from 0 to 15 GPa. (a) and (b): parallel polarization. (c) and (d) crossed polarization.

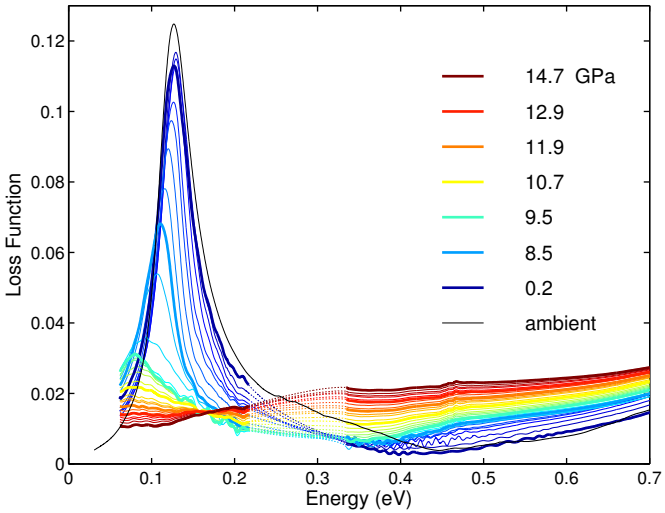

Figure 4.19 – Electronic loss function as a function of pressure. The data taken between 0.22 and 0.33 eV are not shown due to strong diamond absorption.

$-\mathrm{Im}(1/\hat{\epsilon})$. A maximum in the loss function corresponds to the screened plasma frequency. At ambient pressure we observe one such mode at 0.13 eV and associate it with the intraband plasmon. This plasmon mode widens with pressure and slightly bends towards lower energies above 3 GPa, without appreciable pressure dependence up to 9 GPa. The loss function remaining constant means that the spectral weight of the Drude contribution does not change much. However, at 9 GPa the peak in the loss function suddenly vanishes. The dramatical disappearance of the plasmon peak is not due to the disappearance of the free carriers: there still has to be a Drude contribution at highest pressures, since the reflectivity has clear Hagen-Rubens upturns at low energies. Instead, the conductivity $\sigma_1(\omega)$ increases above 9 GPa and this sudden increase in the conductivity produces very strong damping. The plasmon thus becomes overdamped by background conductivity and appears washed out. High pressure pushes the interband transitions close to zero energy, and above 9 GPa they become strongly mixed with the tail of the Drude peak.

In view of our optical data, i.e. transmission directly exhibiting monotonic decrease of the energy gap and optical conductivity obtained by Kramers-Kronig transform of the reflectivity showing a progressive gap filling, the scenario of a symmetric behavior of the energy gap around a critical pressure appears clearly ruled out, since the necessary condition of the topological insulator picture is not met.

The appearance of several additional Raman active modes above the critical pressure is unambiguous evidence for a change of crystal structure, in agreement with the XRD data and other high pressure raman studies [72–74]. Yet the optical conductivity in Fig. 4.16(b) progresses gradually through this phase transition as a function of pressure, and has a kink at 9 GPa for all infrared photon energies. Therefore we postulated that the high-pressure phase is structurally close to the one at ambient pressure (space group $P3m1$ with 3 atoms per unit cell), and mainly differs by the stacking of Bi-Te-I layers. A good candidate was the space group $P6_3mc$ with 6 atoms per unit cell, which is the structure of the chemically related compound BiTeCl at ambient pressure [55]. Our *ab initio* calculations imposing the latter crystal structure for pressurized BiTeI, indicates that in this phase the gap also decreases gradually as a function of pressure, and evolves toward a topologically trivial semimetallic state characterized by a negative gap. This hypothesis about the structure is also consistent with the observation that the main Raman lines are only slightly shifted above 9 GPa and several other weak lines appear. However, on mention that another closely related structure, namely the $Pnma$ one, was also investigated and showed an insulating behavior, which was incompatible with our experimental observation. The structural study of Chen *et al.* [73] arrived to an other conclusion by indicating that the $Pnma$ structure was energetically favored (in the LDA-GGA framework) and whose calculated XRD pattern was compatible with their experimental high pressure powder XRD patterns (it was however admitted that the crystal structure could not be identified only based on the XRD pattern).

4.3.1 GW band structure calculations

The recent interest focussed on BiTeI is, as we mentioned, due in particular to first-principles calculations [54] indicating that a topological phase transition might appear under pressure through the inversion of the energy gap. This first study gave an estimation of the value of the critical pressure to lie between 1.7 and 4.1 GPa, based on Local Density Approximation (LDA) and Generalized Gradient Approximation (GGA).

It was however pointed out [75] that the approximation of the gap value and the Rashba parameters are very sensitive to the method of calculation: GW calculations, taking into account many-body quasiparticle corrections, show a larger value of the gap (~ 0.38 eVm, more in agreement with the experimental data [75]) than the LDA predictions. Fig. 4.20(a) displays for nods of the k-space mesh the energy difference $E - E_F$ as a function of the nods corresponding energy. One notices a discontinuity of about 0.35 eV above the Fermi level between the highest point of valence band and the lowest point in the conduction band which is of course identified as the energy gap and well agrees with the experimental value lying close to 0.4 eV. The difference between the LDA+GGA band structure calculation with the GW calculation and, in particular, the effect on the energy gap, is shown in Fig. 4.20(b) and it indeed mostly consists in a Gap increase near the A point.

Such an increase of the electronic band gap in the topologically trivial regime would effectively result in a positive shift of p_c [76]. Our *GW* calculations estimate $p_c \sim 10$ GPa as shown in Fig. 4.20(d). Fig. 4.20(c) shows a sketch of the dependance obtained by GW calculations of the band of Bi and Te/I respectively below, at and above the critical pressure which is analogous to the previous GGA predictions [54]. Therefore, owing to its higher magnitude, the gap evaluated by GW calculation, is expected to close for a more elevated pressure which would result in turn in a topological phase transition occurring only at a higher pressure.

4.3.2 Other high pressure studies

At the same time as our paper [77] was under writing, an analogous study appeared on arXiv [78] then PRL [72] which consists, first, in an X-Ray powder diffraction investigation of the lattice parameters of the unit cell of BiTeI. The ratio of a/c was found to be minimal near $2 - 2.9$ GPa which is identified as P_c since a change of the nature of the bond between Bi $6p_z$ and Te/I $5p_z$ orbitals from ionic ($P < P_c$) to covalent ($P > P_c$) upon pressurisation is suggested. A metallic bonding between p_z orbitals from Bi and Te is predicted at $P = P_c$ where the fluctuation of charge would increase the compressibility of the material in the z direction. Therefore, the reported lowering of spacing between staked ab planes is interpreted as a manifestation of a topological phase transition. Above 7.9 GPa a structural phase transition is detected based on the complexification of the diffraction pattern. Secondly, both middle infrared reflectivity R and transmission T were measured at several pressures. The

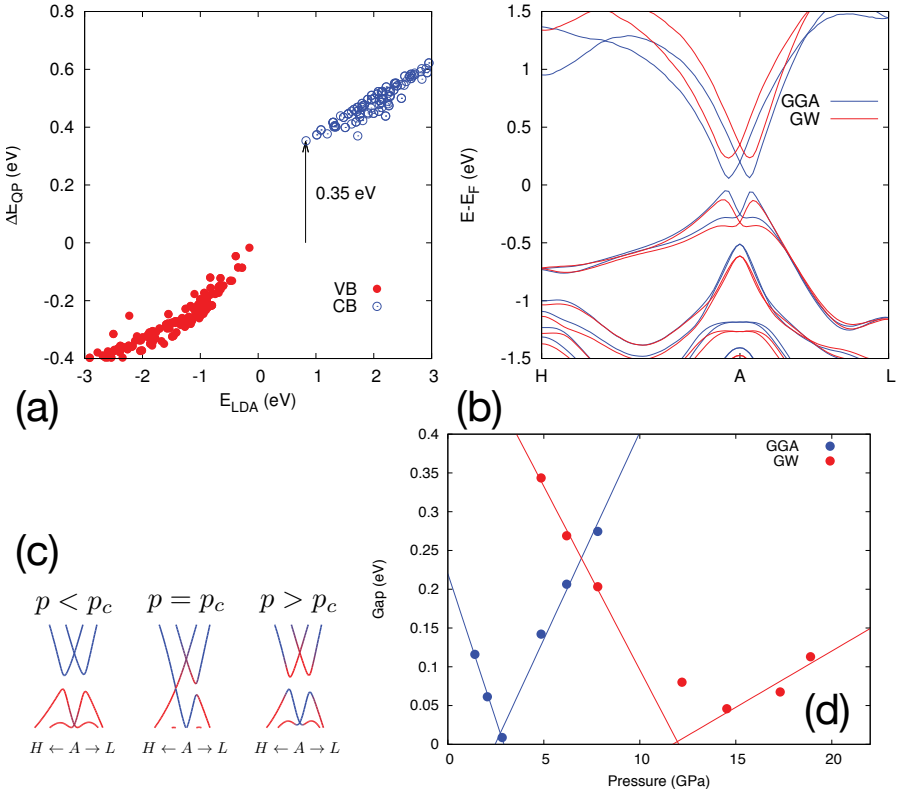

Figure 4.20 – (a) Energy difference $E - E_F$ for all nods in the k-space mesh. (b) Comparison of the band structure of BiTeI obtained by GGA and by GW calculation. (c) Sketches of the band structure, below, at and above the critical pressure p_c. (d) Evolution of the energy gap with pressure for GGA and GW calculations.

optical conductivity $\sigma_1(\omega)$ was calculated from n_1 and n_2 which were retrieved using an iterative solving procedure on the expressions of $R(n_1, n_2)$ and $T(n_1, n_2)$ and the plasma edge frequency ω_p was extracted from a Drude-Lorentz fit of the low energy part of the reflectivity. The results are an observation of a maximum in both the extrapolated zero-frequency conductivity and plasma frequency occurring at 2.2 GPa and thus interpreted as manifestation of the closing and re-opening of the Energy gap, *i.e.* to the observation of the topological transition.

The structure of the HP phase was studied by Chen *et al*. [73] by means of X-ray scattering joined with calculations/refinements and states that the crystal structure at high pressure phase is $Pnma$ (and not $P6_3mc$) with 4 formula units per unit cell and which would be compatible with the occurrence of a topological phase transition with pressure (the $Pnma$ HP phase is insulating). This structure was also considered during our own ab-initio band structure calculations but was precisely discarded because it didn't reproduce a metallic behavior at high pressure. One notes that their calculated critical pressure lies at 6 GPa, whereas their experimental value is closer to 4.5 GPa which is in itself higher than observed by Xi *et al*. [72]. It is rather surprising to see GGA-based calculation producing energy gap in agreement with experimental values. Regarding the methodology, one might find questionable to perform band structure calculations to asses its topology by disregarding the spin orbit coupling for a material precisely known to host a strong Rashba spin splitting which is specifically due to a strong spin orbit coupling [53, 59].

A parallel russian polarized Raman study by Ponosov *et al*. [74] exhibited the same conclusion regarding the occurrence of a structural phase transition at 9 GPa. Furthermore, in analogy with other materials such as Bi_2Se_3 which are *already confirmed* topological insulators, they associated the presence near 3 GPa of a minimum in the linewidth of the E mode in the XY geometry as a consequence of the occurrence of a topological transition. They suggest low temperature measurement to clarify the anormalous linewidth decrease of the E mode.

A transport experiment by Van Gennep *et al*. [79] under both magnetic field and hydrostatic pressure shows the apparition of a second oscillatory frequency in the resistance at pressures of $\sim 0.3 - 0.9$ GPa. In particular, the chemical potential is indicated to rise above the crossing point of the Rashba spin-split bands (misleadingly called Dirac point) hence passing from a regime with a single Fermi surface (single oscillation) to a regime with the appearance of a another (and rather small) fermi surface attributed to the inner Fermi surface with opposed spin polarization as seen in Fig. 4.6(d). The bottom of the Bi conduction band is reported to be lowered of about 10 meV thus being only in qualitative agreement with the band structure calculation of [54] predicting a gap closing. The speed at which this lowering occurs is indeed much smaller than the $\sim$ 70 meV predicted ($\sim 7\times$, which could agree with our conclusion). The study concludes by a rather prudent statement: *further studies at higher pressures and in lower carrier density samples will be necessary to explore the possible appearance of novel surface states in the high-pressure non-centrosymmetric*

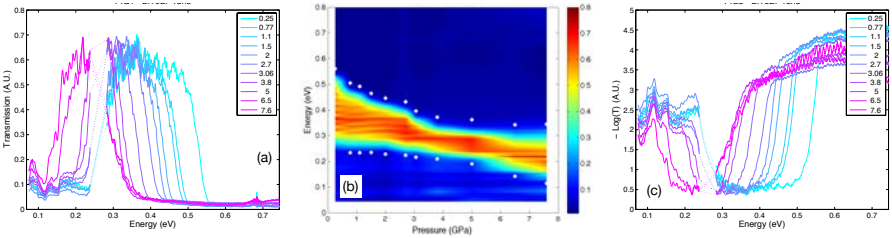

Figure 4.21 – Transmission spectra from 0 to 8 GPa of BiTeBr.

topological insulator phase.

4.3.3 Preliminary results on BiTeBr

The transmission spectra of the BiTeI chemically-related BiTeBr are shown in Fig. 4.21(a) (dashed lines indicate the region of the diamond absorption). Since the renormalisation is difficult to determine with all experimental constraints, the amplitude of the transmission spectra is therefore not absolute and one should focus only on the position of the spectral feature – in particular, we very well distinguish that the boundaries of the transmission windows of these compounds are redshifting with pressure (shown in white dots in the colormap in Fig. 4.21(b)). Even though the limited pressure range ($p < 8$ GPa) covered was sufficient to observe significant qualitative changes in the spectra, it however did not allow the observation of a gap closure since the value of the gap at ambient pressure of BiTeBr is already larger than the one of BiTeI which required as we saw at least 9 GPa to close. We note the presence of transmission at lower energy which is an artifact that we attribute to contamination of the "sample" spectrum by a fraction of the light not passing through the sample. Therefor we discarded such small features. Concerning a further analysis of the data, the lack of reflectivity data a priori precludes a quantitative calculation of the optical conductivity as it was done in our previous study of BiTeI since it is based on a variational dielectric function fitting of the reflectivity. However, one can obtain an qualitative approximation of the optical conductivity as shown in Fig. 4.21(c). Further experiments are scheduled to reach higher pressure and gain access to reflectivity to allow better data fitting.

4.4 Conclusions

To summarize, we have determined the pressure dependence of the optical properties and Raman vibrational modes of BiTeI, under pressures up to 15 GPa. The band structure and the interband transitions were expected to be strongly influenced by pressure [54] which is, indeed, what we measured: the reflectivity and transmission

show dramatic changes under pressure. The band gap monotonically decreases as a function of increasing pressure and the optical conductivity increases. At 9 GPa this process is accelerated. As a result, the interband plasmon becomes overdamped above 9 GPa. The transmission data demonstrate clear evidence of a phase transition at 9 GPa, corroborated by the pressure-dependent Raman spectra indicating a sudden change to a different crystal structure at this pressure.

However, our GW calculations, which more accurately describe the magnitude of band gap, indicate a gap closing for the P_3m1 ambient pressure phase occurring at 10 GPa, which is higher than the observed phase transition and therefore possibly prevents the predicted topological high-pressure phase in BiTeI from occurring.

In order for our data to be consistent with a quantum phase transition in the range $1.7 - 4.1$ GPa as predicted in Ref. [54] and the signature of which was for instance reported in Ref. [72], it would be necessary that either the full process of closing and reopening of the gap is completed in between the pressure points of Fig. 4.17 (*i.e.* within a pressure window of about 0.5 GPa) or that the location of the chemical potential of our samples was so close to the bottom of the conduction band (low carrier concentration) [61] that the distinction between β and γ transitions within the Rashba spin-split band structure would become hard to distinguish. However this seems very unlikely since both our data in transmission and reflectivity unambiguously indicate a gap edge monodically redshifting with pressure.

Moreover, there is the usual problem with topological insulators as well stated by Hasan *et al*. [80]: *Topological insulator materials need to be perfected so that they actually insulate*

CHAPTER 5

Lithium Purple Bronze under High Pressure

You might very well think that;
I couldn't possibly comment.
Francis Urquhart in *House of Cards* by Michael Dobbs

The compound known as lithium molybdenum purple bronze (LPB) is a member of the broader molybdenum *bronzes* $A_xMo_yO_z$ family where A is occupied by an Alkali metal. The name bronze is inherited from the rather metallic look of the samples which is complemented by a color grading depending on the actual composition that changes the color of the reflected light [81]. In this chapter we will discuss the compound LPB whose chemical formula is $Li_{0.9}Mo_6O_{17}$ and which was first synthesized by Greenblat *et al.* in 1984 [82]. Although it was initially considered to be a quasi two dimensional material [83] with strong transport anisotropy owing to the observation of a conducting axis and an insulating one, it was later identified as a quasi one-dimensional material after the study of its crystal structure [84]. For this reason, this material attracted much attention which should be viewed in the perspective of the previous efforts put in the extensive investigation of the Bechgaard salts. These materials are organic compounds which feature several exotic properties (aside from extreme fragility) that showed to be strongly influenced by external pressure; in particular superconductivity and low dimensionality. The last aspect eventually lead by means of optical spectroscopy to the observation of a temperature-induced dimensionality cross-over by Jacobsen *et al.* [85] and also to the first realization of a Luttinger liquid by Schwartz *et al.* [86].

As we have said, LPB has extremely anisotropic transport properties which support the idea of quasi-one dimensional conduction. Along such conducting axis,

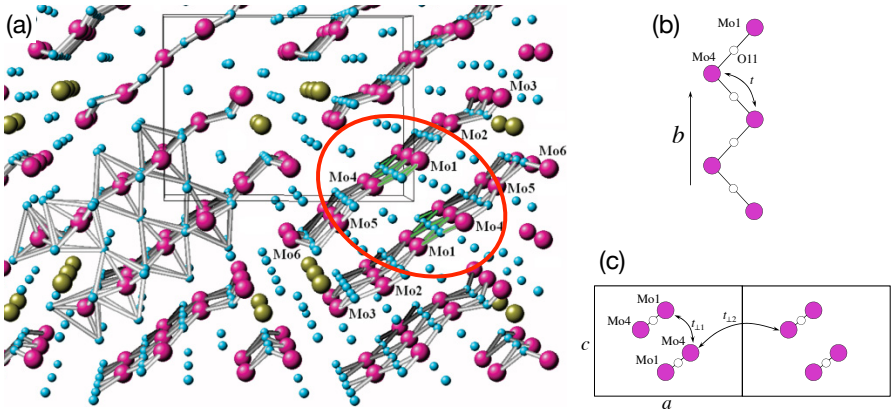

Figure 5.1 – (a) 3D layered crystal structure of LPB adapted from [92] where molybdenum is represented in magenta, oxygen in blue and lithium in yellow. The red circle indicates occurrences of the two quasi 1D chains (in green). (b) Zig-zag chains running along the conductor b axis. (c) Two adjacent unit cells projection into the insulating ac plane with zig-zag chains. Adapted from [93].

the resistivity shows an upturn at 25 K and eventually exhibits superconductivity below 2 K. While not unanimously embraced, a charge density wave (CDW) scenario has from the early studies been proposed as the explanation of the resistivity upturn [83]. Transport under high pressure showed a stabilization of superconductivity at the expense of the CDW-attributed resistivity upturn [87]. As the application of pressure generally tends to enhance the orbital overlaps in a low-dimensional solid, other ground states might be favored [88]. On the theoretical point of view, a crossover from a Luttinger liquid behavior to a to 2D metallic behavior could be considered [89, 90] for 1D conducting chains with the introduction of a small coupling. Reports of such crossover are claimed by thermal expansion experiments [91].

Clearly, more input is desirable regarding the underlying physics of this material and since CDW and SDW instabilities are usually well seen in optics and have shown to be strongly affected by pressure, a high pressure infrared spectroscopic study on LPB is therefore motivated.

5.1 A one dimensional material

$Li_{0.9}Mo_6O_{17}$ has a complex layered structure as shown in Fig. 5.1(a). With more than 23 atoms per formula unit, its crystal structure is the monoclinic $P2_1/m$ with lattice parameters $a = 12.7622$ Å, $b = 5.5231$ Å, $c = 9.4991$ Å and a near right-angle of $\beta = 90.61°$ [84]. A pair of octahedra individually formed of one molybdenum atom surrounded by six oxygen atoms forms two quasi-1D well separated zig-zag

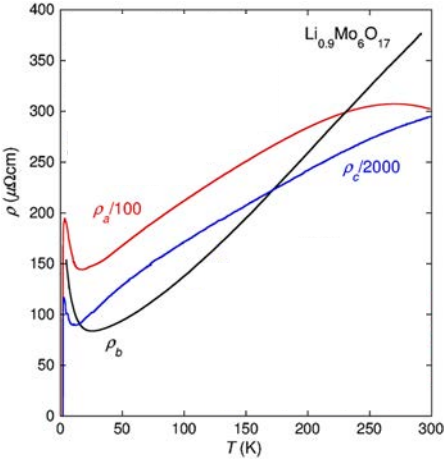

Figure 5.2 – Resistivity for all 3 crystallographic axis of LPB adapted from [94]

chains running along the b axis as shown in Fig. 5.1(b) and (c) . The most interesting feature of lithium purple bronzes is probably the high anisotropy of their electronic properties. Transport measurements [94] as displayed in Fig. 5.2 show three orders of magnitude of difference between b and c axis. Of particular interest is the presence of a sharp rise at 25 K in the resistivity of the b-axis. Above 25 K the b axis resistivity displays a metallic behavior and the sharp upturn below that temperature is eventually terminated by a superconducting transition below 2 K.

This high transport anisotropy suggests that the conduction mostly occurs within the MoO_6 octahedra zig-zag chains and that the coupling $t_\perp$ shown in Fig. 5.1(b) between them is very weak. This system is therefore a very interesting experimental playground to investigate the occurrence of strongly correlated one dimensional physics, i.e. Tomonaga Luttinger Liquid (TLL) [95, 96]. This kind of physics is strongly different from the one occurring at higher dimensions, for instance Fermi liquid. In such a 1D case, for an electron located on a chain the only scattering option is to move either left or right. However, the scattering of one individual electron is rendered impossible by the presence of neighboring electrons along the chain, thus forbidding any simple transposition of a free electron model into a one dimensional system [95] and indicates important correlation effects. Instead of such one-particle excitations, the system allows collective excitations of a special kind where the electron effectively divides itself into a charge and a spin excitation. For example, we consider an antiferromagnetic 1D chain at half filling as sketched in Fig. 5.3, i.e. constant charge density and oscillating spin density. If a vacancy (hole) was to be created by the photo-emission of an electron, both charge and spin densities are disrupted at the hole site. If the hole moves along the chain, one sees that, with

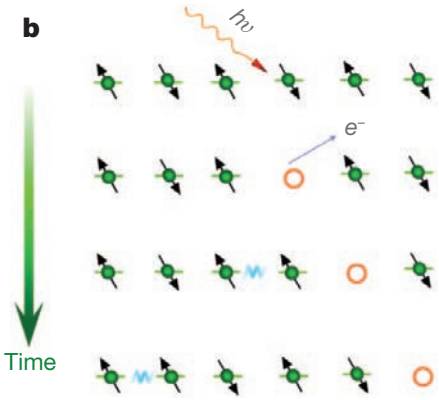

Figure 5.3 – Spin and charge separation on a AFM 1D chain, from [97].

respect to the initial configuration, the disruption in the charge and spin densities now occur on different sites which implies that charge and spin excitation are no longer tied to the electron. The charge excitation, the holon, carries a charge e (and no spin) and the spin excitation, the spinon, carries a spin $1/2$ (and no charge). The implication of this separation for spectroscopic techniques such as ARPES, usually yielding a single peak in the spectral function corresponding to the quasiparticle (the hole), is the observation of two distinct branches in the spectral function as shown in Fig. 5.4(a). For example, Fig. 5.4(b) displays ARPES data in the one dimensional $SrCuO_2$ [98, 99] which spectacularly revealed the dispersion of two peaks corresponding of the Spinon and Holon (each with its own velocity v_s and v_h). In addition to this spin-charge separation, TLL has two other implications regarding the spectral function: its angle-integration should approach the Fermi energy as a power law [100–102] with exponent α and it should also obey a scaling law [103, 104] for the temperature with exponent $\eta = \alpha - 1$. Similarly, optical spectroscopy performed on the metallic 1D organic conductors $(TMTSF)_2X$, where X=PF_6, AsF_6 and ClO_4 revealed [86] that the optical conductivity also exhibits power-law behavior with frequency.

In the case of LPB, electronic band structure calculations [105, 106] shown in Fig. 5.5(a) indicate that two very steep and almost degenerate d bands are crossing the Fermi level between the Y and Γ point, thus yielding an almost flat two-fold Fermi surface with important nesting (thus rendering likely a Peierls instability) and a slight warping due to the interchain coupling $t_\perp$ (shown in Fig. 5.1(b)). Such a Fermi surface was confirmed by ARPES measurements [107–109], as shown in Fig. 5.5(b) and (c) however without sign of warping. In contrast to $SrCuO_2$, the observation of the holon and spinon is not as obvious and the temperature scaling closer to T^α rather than T^η. The less quantitative agreement with theory is attributed to deviations from the ideal 1D TL since, in particular, the system is not exactly one dimensional

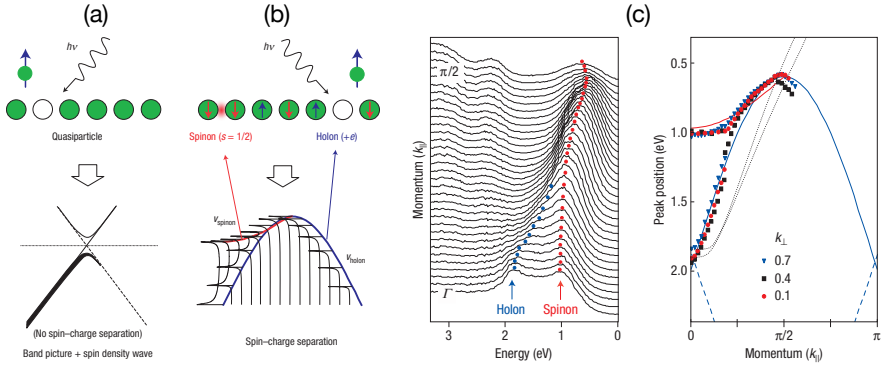

Figure 5.4 – Schematic difference between (a) quasiparticle excitation of a Fermi Liquid and a (b) TLL with spin-charge separation seen in spectral function. (b) ARPES data on $SrCuO_2$ indicating the holon and spinon dispersion. From [99].

(quasi-1D nature of the zig-zag chains, which are weakly coupled) and the Fermi level is crossed by two bands instead of one.

5.1.1 The 25 K upturn controversy

The mechanism behind the resistivity upturn appearing at 25 K in the b axis resistivity is subject to a controversy as several scenarios are proposed and are incompatible with each other.

One scenario is the opening of an energy gap upon cooling. This would be induced by a distortion of the crystal structure, and since here the conduction occurs along the b axis, it amounts to a distortion of a lattice whose nature is captured by the quasi one dimensional chains of Mo-O. For illustration, we consider, as sketched in Fig. 5.6, such a 1D metallic system (half filling) with sites periodically spaced by a constant a and its constant charge distribution $\rho_c(r)$. Grouping the electrons two by two results in a periodical variation of $\rho_c(r)$ named charge density wave (CDW) which is energetically favored and results in a gap opening at the boundary of the Brillouin zone turning the material insulator. Spin density wave (SDW) could also occur, as for instance in the case of an anti-ferromagnetic half filled 1D chain whose corresponding spin density $\rho_s(r)$ shows an oscillation of periodicity $2a$. As such Peierls instability is exhibited by other members of the family, for instance the blue bronze [110] which shows similar optical conductivity than LPB's b axis, such CDW instability was deemed very likely to also occur for LPB [83] in particular in view of its quasi 1D Fermi surface favoring nesting. Further support was found in ARPES data indicating a shift of the leading edge between room temperature and 17 K (below the upturn) and was interpreted as the signature of the opening of a

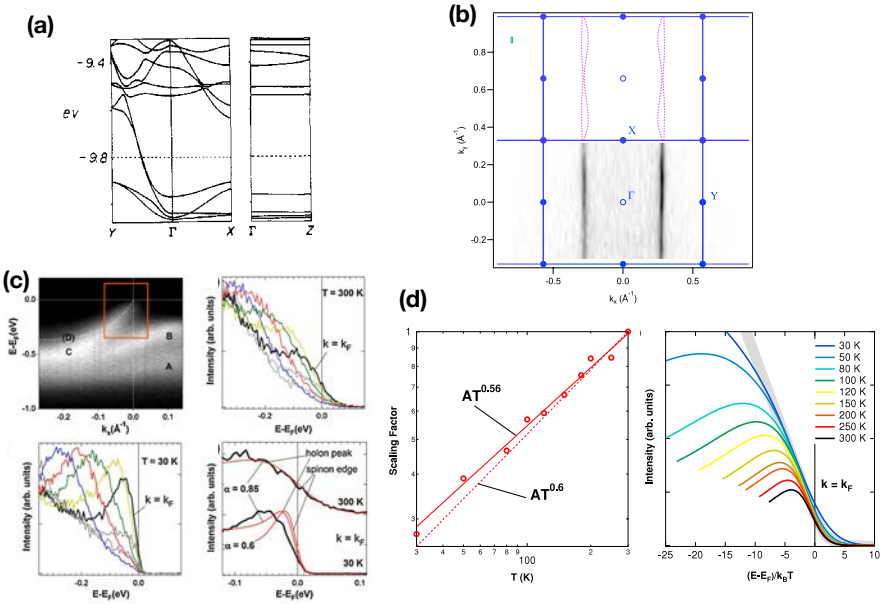

Figure 5.5 – (a) Band structure calculations from [105]. (b) Comparison between calculated (top) Fermi Surface compared to ARPES data (bottom) from [109]. (c) ARPES data showing a intensity plot of the spectral function and a comparison to a TL-like lineshape with charge-spin separation at k_F from [108]. (d) Power-law behavior of ARPES spectra from [108].

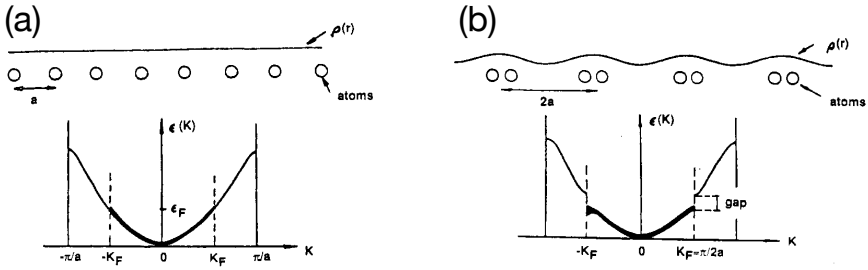

Figure 5.6 – (a) 1D chain with lattice constant a, constant density and (b) Distortion of the lattice by doubling its periodicity $2a$ resulting in a charge density wave turning the material insulating. Adapted from [81].

$\sim$40 meV gap [111].

On the other hand, another scenario excludes such mechanism. Optical studies in the infrared [112, 113] showed no sign of gap opening at low temperature. The latter [113] compared the distortion of the lattice seen in X-rays to the intensively studied material $CuGeO_3$, and its changes of the infrared spectrum as the temperatures cross the spin-Peierls 14 K transition temperature. The conclusion was that if any distortion were to exists it would only be very small (lattice constant changes of less than 0.001%) and eventually stands against any Peierls instability in LPB. Such conclusion is supported by a structural study by neutron diffraction [92] which indicates no sign of significant lattice distortion induced by temperature decrease. Based on that, the mechanisms of the 25 K upturn is instead attributed to localization [113] or to an increasing perpendicular coupling $t_\perp$ (shown in Fig.5.1(c)) between quasi one dimensional chains thus resulting into a dimensional crossover from a 1D regime occurring above the upturn to the 3D regime below 25 K where superconductivity appears below 2 K [90, 107, 109] .

5.1.2 Optical properties

Ambient pressure optical measurement in the infrared have already been the subject of several studies, among which the one by Choi *et al.* [113] done at several temperatures between 10 K and 300 K. The energy ranges from 6 meV to 5.6 eV for both the insulating axis $\perp$ b and conducting b axis. The orientation of the polarizers was determined so as to maximize the anisotropy of the optical response. The insulating axis showed in Fig. 5.7(a) contains a very dense set of sharp vibrational modes below 0.1 eV (as one could have expected which such a complex crystal structure) and a much simpler behavior at higher energy containing a few much broader excitations. The b axis in Fig. 5.7(b) shows a high reflectivity which nearly linearly decreases until

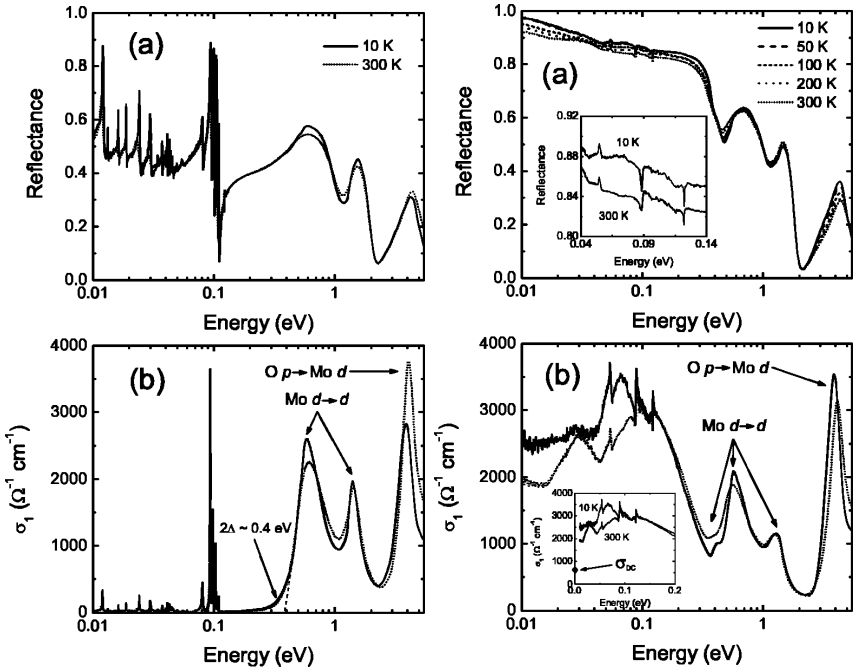

Figure 5.7 – Infrared optical study of LPB by Choi *et al.* [113]. Left panels show $R(\omega)$ and $\sigma_1(\omega)$ for the $\perp b$ insulating axis and the right panels show $R(\omega)$ and $\sigma_1(\omega)$ for the conducting b axis.

0.3 eV below which a few screened vibrational modes can still be distinguished. The reflectivity at low energy shows a slight increase when the temperature is lowered. The higher energy region shows a steeper decrease with frequency and the clear presence of broad excitation reminiscent of the ones observed in the insulating axis.

The optical conductivity was calculated by means of Kramers-Kronig transformation with extrapolation at high energy as ω^{-2} for both axis whereas at low energy a metallic response (Hagen-Ruben) is assumed for the b axis and an insulating (constant) one for the insulating $\perp$ b axis. The obtained conductivity shows an strong anisotropy which is even slightly higher than seen in the transport data.

On the insulating axis, an optical gap of 0.4 eV is observed along with several vibrational modes that blueshift as temperature decreases but exhibit no drastic changes below 25 K. Similarly, and for both axis in the high energy part, the broad peaks attributed to on-site excitations of the Molybdenum and a Oxygen-Molybdenum charge transfer excitation do not show any strong temperature dependance. The b axis contains no Drude-like contribution at any temperature which may be caused by low dimensionality and electron correlation. The inset of Fig. 5.7(d) shows a blow-up in the conductivity showing the location of the conductivity point obtained by transport which lies much below the optical curves. The insulating $\perp$ b axis is gapped up to $\sim$ 0.4 eV and features many sharp phonons at low frequency whereas the higher energy portion shows peaks which are associated with orbital excitations both Mo on-site and O-Mo. The b axis exhibits a rather conducting behavior with a high level of reflectivity at low energy and also features the orbital transitions seen in the other axis, but does not present a Drude peak (in contrast to the previous study [112]). Overall, the decrease of temperature affects more the b axis in the form of a slight increase of reflectivity. The mechanism suggested for the upturn is localization occurring whithin a TLL system.

5.1.3 High pressure transport

A previous pressure study in transport up to 2 GPa [87] showed a progressive suppression of the 25 K upturn up to 1.25 GPa in the b axis resistivity. This phenomenon was also accompanied by a slight increase of the superconducting critical temperature as displayed in Fig. 5.8. Such behavior was then attributed to the competition between a charge density wave responsible for the upturn and a superconducting instability.

5.2 High pressure optical study

Our optical high pressure study consists of infrared measurement performed in reflectivity geometry. Reflectivity measurements in at lower pressure in a range of $0.1 - 2$ GPa was planned using the previous pressure setup described in [7] as well as transmission measurements on thin samples were at first also considered but several technical issues were encountered on the Bruker 66/v spectrometer supporting

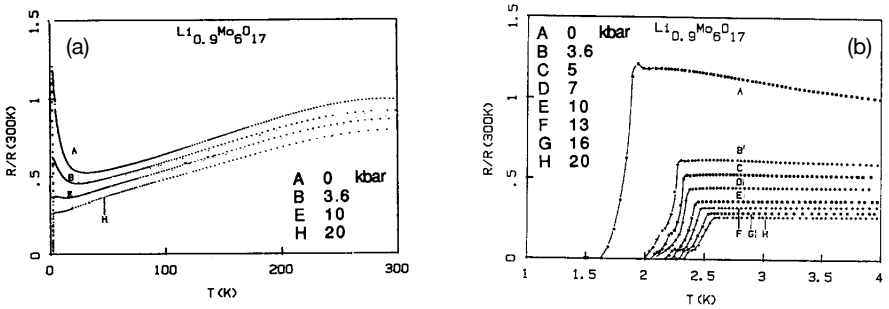

Figure 5.8 – (a) Ratios of resistance under pressure by ambient pressure resistance from [87].

both setups, thus preventing such measurements. Our infrared data are complemented by a high pressure Raman scattering study.

5.2.1 Infrared reflectivity

Before embarking on the high pressure experiment, *standard* optical measurements were carried out at ambient pressure. Samples similar to the one shown in Fig. 5.9(a) with surface's vector parallel to the c axis provided by M. Greenblatt were measured in Geneva on the available equipment at the time of the experiment. The MIR was covered by a Hyperion microscope where the normalisation consisted of the signal of a gold miror. An overlapping range was measured with a Bruker 70/v with a coldfinger equipped for gold *in-situ* evaporation to perform level normalisation. In both cases, a gold wire polarizer was used to distinguish both axis by maximizing the anisotropy. Reflectivity spectra shown in Fig. 5.9(b) are consistent to the optical measurements of Choi *et al.* [113] in the same energy range. However, due to to a lesser signal quality and spectral range, the aforementioned data will be used as reference in the discussion below.

Reflectivity data at high pressure was acquired on a Hyperion microscope at the X01DC beamline. A KBr window separates the Bruker 70v spectrometer of the Hyperion coupling optics and thus imposes a low energy cutoff of about 0.05 eV. Freshly cut samples were loaded in the DAC with rubi chips and KBr powder as a pressure transmitting medium. A gold wire polarizer working in FIR-MIR is placed at the rear of the reflective objective to separate the conducting and insulating axis optical response. Incidentaly this also limits the upper limit in spectral range to about 0.6 eV. Before each pressure run we first do a polarization check by measuring spectra every $\sim 13°$; one for the sample and one for the reference taken on the gasket. Since the angle setting is manual and showed an important backslash it was deemed more reliable to change the angle only once and move back and forth

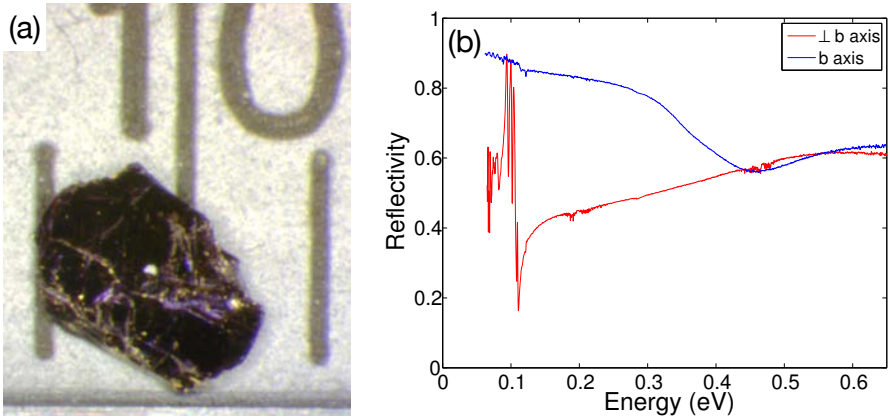

Figure 5.9 – (a) Crystal of LPB. Separation between graduation is one mm. (b) Infrared spectra of the reflectivity in both insulating and conducting axis at ambient pressure and room temperature.

the DAC thus switching between sample and gasket location. The ratios allowed to identify the polarizer angle corresponding best to insulating axis by trying to minimize the intensity minimum observed close to 0.1 eV. The angle corresponding to the conducting axis was determined by turning the polarizer of 90° further. However, the b axis turned out to be more difficult to determine as numerous experimental runs exhibit anomalous b axis reflectivity showing for instance partial contamination with strong phonons coming from the insulating axis. The situation did not improve on ratios for adjacent angles. In these case the b axis data are discarded.

At first, only room temperature measurements were performed. Then with the availability of the cryostat reflectivity measurements at 13 K were performed. Since the pressure is not tuned at low temperature, it implies to make a full thermal cycle before changing the pressure inside the DAC – which also showed noticeable changes during the cycle[1]. Such experiments turned out to be quite lengthy (in particular due to the temperature sweep) which renders it intrinsically non-optimized for synchrotron beamtime experiment with time constrains. For these reasons the pressure and temperature mesh of our data is not ideally densely filled for both axis. One notes that since many pressure runs were attempted under many different conditions/constraints of measurement (time, microscope alignment/coupling, windows, and detectors), that the various datasets gathered are not easily combined and merged. Instead, we separately present the results obtained on distinct pressure runs.

[1]These unwanted, repetitively occurring and non negligible temperature-induced changes of pressure, attributed to the membrane, actually remained un-explained by the DAC manufacturer (BETSA).

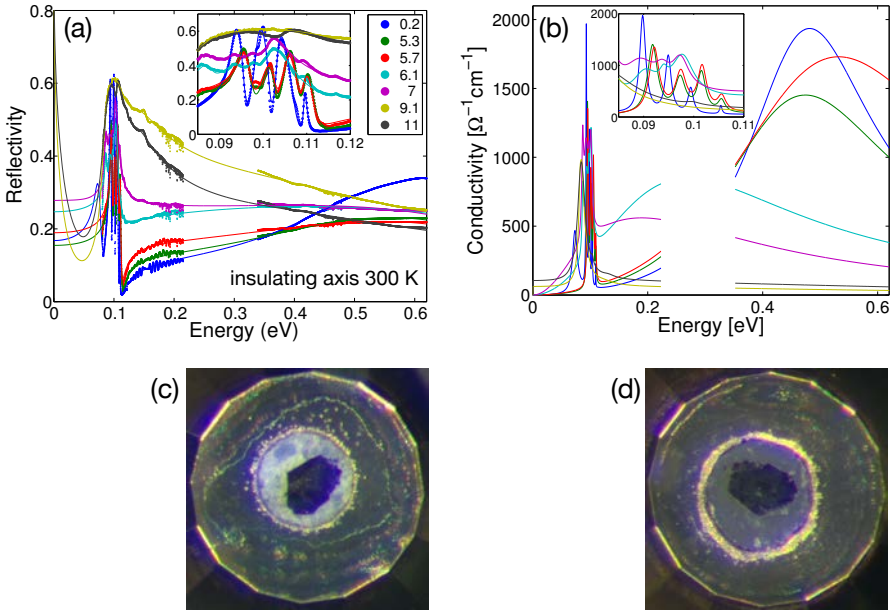

Figure 5.10 – Insulating axis at room temperature. (a) Reflectivity data (dotted) fitted with DL model (lines), inset magnifies the phonon region. (b) Optical conductivity at several pressures. (c) Photograph of the sample after the loading the DAC, before compression with KBr powder as pressure transmuting medium and (d) after decompression.

Room temperature Fig. 5.10(a) shows the reflectivity of the insulating axis at ambient temperature for several selected pressures obtained with a MCT detector. The curves indicate a clear and fast metallization upon pressure increase near 5.7 GPa, a pressure below which the phononic structure below 0.12 eV remains recognizable as shown in the inset. Just above 6 GPa, the reflectivity experiences a drastic increase which starts to screen the phonons. Above 9 GPa, the reflectivity reaches its maximum and no sharp phonons is observed. At 11 GPa, the reflectivity decreases again above 0.12 eV. The data was phenomenologically fitted with a Drude-Lorentz model in order to extract the optical conductivity shown in Fig. 5.10(b). Sample loaded in the DAC is shown in Fig. 5.10(c) right before the start of the pressure run and Fig. 5.10(c) shows the same sample after the release of the membrane pressure.

Another pressure run shown in Fig. 5.11 was specifically focused on the evolution of the phonons and was conducted with a MIR bolometer detector covering the lowest accessible spectral range. Unfortunately, this pressure run did only allow to cover a smaller pressure range since it only got to 5.7 GPa. However one stresses the consistency with the previous run for the insulating axis: upon pressure increase we clearly see the progressive screening of the phonon which is accompanied for some

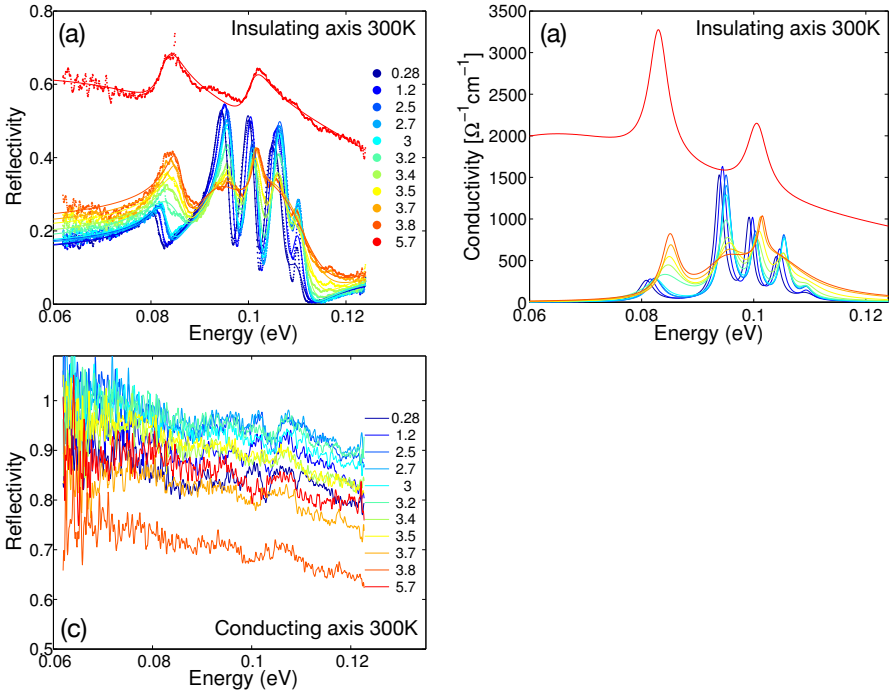

Figure 5.11 – Ambient temperature and low energy reflectivity of LPB under high pressures (in GPa). (a) Insulating axis reflectivity and (b) optical conductivity Drude-Lorentz fitting. (c) Reflectivity of the conducting axis.

of them with a noticeable blueshift and possible splitting near 3.5 GPa.

During the same pressure run, we were also able to measure the reflectivity of the conducting axis, which displays no strong spectral features as previously reported. The effect of the pressure does however not induce significant spectral changes. Of particular importance is an observed increase of the general level of the reflectivity up to 3 GPa. Above this pressure the reflectivity starts to decrease again and eventually reaches a level even lower than at the start of the pressure run.

Low temperature As mentioned earlier in the case of low temperature measurements the modification of the pressure inside the DAC is done at room temperature only. Hence, we also measured the reflectivity at 300 K. It also turned out that both the insulating and conducting axis were observable during a particular experiment using a MCT detector. The results at ambient temperature and 15 K, i.e. below the 25 K resistivity upturn controversy, for the insulating axis are displayed in Fig. 5.12(a) and (c). The insets magnify the phonon region. The results on the conducting axis

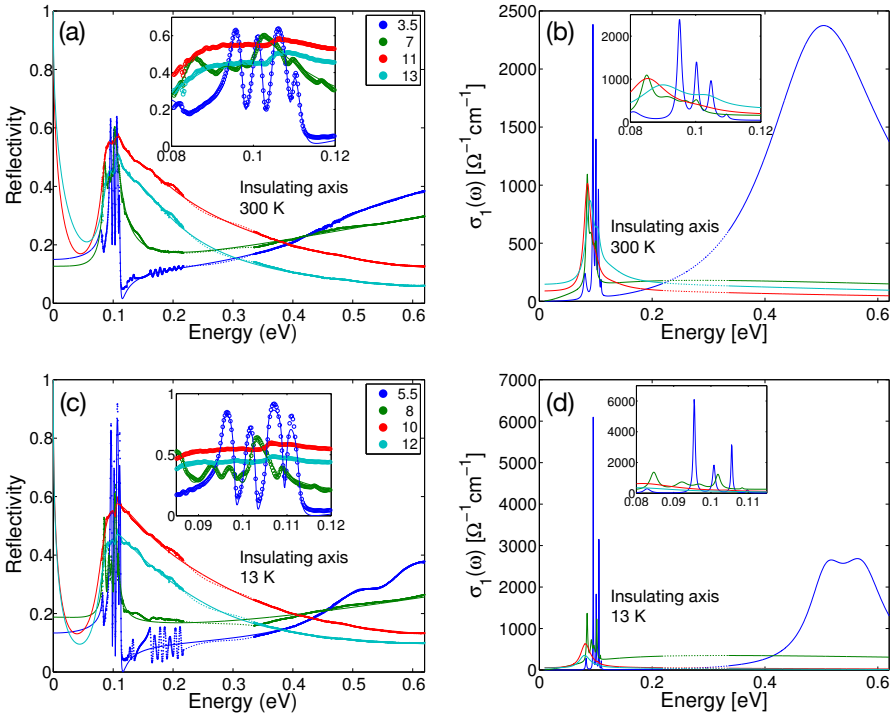

Figure 5.12 – Insulating $\perp$ b axis with (a) $R(\omega)$ at 300 K with Drude-Lorentz fit at several pressures (in GPa), (b) the corresponding optical conductivity. (c) $R(\omega)$ at 13 K and (d) corresponding $\sigma_1(\omega)$.The dashed region correspond to the diamond absorption.

are shown in Fig. 5.13(a) and (c). As previously reported, the temperature effect on the reflectivity on the insulating axis does not induce drastic changes: we however report a general increase of the level of reflectivity for the insulating axis. We stress that the lowest pressures of this experiment are already significant: 3.5 GPa at 300 K and 5.5 GPa at 15 K and make the comparison with ambient pressure data difficult.

5.2.2 Raman Spectroscopy

Raman shift was measured at room temperature as a function of pressure in the same pressure cell and using Daphnee oil 7373 as a pressure medium. The results obtained with unpolarized light are shown in Fig. 5.14(a) as raw renormalized data curve with a vertical spacing scaled with pressure and also in a intensity plot shown in panel (b) as function of shift and pressure.

The spectrum is extremely rich, and therefore has not been modeled in order to look after changes on the Raman mode parameters induced by pressure. Instead, one

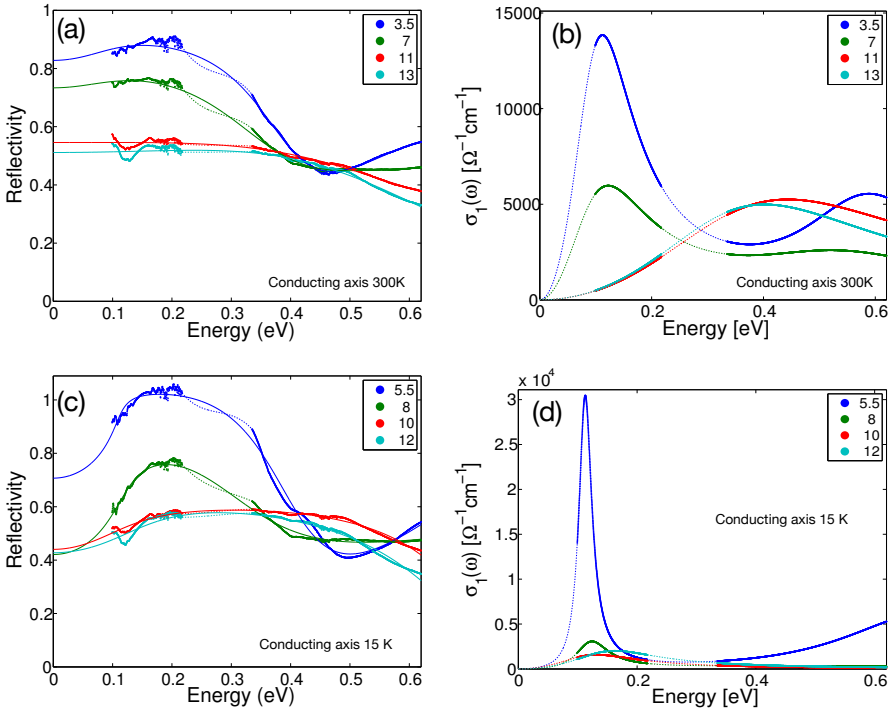

Figure 5.13 – Conducting b axis with (a) $R(\omega)$ at 300 K with Drude-Lorentz fit at several pressures (in GPa), (b) the corresponding optical conductivity. (c) $R(\omega)$ at 15 K and (d) corresponding $\sigma_1(\omega)$.The dashed region correspond to region out of experimental range or to the diamond absorption.

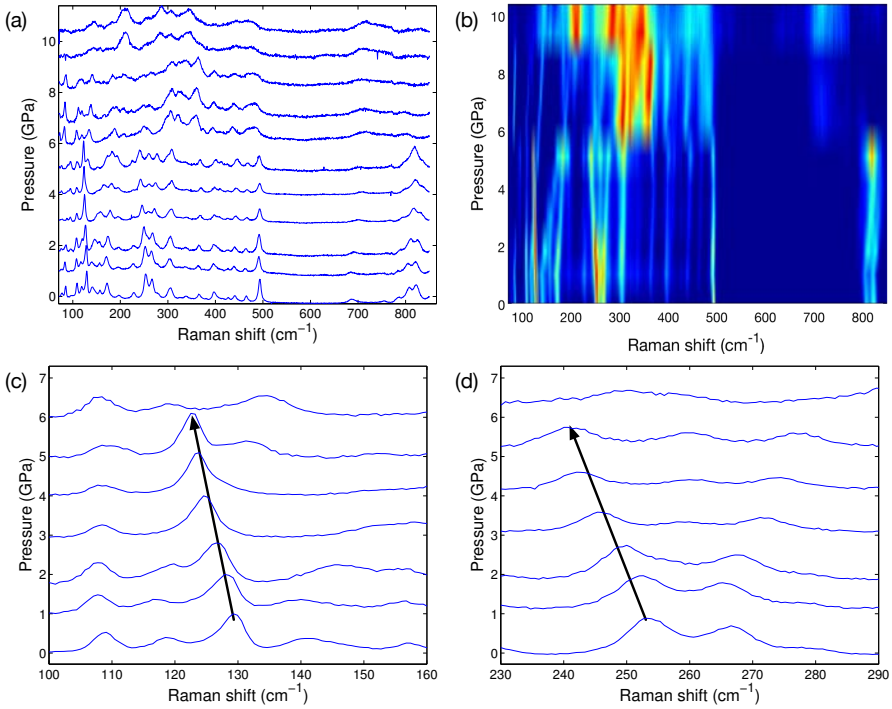

Figure 5.14 – Raman shift of LPB under pressure. (a) Normalized curves shifted according to their pressure. (b) Normalized intensity plot as a function of Raman shift and pressure. (c) and (d) show two modes that redshift with pressure and disappears above 5 GPa.

might more easily sees such evolution on the intensity plot which allowed to highlight an abrupt change occurring at about 5 GPa. Looking in more details at the the lower pressure region, one can notice that at least two Raman mode redshift with pressure. One lies at 130 cm^{-1} at ambient pressure and monotonically shifts to 122 cm^{-1} at about 5 GPa where is vanishes, as displayed in Fig. 5.14(c). The same happens for another mode initially at 253 cm^{-1} that redshifts to 241 cm^{-1} as indicated in Fig. 5.14(d)

We then performed an additional pressure run using polarized light and also over a broader spectral range. This required the rotation of the grating between low and high energy region. The rotation is reproducible but introduces a slight shift in intensity and frequency ($\sim$ 1 cm^{-1}). Therefore, we take the low energy region as reference and the higher energy region is shifted back in energy and the level is scaled so as to match the low energy data. The curves Raman shift for XX and XY polarization are shown in Fig. 5.15 (a) and (b) and are vertically shifted to the pressure scale. Again,

the two spectra displayed are very rich and unpraticable to model. They nevertheless exhibit major change above 4 GPa, at least in the XX geometry where new modes seems to appear below 400 cm^{-1} and near 500 cm^{-1}.The XY geometry displays a simplified single mode near 850 cm^{-1} above this pressure. A color intensity plot in both Raman shift and pressure are shown in Fig. 5.15(c-d) which seems to indicate even more discontinuities in the mode's positions as the pressure increases. The two redshirting modes observed in the unpolarized experiment are also seen but in different polarization as highlighted in Fig. 5.15(e-f). The mode at 130 cm^{-1} belongs to the XY polarization and is found to redshifts from 129 cm^{-1} to 125 cm^{-1} at 4 GPa above which it vanishes. The mode at 253 cm^{-1} is found in the XX polarization where it moves from 252 cm^{-1} to 244 cm^{-1} also up to 4 GPa.

5.3 Discussion

As mentioned earlier, since the experimental data are available on a more narrow energy range and with less accuracy (determination of the polarizer's angle, renormalisation) as in the case of the previous study of BiTeI, we do not expect here to extract a quantitative optical conductivity from $R_{sd}(\omega, P)$ and rather more aim to identify the qualitative influence of pressure. The analysis of the reflectivity at sample-diamond interface R_{sd}, has been attempted on the data set of the insulating axis at room temperature as presented in Fig. 5.10(a) using a Drude-Lorentz modeling of the dielectric function. The resulting optical conductivity is displayed for the same curves in Fig. 5.10(b) with the inset magnifying the phonon region. Following previous studies at ambient pressure indicating the absence of Drude response at low energy our phenomenological dielectric function at the lowest pressure only contains Lorentzian oscillators: one for each strong phonon in low energy region and one for the broad excitation dome at higher energy. The agreement is rather good in the reflectivity and the obtained conductivity is qualitatively consistent with the one of previous studies (and quantitavely off by about a factor of two). The reported optical gap of 0.4 eV, could be pictured disregarding the low energy tail of the higher energy lorentzian. One also notes the presence at low pressure of oscillations between the phonon region and the lower diamond absorption range that we interpret as Fabry-Perrot oscillation of the sample cavity and therefore support an insulating behavior. These oscillations persist in the spectrum until the 6.1 GPa curve (which features in this region some noise attributed to absorption in air, also already present in all other spectra).

The DL analysis carried out displayed three major effects. First, the phonon spectrum is cleared when passing above 9 GPa, as already seen in reflectivity. Second, the redshift and suppression of the higher energy oscillators at 9 GPa, thus giving the impression of an pressure-induce optical gap closure. Third, the drastic increase of reflectivity in the lower part of the spectrum in the absence of sharp spectroscopic features forces the energy of lorentzian oscillators to zero. The appearance at the same pressure of such a Drude peak and the disappearance of the energy gap build a

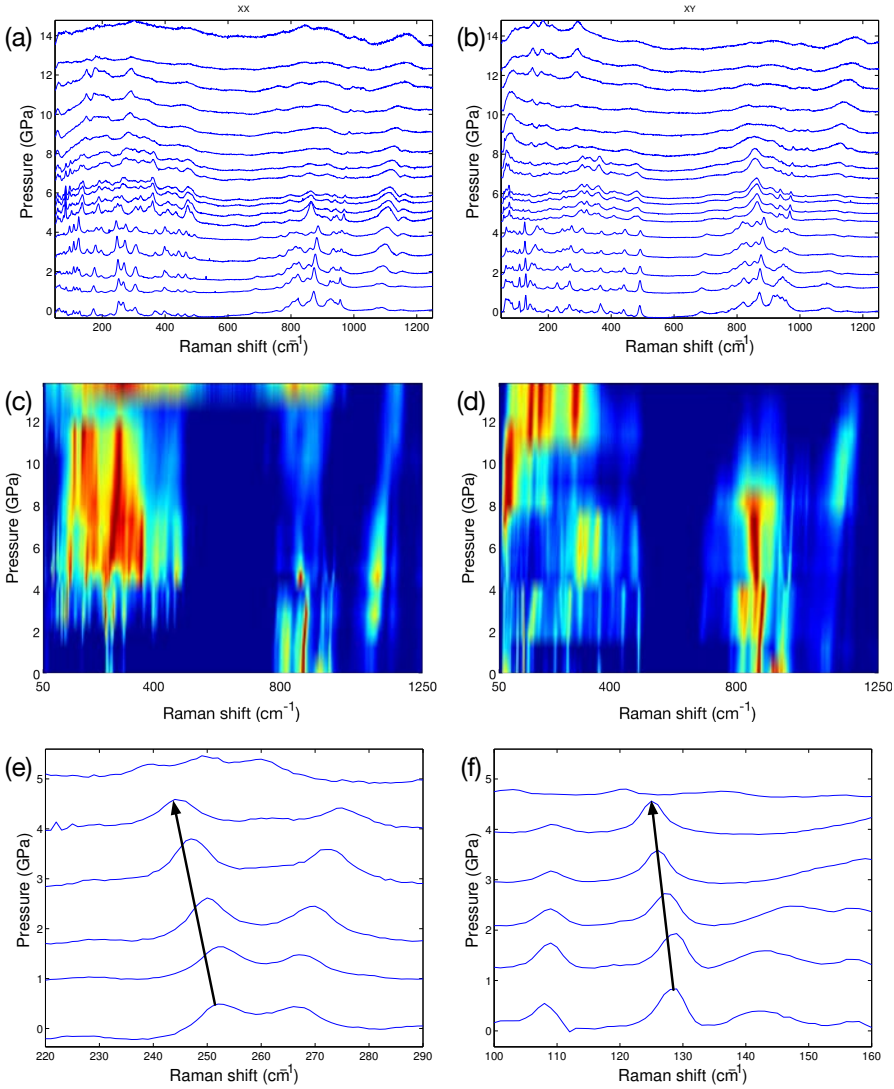

Figure 5.15 – Raman shift in XX (a) and XY (b) polarizations with curves vertically shifted with respect with pressure.(c) and (d) show the corresponding intensity plot as a function of Raman shift and pressure. (e) and (f) show magnified regions of the XX and XY polarizations respectively, where one mode redshifts.

case for the metallization of the (previously) insulating axis.

The conductivity extracted from the second room temperature pressure run for both axis allows first to refine the pressure phonon dependence which displays a splitting of the main phonon peak occurring at 3.5 GPa. The increase of the lowest energy part is consistent with the observation of the metallization observed in Fig. 5.10. The conducting axis shows first an increase of the general conductivity level up to 3 GPa and eventually drops below its initial level.

The low temperature run shows room temperature data consistent with the two previous data sets at 300 K. However, the pressure range unfortunately does not overlap with the range of available data for the conducting axis since the lowest pressure lies at 3.5 GPa (thus precludes the observation of the b axis reflectivity increasing then decreasing). The insulating axis undergoes a metallization and displays a disappearance of phononic structure. The 15 K data shows a higher magnitude of reflectivity (hence higher conductivity) which is consistent with previous studies. The metallization sequence remains qualitatively identical with the distinction of a lower conductivity at low energies. One notes that the Mo transition metal $d-d$ transition producing a single excitation near 0.5 eV and present at 300 K has split into two close excitations. Qualitatively, as a decrease of anisotropy in the crystal field should reduce the splitting between energy level, one expects that the position in energy of this excitation redshifts, which it eventually does below 11-10 GPa. Above this pressure, the presence in both axis of this excitation is suppressed.

The b axis data was fitted with two lorentzian curves in the lower pressure range whereas only one was needed in the higher range. The peak at higher energy, also attributed to the $d-d$ transition which is suppressed at high pressure. In strong contrast to the insulating axis, the conductive one only exhibits a decrease of reflectivity leading also to a decrease of the conductivity.

Overall, the infrared data (already in the reflectivity) give the impression of a qualitative (strong) reduction of anisotropy at high pressure for both axis which tends to indicate that the system is driven away from a quasi 1D behavior.

The unpolarized Raman spectra is very dense but still allows to distinguish the evolution of some of the optical modes under pressure. The observation of the hardening of some optical modes under pressure is not unexpected. The presence of modes redshirting, and eventually, disappearing with pressure is a more peculiar thing and qualifying them as soft modes is very attractive since they would constitute the signature of an instability toward a different crystal structure. Such a scenario is compatible with the observation of the appearance and disappearance of a complex set of peaks under pressure which suggest the occurrence of several structural changes. The intensity plot shows several discontinuities occurring near 6 GPa, followed by another near 9 GPa. The polarized light dataset, and in particular in view of the intensity plot, also displays several lineshape discontinuities with pressure. Compared to the unpolarized experiment, the first discontinuity is observed above 4 GPa (mostly in XX geometry) and the second one closer to 8 GPa. An additional line shape is also

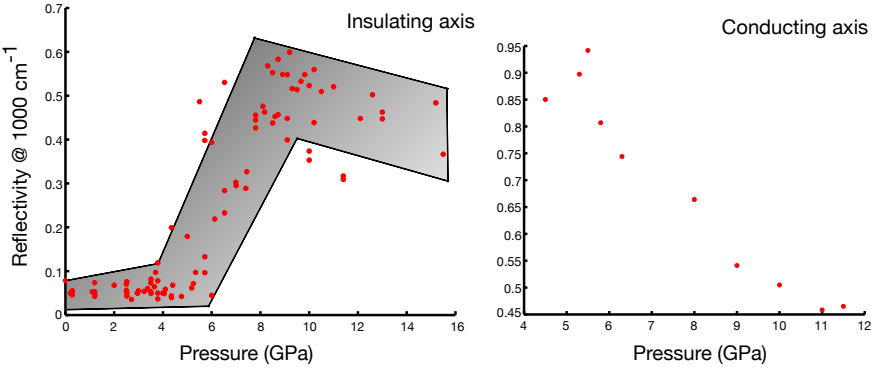

Figure 5.16 – Cuts of reflectivity at 1000 cm^{-1} for insulating (left) and conducting (right) axis.

seen in both geometries slighly below 12 Gpa.

The occurrence of these transitions could be supported by performing a cut in the reflectivity curves for both axis at fixed frequency of 1000 cm^{-1} over all our sets of data (this frequency is chosen for the absence of strong features in the spectrum) as shown in Fig. 5.16. One easily sees for the insulating axis the quick rise of the reflectivity above 4 GPa in a "step-like" way over about 1 GPa of broadness as sketched by hand with the gray area. In fact, for some runs this rise occurs at a higher pressure near 6 GPa but the broadness remains the same. This discrepancy might be explained by the fact that over 11 different pieces of sample and 11 different experiments spread over several months were needed without even considering the changes coming from differences of pressure distribution/determination. In the vicinity of $9 - 10$ GPa the trend abruptly changes and the level decreases again, thus suggesting another transition. The conducting axis tends to indicate first a small increase of the reflectivity followed by slow decrease. At high pressure the reflectivity reaches a level similar to the one of the insulating axis.

5.4 Conclusions

The optical response of the materiel shown to be dramatically influenced by the application of pressure. The reflectivity measurement highlighted a metallization of the otherwise insulating axis which was supported by the disappearance of the Fabry-Perrot oscillations and the setting-in of a Drude peak. This trend is observed both at room temperature and a 15 K, below the resistivity up-turn observed at 25 K at ambient pressure. This behavior is not so surprizing as pressure generally tends to increase the orbital overlap thus favoring the mobility as was observed on many

quasi 1D organic compounds. What is much more intriguing and counterintuitive is the decrease of the conductivity observed in the conducting axis. This apparent qualitative more isotropic response induced by pressure brings another evidence that the material is driven away from its initial quasi 1D dimensional conduction scenario.

The high pressure sensitivity of the Raman line-shape which suggests several successive structural phase transitions should constitute strong motivation for a detailed structural study under pressure which might give precious informations on the fate of the quasi 1D conduction channels, and of their relevance in the higher pressure phases.

CHAPTER 6

Conclusion

It's no wonder that truth is stranger than fiction. Fiction has to make sense.
Mark Twain

A substantial amount of time was dedicated during this work to the experimental setup(s) required to conduct high pressure optical spectroscopy experiments at low temperature. It was conceived using commercially available components and also from custom-designed ones that were assembled into two distinct configurations: transmission and reflexion geometries. The first was meant to be coupled to an Bruker 66/v vacuum chamber and the second can be mounted on a Hyperion microscope coupled to a Vertev 70v. Both spectrometer and microscope are available at the X01DC beamline of SLS and in Geneva, thus constituting two (almost) plug-and-play setups. The reflectivity setup can also be put on the Raman microscope based in Geneva.

Due to the sample's extreme environment and to its own size, the quality of the acquired data is not comparable to the quality of ambient pressure optical data which renders its analysis challenging on a quantitative point of view. Despite this issue, we tried via some simplifications to apply a standard Drude-Lorentz and also Kramers-Kronig analysis technique to the reflectivity which yields conductivity curves easily comparable to the one obtained at ambient pressure.

The first material investigated and presented in this work is BiTeI, a material whose properties were predicted to be strongly pressure dependent and even feature a topological transition thus provoking a resurgence of interest. One necessary condition required for the occurrence of this new state is the energy gap closure at a critical pressure immediately followed by an inverted energy gap re-opening. Being a

bulk property, such gap was easily followed under pressure, either by transmission or reflexion, and displayed only a monotonic decrease, i.e. no re-opening. As optical data indicated profound changes at 9 GPa, a phase transition was suspected to occurs which was confirmed to be a structural one by means of Raman spectroscopy. GW band structure calculations taking into account quasi-particle corrections, actually indicated that the predicted topological phase transition might occurs at a pressure of about 10 GPa, which means that the structural phase transition occurs before. In accordance with the fact that our optical data shown no sign of an insulating behavior above such pressure, a candidate for a compatible high pressure phase crystal structure was proposed as $P6_3mc$ which is metallic under pressure. As times elapses, more results of other high pressures studies on this compounds have been released from which a majority present results in perspective of the topological transition. Theoretical studies containing *ab initio* calculation are all based on DFT-GGA, which is known to underestimate energy-gap and incidentally the value of the critical pressure, but do however show critical pressure of increasing value. XRD experiments associate the minimum in the c/a ratio observed at 2.2 GPa for some and 4.5 GPa for others as the signature of the topological transition. Experimental consensus is unanimously reached regarding the occurrence of a structural phase transition at 9 GPa. The high pressure structure can not be determined solely from measured XRD pattern which are used as compatibility-check for proposed structures energetically favored. Finally, quantum oscillations results (although clearly in a lower pressure range) suggest that the lowering of the conduction band occurs more slowly with pressure than predicted, which might be in accordance with our conclusion.

Being around for more than 30 years, Lithium Molybdenum purple bronze have been already intensively studied with many techniques, in particular since they offered a simpler playground for the investigation of low dimensional physics compared to the organics superconductor that were extensively studied before them. Our experimental results in the infrared indicate than the application of pressure induces a metallization of the insulating axis $\perp b$, which is a phenomena theoretically well understood. Which is more surprising is that the pressure also induces a reduction of the conductivity along the b axis. Above $10-11$ GPa, the optical response has lost most of its ambient pressure anisotropy thus suggesting that the material is driven away from its 1D behavior toward higher dimensions.

Raman measurements under pressure indicated several discontinuities which led us to consider the occurrence of successive structural phase transition which might be at the origin of such pressure-induced (more) isotropic optical response. However, the absence of structural study under high pressure makes the identification of the underling physics causing this dimensional change uneasy.

APPENDIX A

LabView Program: ElisaBETSA

I like the challenge of trying different things and wondering whether it's going to work or whether I'm going to fall flat on my face.
Johnny Depp

The pressure equipment brought with the DAC also contained the BETSA software controlling their pressure determination suite based on a grating-bases spectrometer. Having encountered multiple difficulties, in particular the obvious obsolescence of the unstable PRL software only working on legacy version of Windows 3.11, and also, the required dedicated tower-form factor computer with legacy ISA motherboard extension connector hosting the interface to the spectrometer external electronics box. It was soon realized that while being frequently moving the hole high pressure setup itself from Geneva to the Swiss Light Source, moving along such bulky and unreliable solution of pressure determination was not a good solution. Hence some time was invested to put together an as much as possible automated workflow to perform the pressure determination based on modern, compact and reliable hardware. Thanks are owed to JL, in particular for finding a name to the program.

A.1 Basic calculation

The LabView interface is based on a commercial example provided by Ocean Optics covering the spectral acquisition in loop with the HR+2000 spectrometer. It also embeds commercial examples provided by Lakeshore allowing temperature capture.

After each integration (of adjustable duration), the spectrum is re-sampled into a smaller spectral region containing the two rubi fluorescence lines and displayed on a graph. When *Fit* is on, the spectrum is then fitted to a model of two gaussian peaks and a constant background and the result displayed on a graph along the raw spectrum. The parameters are also shown. It is necessary to provide some initial value to the parameters to ease the fit convergence.

The wavelength of the two gaussian are always ordered, thus preventing accidentally mixing the two while fitting resulting in an incorrect pressure determination. The resulting parameters can be use as the new starting parameters for the fit of the subsequent spectrum by turning *D/MFT*[1] on. This allows a much faster fitting time and for a rather usual integration time in of 0.1 second range, and give an almost real-time fitting which is extremely useful when performing alignment. This feedback was initially intended to allow the adaptation of the starting parameter as pressure markedly shifts the position of the peak away of their ambient-pressure values thus frequently resulting in a completely irrelevant fit. For the very same reason, one should not let this feedback active if one is about to externally cause a significant spectral change (obturation, or displacement of laser beam, and so on) which might cause a permanent divergence of the fit requiring to manually enters valid starting parameter. The temperature can be read on a controller for instance here a Lakeshore.

One notes that instead of benefiting of the automatism provided by ElisaBETSA, the software can very well be used to calculate a pressure while manually entering both temperature and wavelength of R_1 peak and by choosing the method of calculation (hydrostatic of quasi-hydrostatic). The temperature correction to the shift in wavelength is automatically carried out when *Measure T* is on.

The references values of wavelength and temperature can be set by the software: results of fits can be designated to be used as the reference by clicking while fitting on the *Take lambda ref* button whereas *Take T ref* button sets the current temperature as the reference. If needed, the starting parameter of ambient condition can be restored as starting parameters by selecting *RTAV*.

Globally, when the program is running and fluoresce light is reasonably well detected, thanks to the large digital dial, one can easily follow the evolution of pressure with some distance of the computer which is much appreciated when having to move around within the lab/beamline during the experiment.

A.2 Data saving

If one is interested in automatically keeping trace of the evolution of the pressure run, one might find it useful to keep track of the evolution of fluorescence and other informations. Here, at the same time as the software is fitting, one can clic to *Save ALL* button which will save in three different text files (a) the raw measured

[1] Stands for Dynamical Mean Fit Transfert.

spectrum, (b) the fitted two gaussian line shape and (c) the fit parameters and other useful information one has manually entered such as: pressure inside the DAC's membrane, temperature. In any case, the files created contains by default in their name the membrane pressure, the temperature and the DAC pressure. Additionally, a customized string of character can also be added to the name. Files are stored in a user-define file path. One notes that the *Log* function is not operational in the current state.

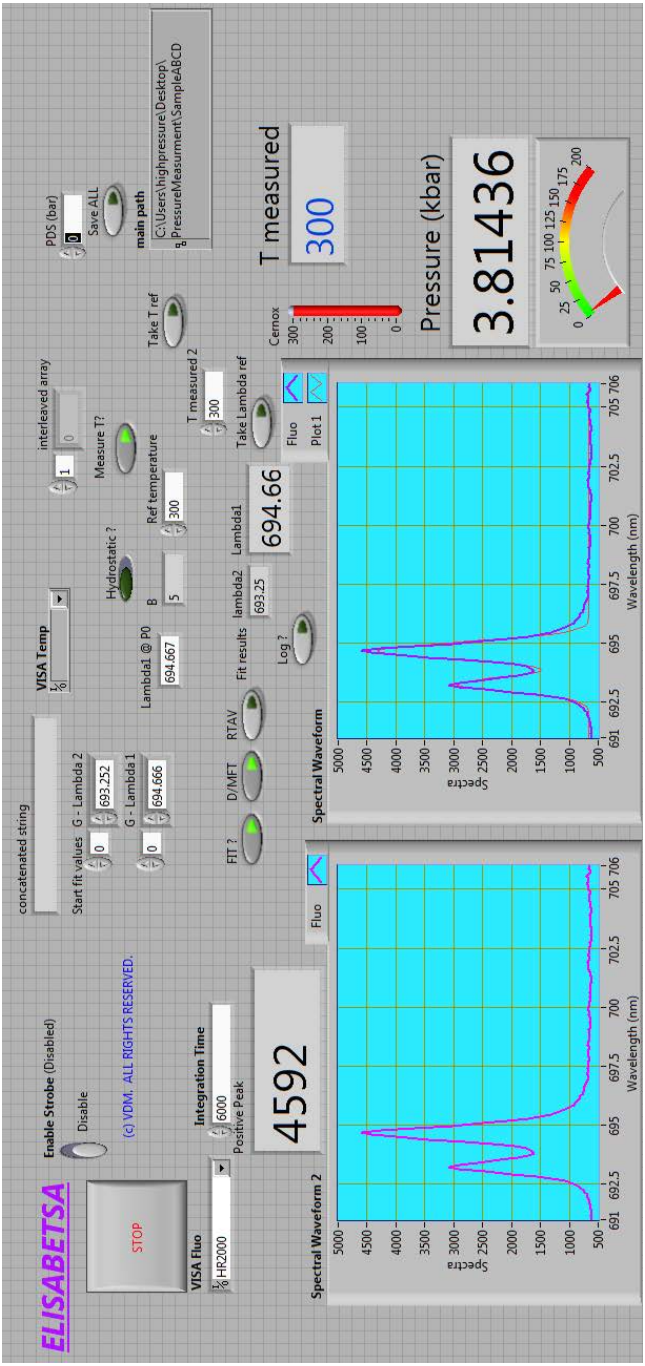

Figure A.1 – Front view of the labview program ElisaBETSA.

APPENDIX B

Technical Drawings

If you want to make God laugh, tell him about your plans.
Woody Allen

The two setup presented in chapter 3 of this Ph D work required several customized mechanical pieces that were conceived with the Inventor software suite. Finished pieces were delivered by the Atelier de méchanique de la section de physique, based on the technical drawing presented in the present appendix (scales contained in the drawings are misleading due to their inclusion). Unless specified, all units of length are in millimeters. Drawing for pieces of the transmission setup are those contained in [21] and have been slightly modified while the manufacturing process that occurs during this work (updated drawings corresponding to the final design shown in Fig. 3.10 are pending and will be available as a separate document). Drawings of the newer reflectivity setup are presented in the following pages.

B.1 Reflectivity

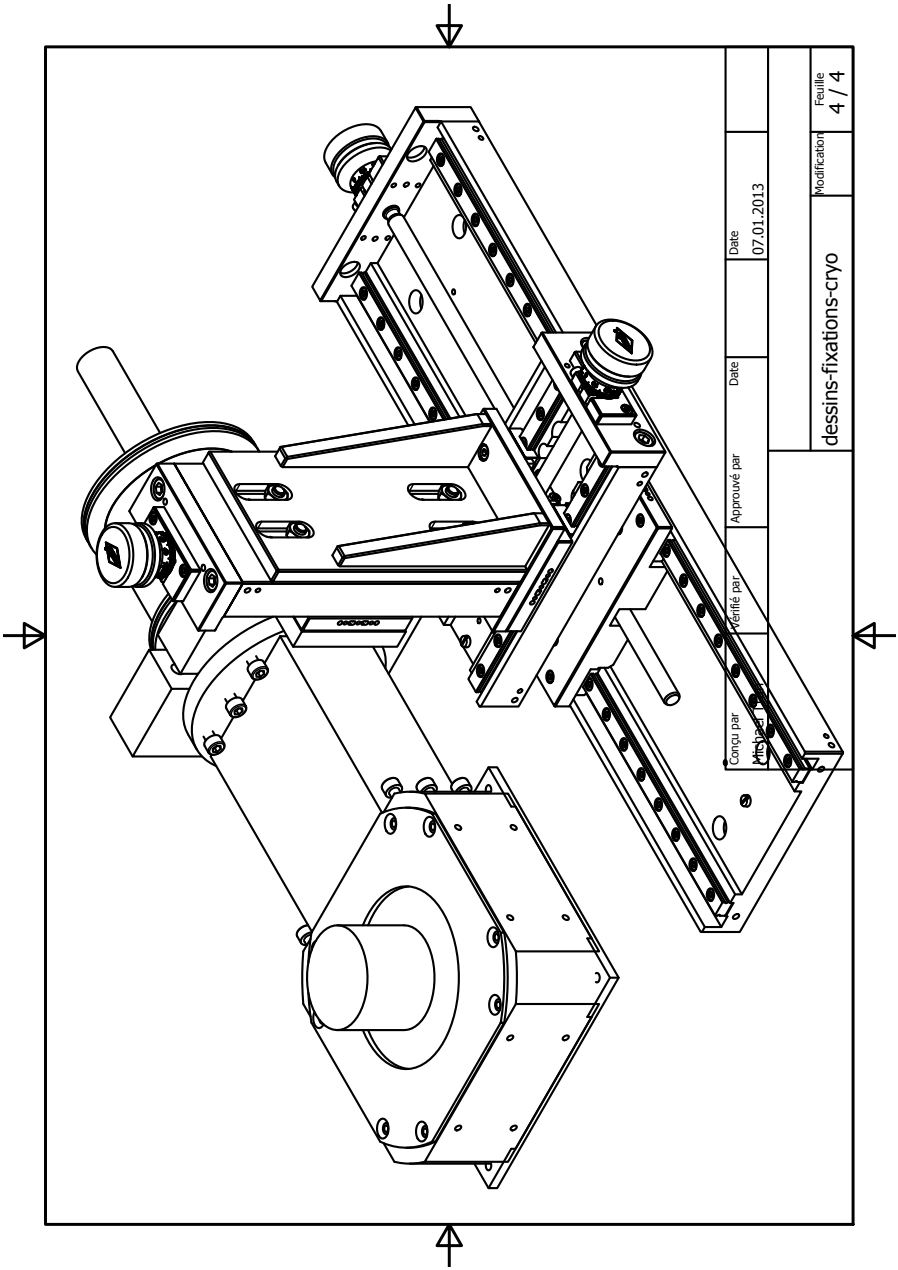

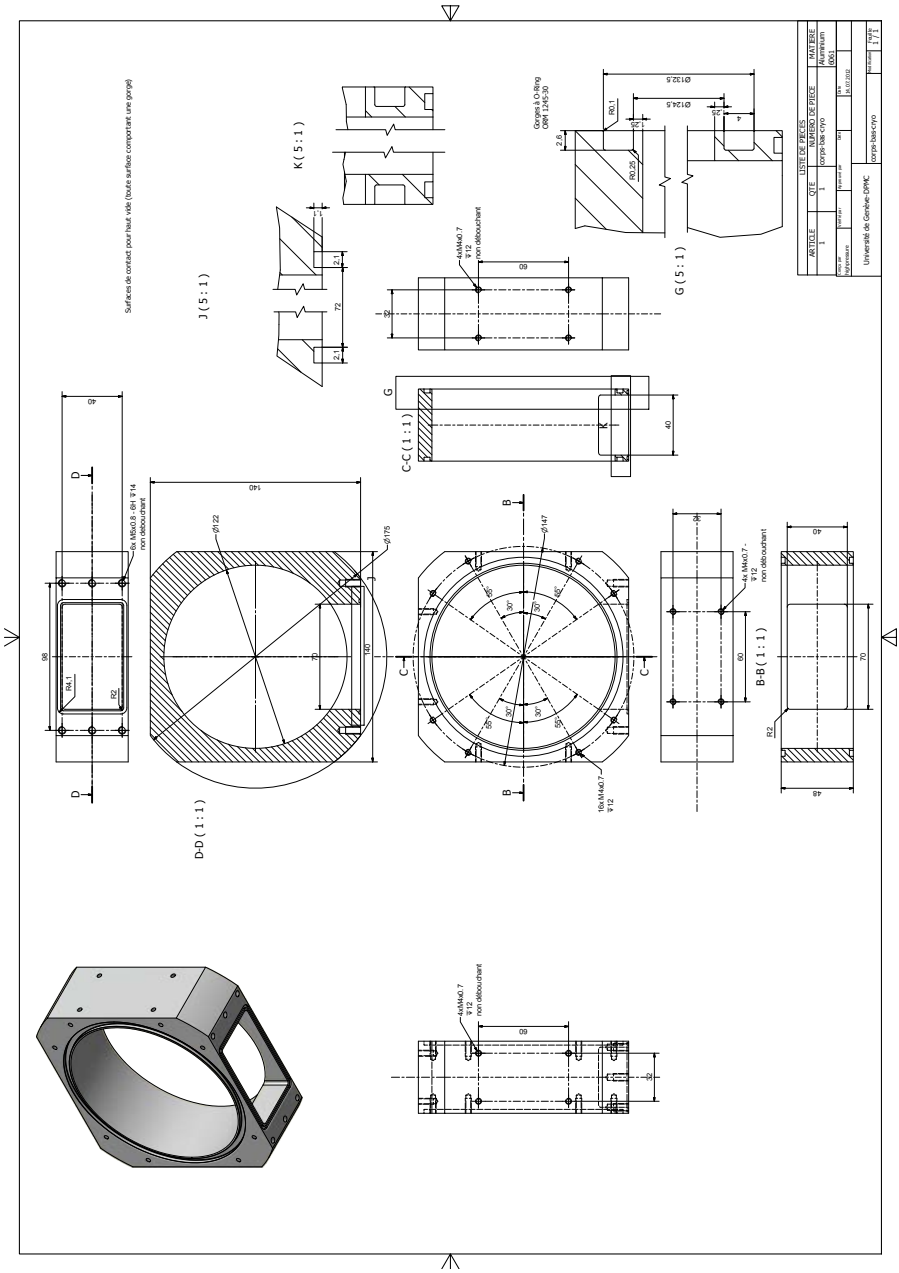
Surfaces de contact pour haut vide (toute surface comportant une gorge)
J (5 : 1)
K (5 : 1)
G (5 : 1)
C-C (1 : 1)
D-D (1 : 1)
B-B (1 : 1)
Gorge à O-Ring
ODM 124/5.30
6xM4x0.7
↧12
non débouchant
16xM4x0.7
↧12
6x M4x0.7 -
↧12
non débouchant
Ø132.8
Ø124.5
R0.1
R0.25
2.8
4
10
90°
2.1
72
60
32
40
140
Ø122
Ø175
Ø147
98
84.1
R2
70
48
45°
30°
55°
25°
LISTE DE PIECES
NUMERO DE PIECE
MATERIE
ARTICLE
QTE
1
corps-bas-cryo
Aluminium
6061
Université de Genève-DPMC
corps-bas-cryo
échelle
1 / 1.1

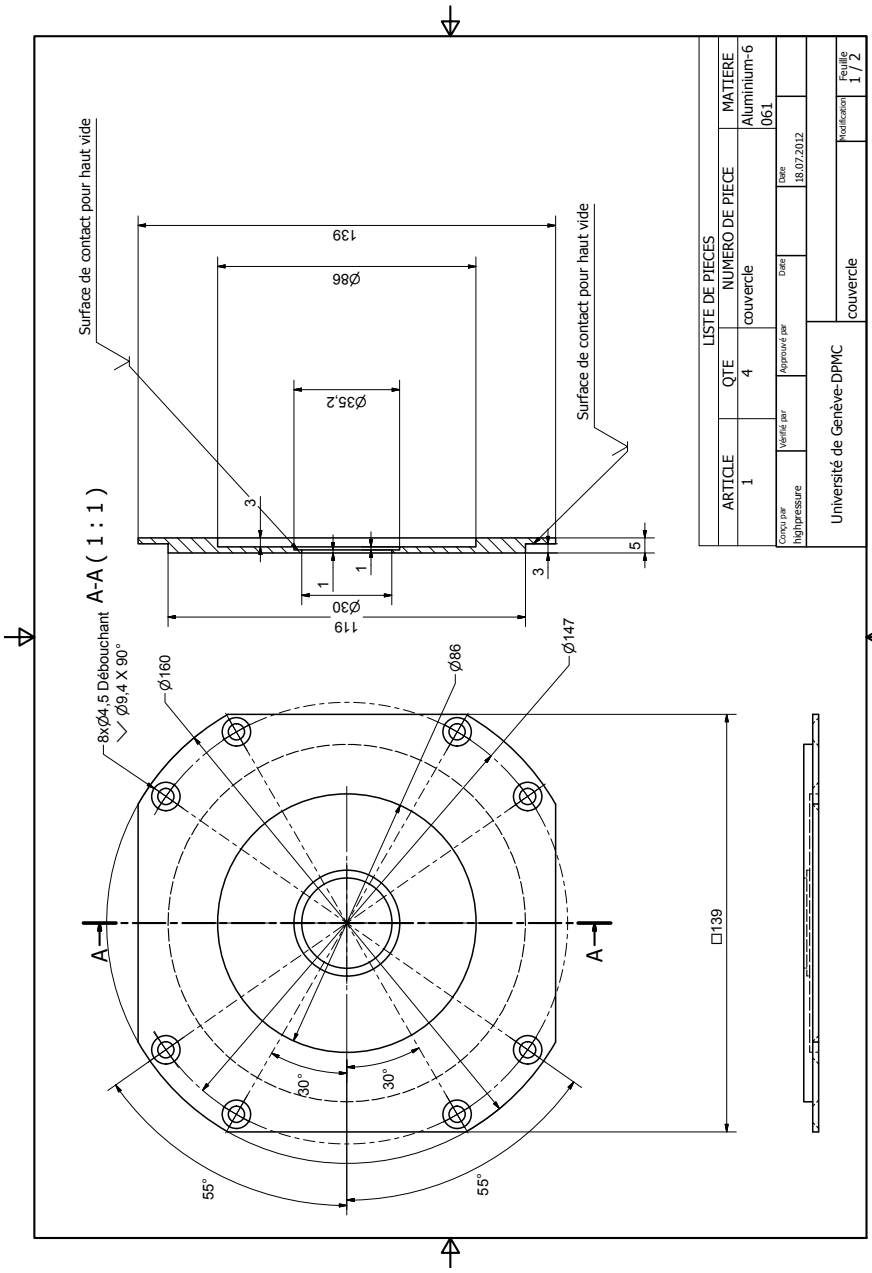
Surface de contact pour haut vide
Surface de contact pour haut vide
A-A (1 : 1)
8xØ4.5 Débouchant
Ø9.4 X 90°
Ø160
Ø86
Ø147
Ø35.2
Ø86
Ø30
139
119
□139
55°
55°
30°
30°
LISTE DE PIECES
ARTICLE
QTE
NUMERO DE PIECE
MATIERE
1
4
couvercle
Aluminium-6061
Conçu par highpressure
Vérifié par
Approuvé par
Date
18.07.2012
Université de Genève-DPMC
couvercle
Modification
Feuille 1 / 2

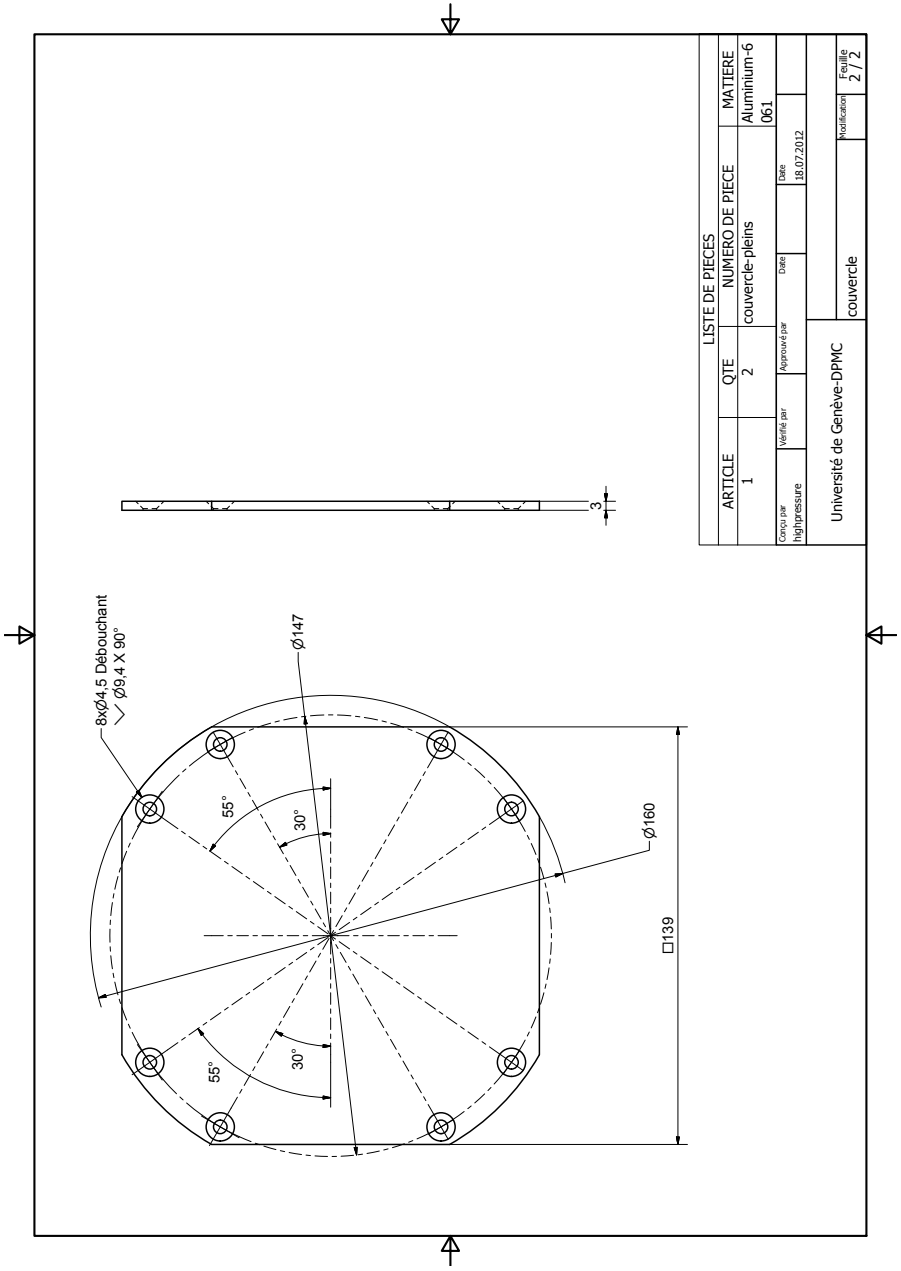
LISTE DE PIECES
ARTICLE
QTE
NUMERO DE PIECE
MATIERE
1
2
couvercle-pleins
Aluminium-6
061
Conçu par highpressure
Vérifié par
Approuvé par
Date
18.07.2012
Université de Genève-DPMC
couvercle
Modification
Feuille 2 / 2
3
8xØ4.5 Débouchant
ØØ9.4 X 90°
Ø147
Ø160
□139
55°
30°
55°
30°

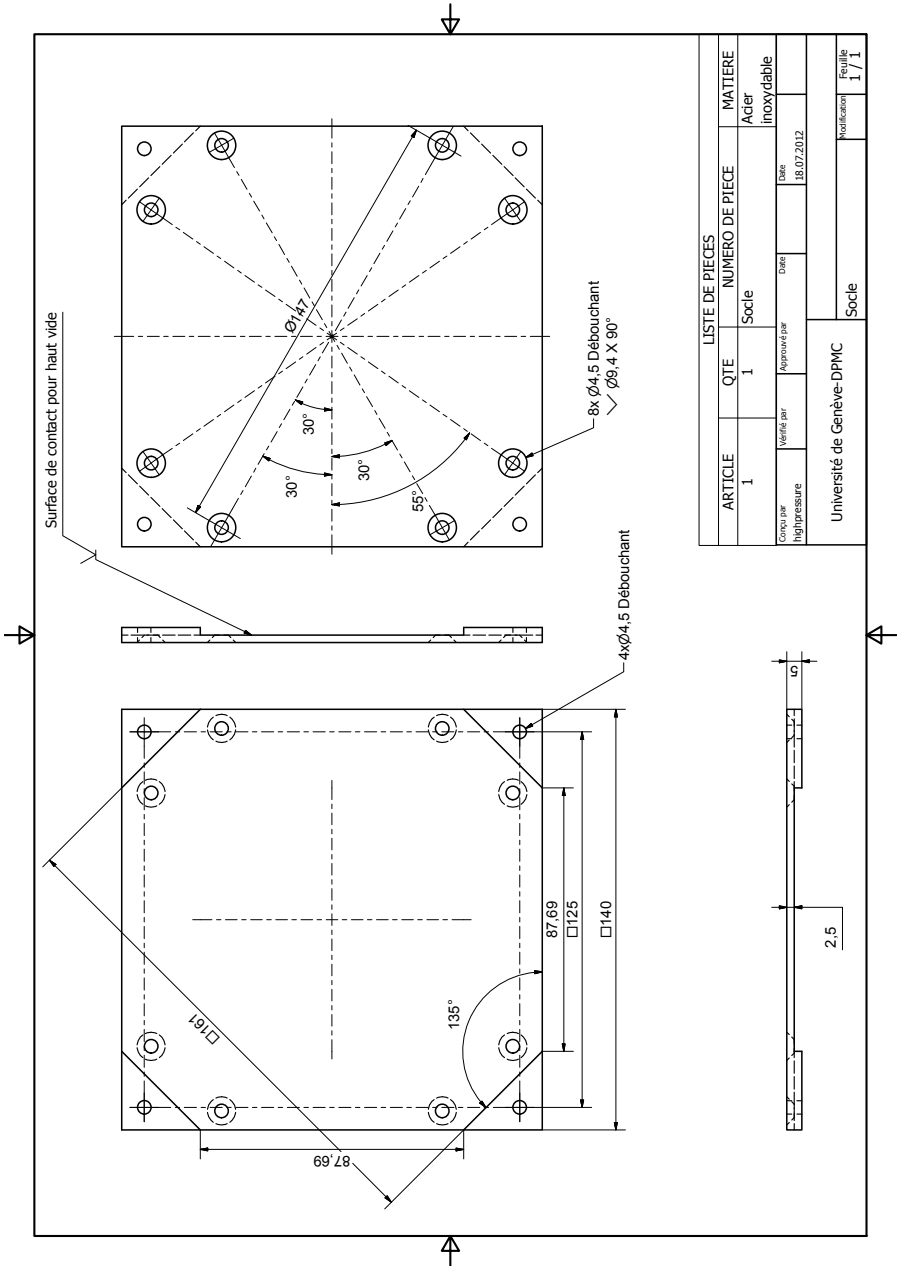
LISTE DE PIECES
ARTICLE
QTE
NUMERO DE PIECE
MATTERE
1
1
Socle
Acier inoxydable
Conçu par highpressure
Vérifié par
Approuvé par
Date
18.07.2012
Université de Genève-DPMC
Socle
Modification
Feuille 1 / 1
Surface de contact pour haut vide
Ø1H7
30°
30°
30°
55°
8x Ø4,5 Débouchant
Ø9,4 X 90°
4xØ4,5 Débouchant
□167
135°
87,69
□125
□140
87,69
5
2,5

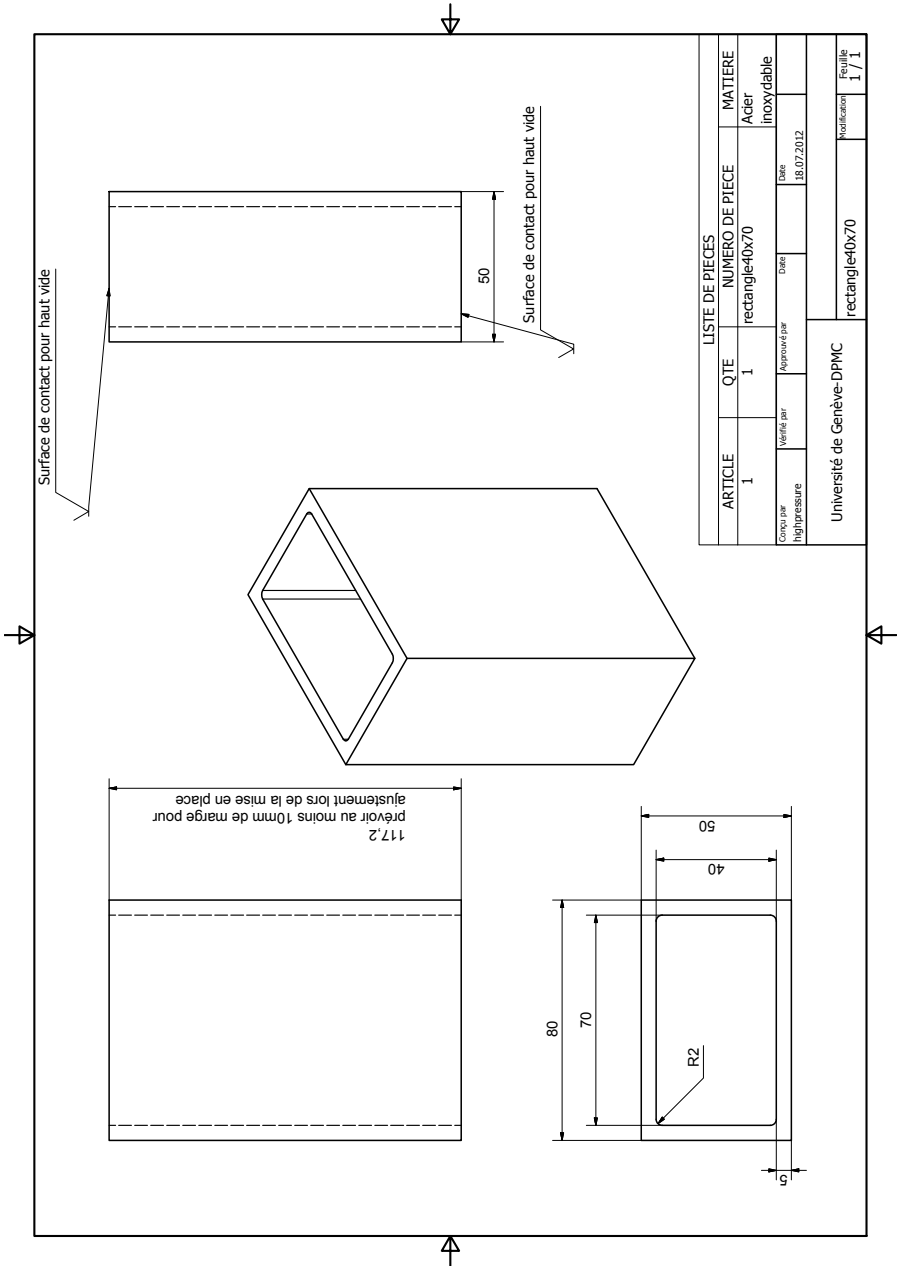
Surface de contact pour haut vide
50
Surface de contact pour haut vide
117.2
prévoir au moins 10mm de marge pour
ajustement lors de la mise en place
50
40
80
70
R2
5
LISTE DE PIECES
ARTICLE
QTE
NUMERO DE PIECE
MATTERE
1
1
rectangle40x70
Acier
inoxydable
Conçu par
highpressure
Vérifié par
Approuvé par
Date
Date
18.07.2012
Université de Genève-DPMC
rectangle40x70
Modification
Feuille
1 / 1

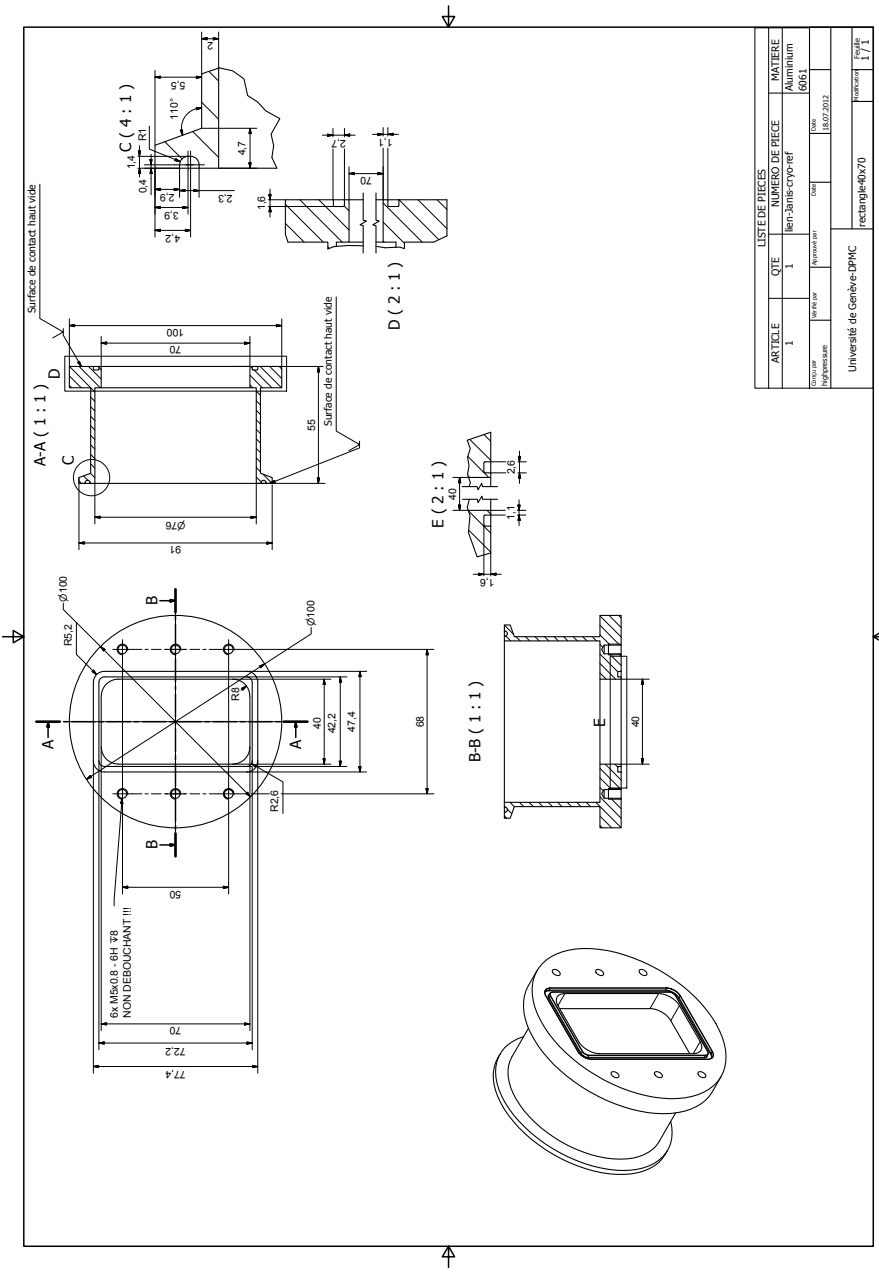
LISTE DE PIECES
ARTICLE | QTE | NUMERO DE PIECE | MATIERE
1 | 1 | lien-Janis-cryo-ref | Aluminium 6061
Université de Genève-DPMC
rectangle40x70
Feuille 1 / 1
C (4 : 1)
D (2 : 1)
A-A (1 : 1)
B-B (1 : 1)
E (2 : 1)
Surface de contact haut vide
6x M5x0.8 - 6H ↧8
NON DEBOUCHANT !!!
Ø100
R5.2
R8
R2.6

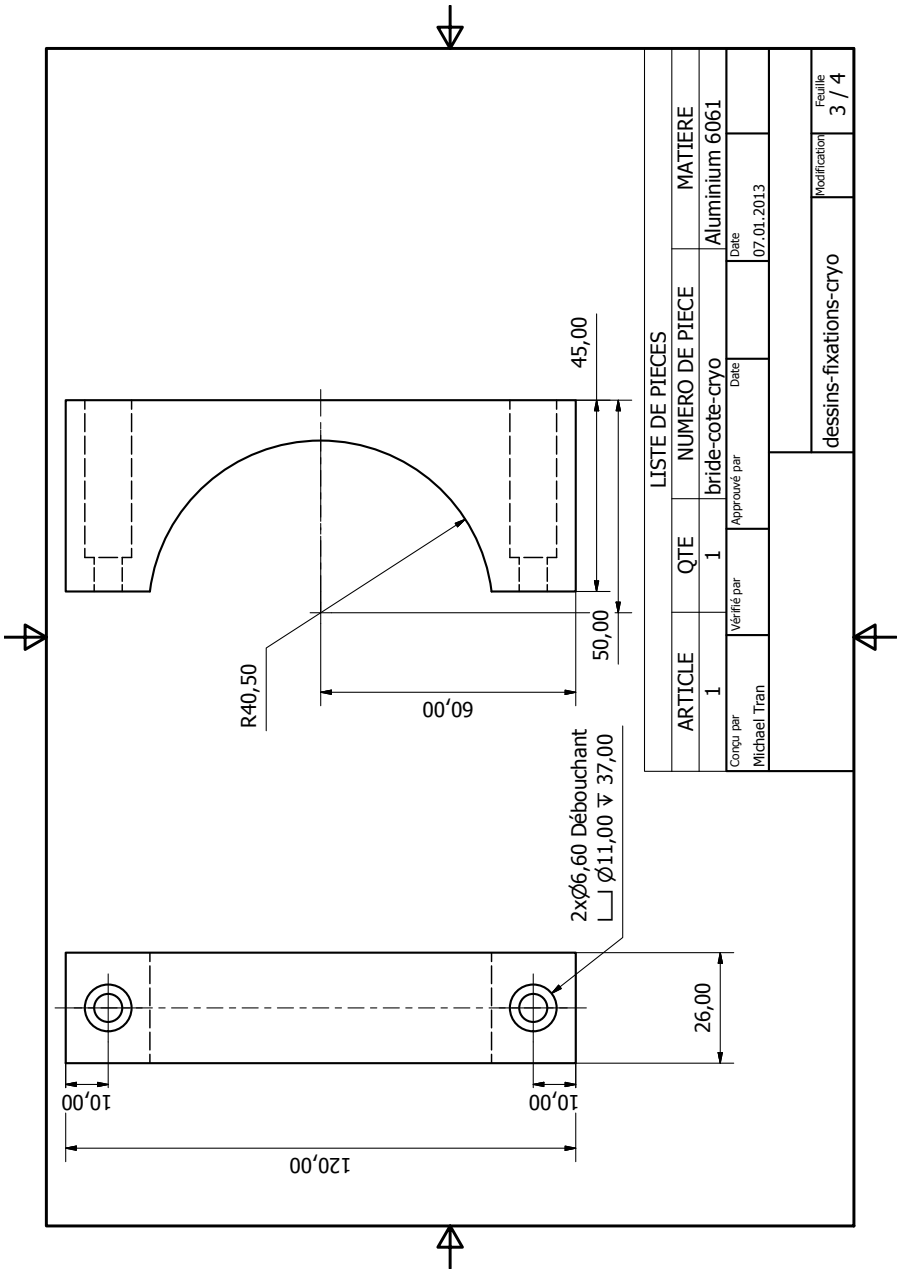
LISTE DE PIECES
ARTICLE
QTE
NUMERO DE PIECE
MATIERE
1
1
bride-cote-cryo
Aluminium 6061
Conçu par
Michael Tran
Vérifié par
Approuvé par
Date
07.01.2013
dessins-fixations-cryo
Modification
Feuille
3 / 4
45,00
50,00
R40,50
60,00
2xØ6,60 Débouchant
⌴ Ø11,00 ↧ 37,00
26,00
10,00
10,00
120,00

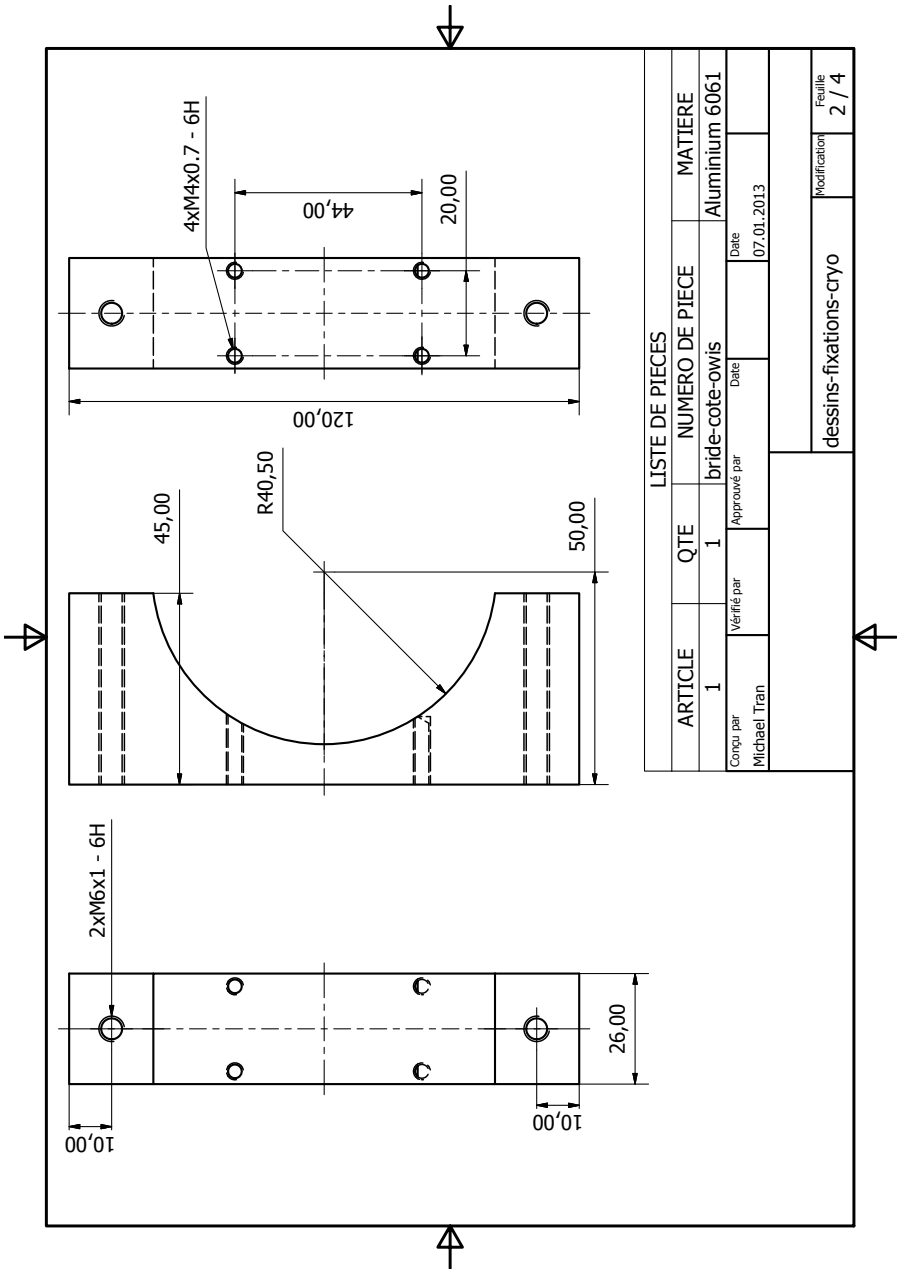
4xM4x0.7 - 6H
44,00
20,00
120,00
R40,50
45,00
50,00
2xM6x1 - 6H
10,00
26,00
10,00
LISTE DE PIECES
ARTICLE
QTE
NUMERO DE PIECE
MATIERE
1
1
bride-cote-owis
Aluminium 6061
Conçu par
Michael Tran
Vérifié par
Approuvé par
Date
07.01.2013
dessins-fixations-cryo
Modification
Feuille
2 / 4

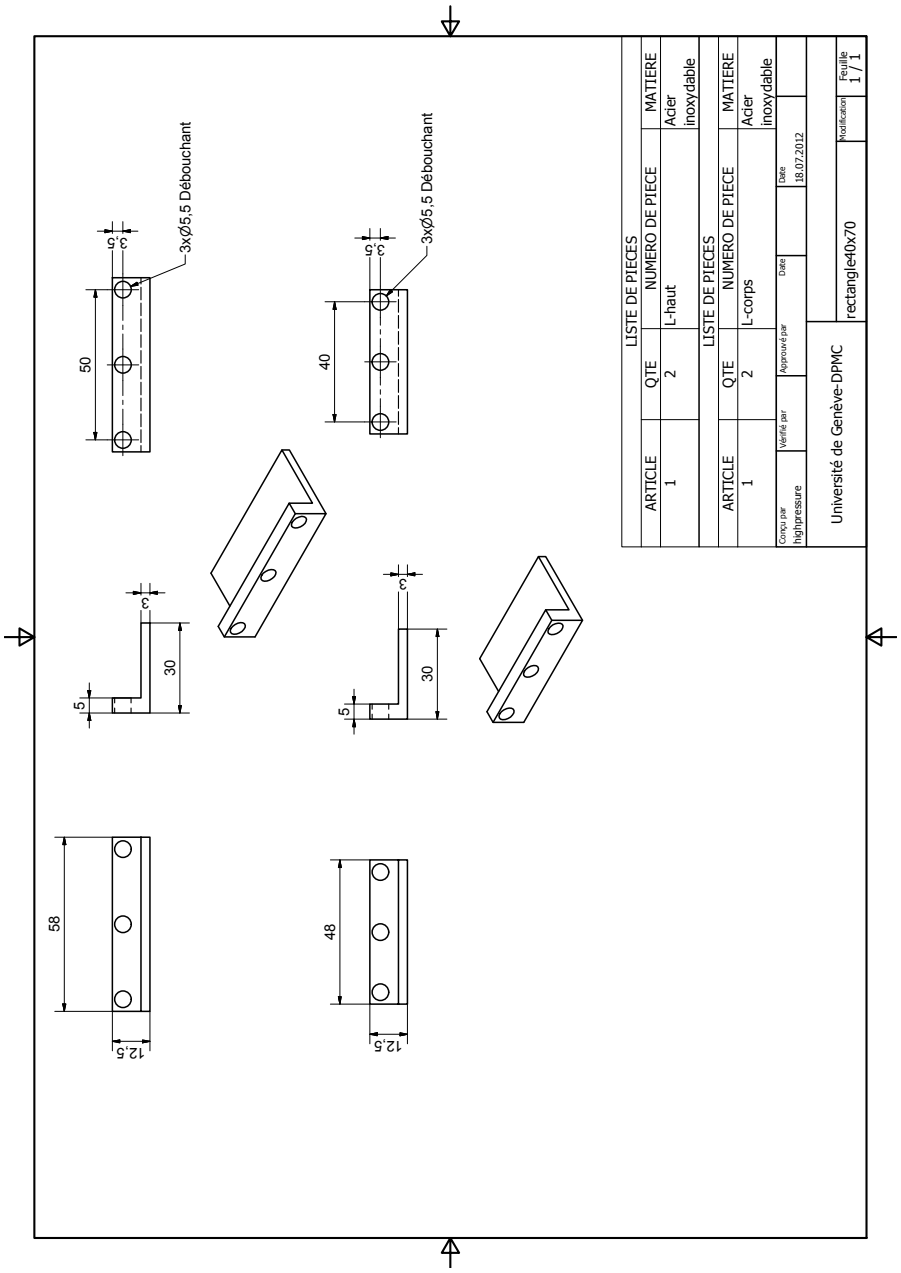
3xØ5,5 Débouchant
3xØ5,5 Débouchant
50
40
58
48
30
30
12,5
12,5
3
3
5
5
LISTE DE PIECES
ARTICLE
QTE
NUMERO DE PIECE
MATIERE
1
2
L-haut
Acier inoxydable
LISTE DE PIECES
ARTICLE
QTE
NUMERO DE PIECE
MATIERE
1
2
L-corps
Acier inoxydable
Conçu par highpressure
Vérifié par
Approuvé par
Date
18.07.2012
Université de Genève-DPMC
rectangle40x70
Modification
Feuille 1 / 1

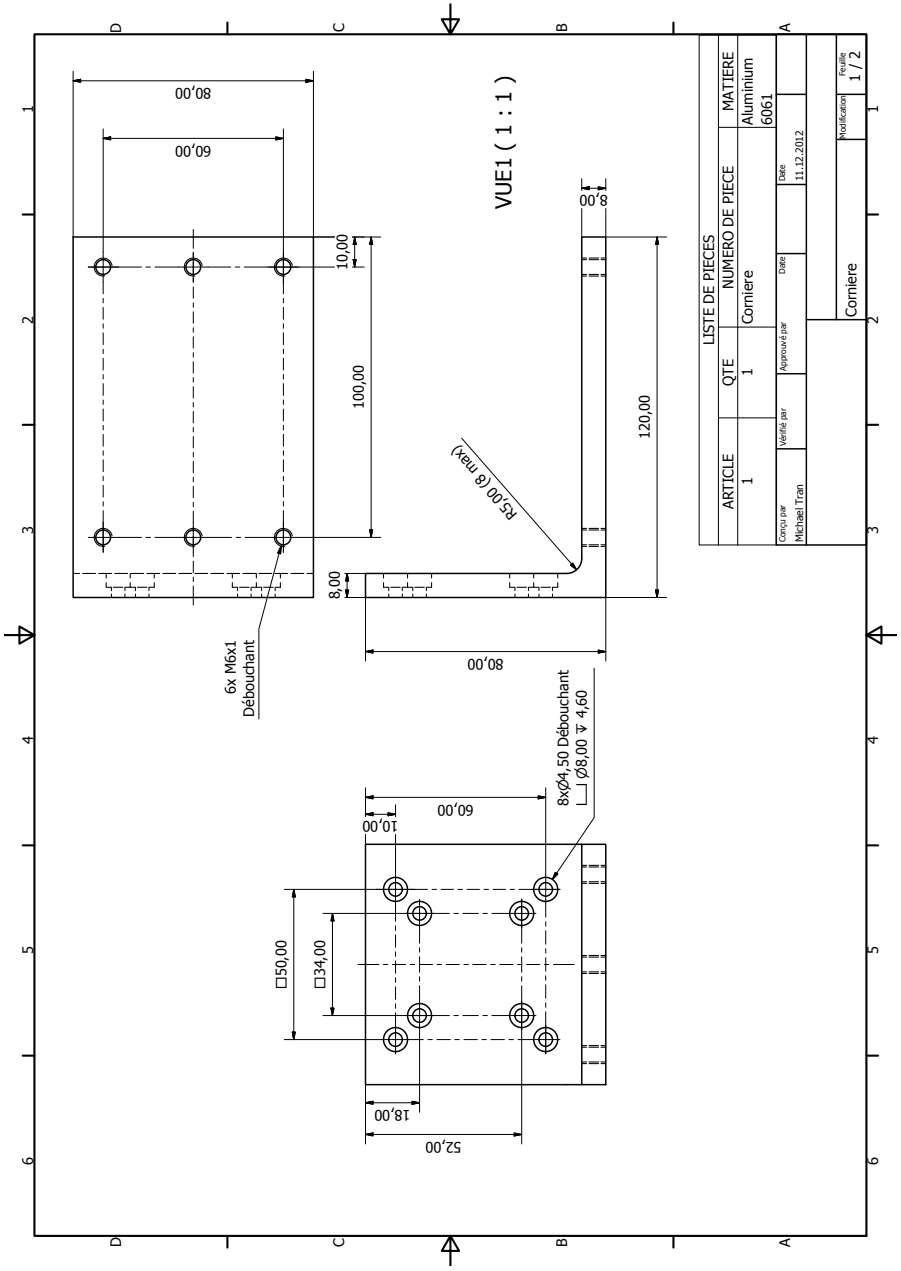
VUE1 (1 : 1)
80,00
60,00
10,00
100,00
120,00
8,00
R5,00 (8 max)
6x M6x1
Débouchant
8xØ4,50 Débouchant
⌴ Ø8,00 ↧ 4,60
□50,00
□34,00
18,00
52,00
LISTE DE PIECES
ARTICLE
NUMERO DE PIECE
QTE
MATIERE
Corniere
Aluminium 6061
Conçu par Michael Tran
Vérifié par
Approuvé par
Date 11.12.2012
Modification
Feuille 1 / 2

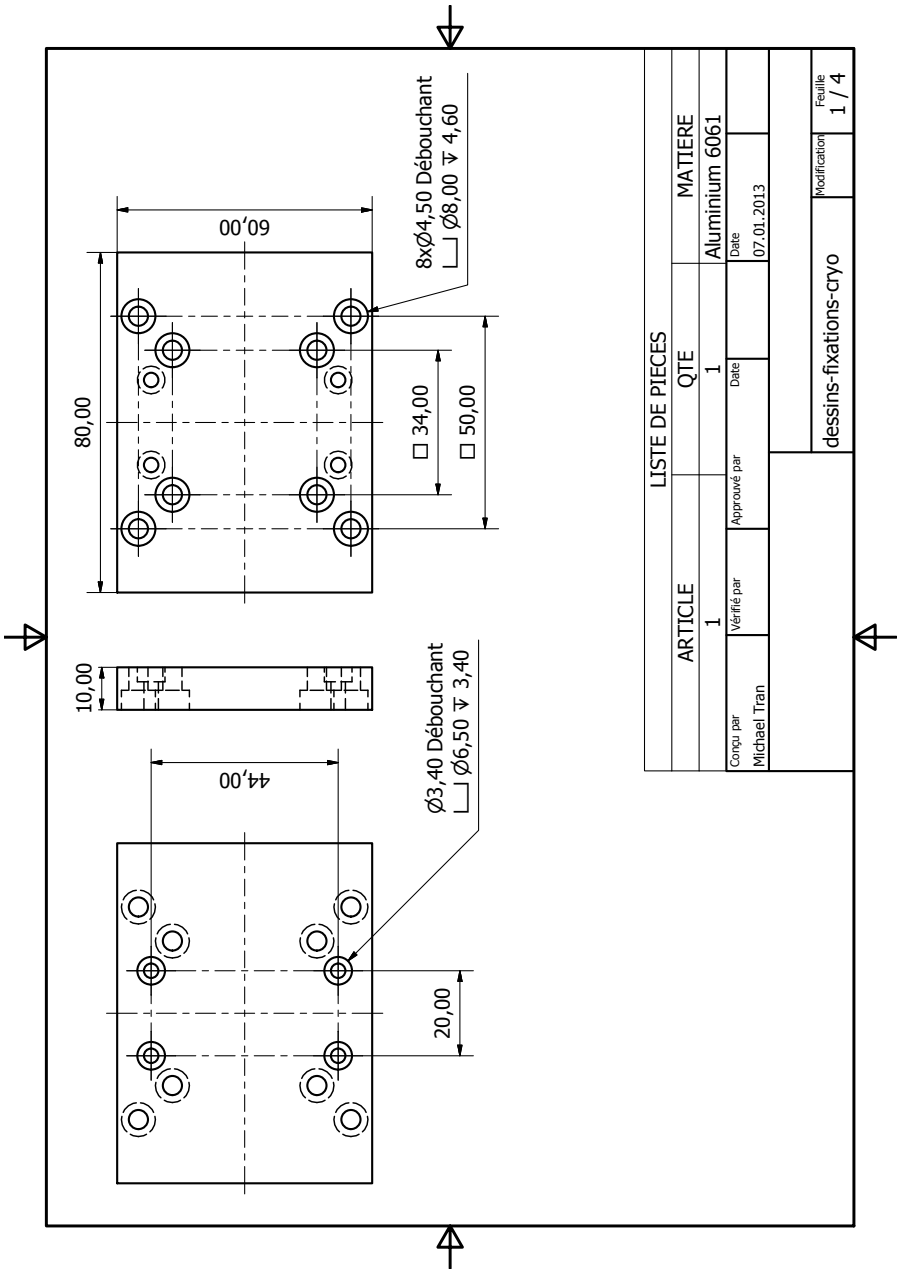
8xØ4,50 Débouchant
⌴ Ø8,00 ∓ 4,60
60,00
80,00
34,00
50,00
10,00
Ø3,40 Débouchant
⌴ Ø6,50 ∓ 3,40
44,00
20,00
LISTE DE PIECES
ARTICLE
QTE
MATIERE
1
1
Aluminium 6061
Conçu par
Michael Tran
Vérifié par
Approuvé par
Date
Date
07.01.2013
dessins-fixations-cryo
Modification
Feuille
1 / 4

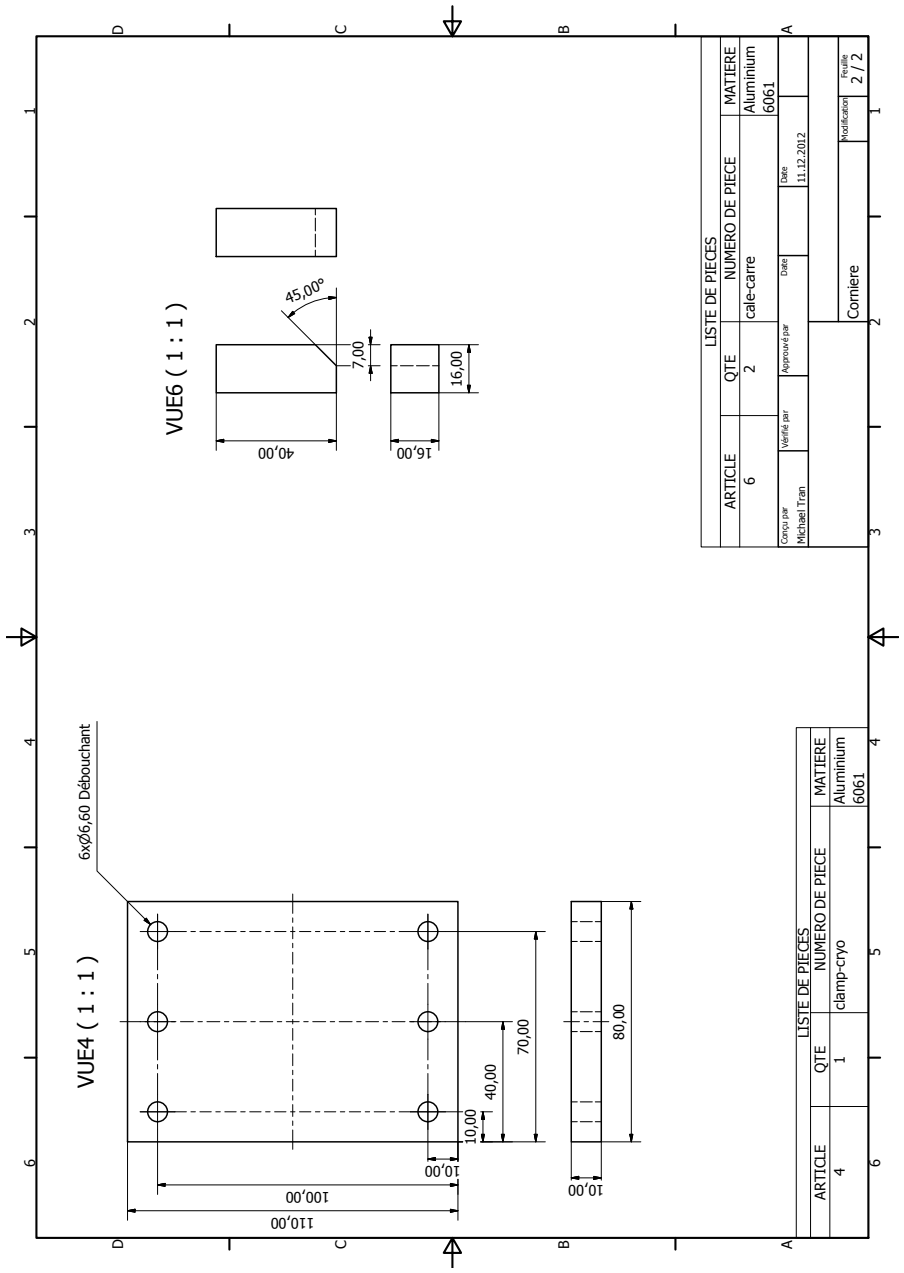
VUE4 (1 : 1)
6xØ6,60 Débouchant
110,00
100,00
10,00
10,00
40,00
70,00
10,00
80,00
VUE6 (1 : 1)
45,00°
7,00
16,00
40,00
16,00
LISTE DE PIECES
ARTICLE
NUMERO DE PIECE
QTE
MATIERE
4
clamp-cryo
1
Aluminium 6061
6
cale-carre
2
Aluminium 6061
Conçu par Michael Tran
Vérifié par
Approuvé par
Date
11.12.2012
Cornière
Modification
Feuille 2 / 2

Accepted and submitted Papers

[P1] P. Lerch, L. Quaroni, J. Wambach, J. Schneider, D. Armstrong, D. Rossetti, F. Mueller, P. Peier, V. Schlott, L. Carroll, P. Friedli, H. Sigg, S. Stutz, and M. Tran, *IR beamline at the Swiss Light Source*, J. Phys. Conf. Series **359**, 012003 (2012).

[P2] A. Akrap, M. Tran, A. Ubaldini, J. Teyssier, E. Giannini, D. van der Marel, P. Lerch, and C. C. Homes, *Optical properties of Bi_2Te_2Se at ambient and high pressures*, Phys. Rev. B **86**, 235207 (2012).

[P3] M.K. Tran, J. Levallois, P. Lerch, J. Teyssier, A.B. Kuzmenko, G. Autès, O.V. Yazyev, A. Ubaldini, E. Giannini, D. van der Marel, and A. Akrap, *Infrared- and Raman-Spectroscopy Measurements of a Transition in the Crystal Structure and a Closing of the Energy Gap of BiTeI under Pressure*, Phys. Rev. Lett. **112**, 047402 (2014).

[P4] J. Levallois, F. Lévy-Bertrand, M. K. Tran, D. Stricker, J. A. Mydosh, Y. K. Huang and D. van der Marel, *Hybridization gap and anisotropic far-infrared optical conductivity of URu_2Si_2*, Phys. Rev. B. **84**, 184420 (2011).

[P5] J. Levallois, M. K. Tran, and A. B. Kuzmenko, *Decrypting the cyclotron effect in graphite using Kerr rotation spectroscopy*, Solid State Communications **152**, 1294-1300 (2012).

References

[1] J. Berger and P. V. Santamaria, YAM-Le Magazine de Chefs (2013).

[2] T. Cuk, D. A. Zocco, H. Eisaki, V. Struzhkin, F. M. Grosche, M. B. Maple, and Z. X. Shen, Phys. Rev. B **81**, 184509 (2010).

[3] L. Gao, Y. Xue, F. Chen, Q. Xiong, R. Meng, D. Ramirez, C. Chu, J. Eggert, and H. Mao, Phys. Rev. B **50**, 4260 (1994).

[4] S. Frank, C. Kuntscher, I. Loa, K. Syassen, and F. Lichtenberg, Phys. Rev. B **74**, 054105 (2006).

[5] C. Marini, E. Arcangeletti, D. Di Castro, L. Baldassare, A. Perucchi, S. Lupi, L. Malavasi, L. Boeri, E. Pomjakushina, K. Conder, and P. Postorino, Phys. Rev. B **77**, 235111 (2008).

[6] B. Welber, P. Seiden, and P. Grant, Phys. Rev. B **18**, 2692 (1978).

[7] R. Tediosi, *Pressure Tuning of Low-energy Collective Excitations in Metals*, Ph.D. thesis, Université de Genève (2008).

[8] M. Dressel and G. Grüner, *Electrodynamics of Solids* (Cambridge University Press, Cambridge, 2001).

[9] D. J. Griffiths, *Introduction to electrodynamics* (MA : Pearson, Boston, 2013).

[10] M. Dressel, "Fourier-Transform Infrared Spectroscopy | Universität Stuttgart," .

[11] M. Dressel and N. Drichko, Chemical Reviews **104**, 5689 (2004).

[12] A. B. Kuzmenko, Rev. Sci. Instrum. **76**, 083108 (2005).

[13] A. B. Kuzmenko, *Guide to Reffit: software to fit optical spectra* (2004).

[14] Almax-Easylab, "Type IIac Standard design," .

[15] Diamond Materials, "The CVD Diamond booklet," .

[16] H. Okamura, Journal of Physics: Conference Series **359**, 012013 (2012).

[17] H. Okamura, M. Matsunami, R. Kitamura, S. Ishida, A. Ochiai, and T. Nanba, Journal of Physics: Conference Series **215**, 012051 (2010).

[18] W. A. Bassett, High Pressure Research **29**, 163 (2009).

[19] D. J. Dunstan and I. L. Spain, J. Phys. E: Sci. Instrum. **22**, 913 (1989).

[20] I. L. Spain and D. J. Dunstan, J. Phys. E: Sci. Instrum. **22**, 923 (1989).

[21] M. K. Tran, *Développement d'une cellule de pression pour des mesures optiques dans l'Infrarouge*, Master's thesis, Université de Genève (2009).

[22] R. Letoullec, J. P. Pinceaux, and P. Loubeyre, High Pres. Res. **1**, 77 (1988).

[23] R. L. Smith Jr. and Z. Fang, The Journal of Supercritical Fluids **47**, 431 (2009).

[24] BETSA France, "Membrane Diamond Anvil Cell MDAC-XHP(sc)," (2008).

[25] K. Murata, K. Yokogawa, H. Yoshino, S. Klotz, P. Munsch, A. Irizawa, M. Nishiyama, K. Iizuka, T. Nanba, T. Okada, Y. Shiraga, and S. Aoyama, Rev. Sci. Instrum. **79**, 085101 (2008).

[26] M. I. Eremets, *High Pressure Experimental Methods* (Oxford University Press, 1996).

[27] Goodfellow, "Cuivre/Béryllium - Feuille," .

[28] "UHU patafix gluepads," .

[29] BETSA France, *Motorized Electric Discharge Machine (EDM) MH20M*.

[30] *Pneumatic Drive System for the MDAC high pressure cell: PDS 200*, BETSA France.

[31] Swagelok, "Quick-Connects," (2013).

[32] F. Datchi, A. Dewaele, P. Loubeyre, R. Letoullec, Y. Le Godec, and B. Canny, High Pres. Res. **27**, 447 (2007).

[33] F. Occelli, Ph.D. thesis, Université Pierre et Marie Curie (Paris~VI) and CEA (2002).

[34] Bruker Optics GmbH, *IFS 66v/S User's Manual*, Bruker Optics (1997).

[35] P. Lerch, L. Quaroni, J. Wambach, J. Schneider, D. B. Armstrong, D. Rossetti, F. L. Mueller, P. Peier, V. Schlott, L. Carroll, P. Friedli, H. Sigg, S. Stutz, and M. Tran, J. Phys. Conf. Series **359**, 012003 (2012).

[36] Bruker Optics GmbH, *HYPERION Series*, FT-IR Microscopes (2013).

[37] S. Soleil, "Le rayonnement synchrotron pour l'industrie," .

[38] D. Cannavo and L. Degiorgi, *Project for an infrared-beamline at the Swiss Light Source*, Tech. Rep. (2000).

[39] D. Lu, I. M. Vishik, M. Yi, Y. Chen, R. G. Moore, and Z.-X. Shen, Annual Review of Condensed Matter Physics **3**, 129 (2012).

[40] E. H. Hall, American Journal of Mathematics **2**, pp. 287 (1879).

[41] E. H. Hall, Phil. Mag. **12**, 157 (1881).

[42] S. P. P. m. b. C. o. e. O. work, "Hall effect A," .

[43] C. Day, Physics Today **61**, 19 (2008).

[44] K. Klitzing, G. Dorda, and M. Pepper, Physical Review Letters **45**, 494 (1980).

[45] B. A. Bernevig and T. L. Hughes, Science **314**, 1757 (2006).

[46] M. Konig, S. Wiedmann, C. Brune, A. Roth, H. Buhmann, L. W. Molenkamp, X. L. Qi, and S. C. Zhang, Science **318**, 766 (2007).

[47] J. Maciejko, T. L. Hughes, and S.-C. Zhang, Annual Review of Condensed Matter Physics **2**, 31 (2011).

[48] L. Fu and C. Kane, Phys. Rev. B **76**, 045302 (2007).

[49] D. Hsieh, Y. Xia, L. Wray, D. Qian, A. Pal, J. H. Dil, J. Osterwalder, F. Meier, G. Bihlmayer, C. L. Kane, Y. S. Hor, R. J. Cava, and M. Z. Hasan, Science **323**, 919 (2009).

[50] Y. L. Chen, J. G. Analytis, J. H. Chu, Z. K. Liu, S. K. Mo, X. L. Qi, H. J. Zhang, D. H. Lu, X. Dai, Z. Fang, S. C. Zhang, I. R. Fisher, Z. Hussain, and Z. X. Shen, Science **325**, 178 (2009).

[51] E. Dönges, Zeitschrift für anorganische und allgemeine Chemie **265**, 56 (1951).

[52] J. Horak, Journal de Physique **31**, 121 (1970).

[53] K. Ishizaka, M. S. Bahramy, H. Murakawa, M. Sakano, T. Shimojima, T. Sonobe, K. Koizumi, S. Shin, H. Miyahara, A. Kimura, K. Miyamoto, T. Okuda, H. Namatame, M. Taniguchi, R. Arita, N. Nagaosa, K. Kobayashi, Y. Murakami, R. Kumai, Y. Kaneko, Y. Onose, and Y. Tokura, Nature Mat. **10**, 521 (2011).

[54] M. S. Bahramy, B.-J. Yang, R. Arita, and N. Nagaosa, Nature Comm. **3**, 679 (2012).

[55] A. V. Shevelkov, E. V. Dikarev, R. V. Shpanchenko, and B. A. Popovkin, Journal of Solid State Chemistry **114**, 379 (1995).

[56] E. I. RASHBA, SOVIET PHYSICS-SOLID STATE **2**, 1109 (1960).

[57] Y. A. BYCHKOV and E. I. RASHBA, Jetp Letters **39**, 78 (1984).

[58] J. Sinova, D. Culcer, Q. Niu, N. Sinitsyn, T. Jungwirth, and A. MacDonald, Physical Review Letters **92**, 126603 (2004).

[59] A. Crepaldi, L. Moreschini, G. Autès, C. Tournier-Colletta, S. Moser, N. Virk, H. Berger, P. Bugnon, Y. J. Chang, K. Kern, A. Bostwick, E. Rotenberg, O. V. Yazyev, and M. Grioni, Physical Review Letters **109**, 096803 (2012).

[60] G. Landolt, S. V. Eremeev, Y. M. Koroteev, B. Slomski, S. Muff, T. Neupert, M. Kobayashi, V. N. Strocov, T. Schmitt, Z. S. Aliev, M. B. Babanly, I. R. Amiraslanov, E. V. Chulkov, J. Osterwalder, and J. H. Dil, Physical Review Letters **109**, 116403 (2012).

[61] J. S. Lee, G. A. H. Schober, M. S. Bahramy, H. Murakawa, Y. Onose, R. Arita, N. Nagaosa, and Y. Tokura, Physical Review Letters **107**, 117401 (2011).

[62] I. Y. Sklyadneva, R. Heid, K. P. Bohnen, V. Chis, V. A. Volodin, K. A. Kokh, O. E. Tereshchenko, P. M. Echenique, and E. V. Chulkov, Phys. Rev. B **86**, 094302 (2012).

[63] V. Gnezdilov, D. Wulferding, P. Lemmens, A. Möller, P. Recher, H. Berger, R. Sankar, and F. C. Chou, arXiv:1303.4333 (2013).

[64] D. Hsieh, L. Wray, A. Pal, H. Lin, A. Bansil, D. Grauer, Y. S. Hor, R. J. Cava, and M. Z. Hasan, Nature Phys. **5**, 398 (2009).

[65] H. Zhang, C.-X. Liu, X.-L. Qi, X. Dai, Z. Fang, and S.-C. Zhang, Nature Phys. **5**, 438 (2009).

[66] S.-Y. Xu, L. A. Wray, S. Jia, F. Meier, J. H. Dil, J. Osterwalder, B. Slomski, A. Bansil, H. Lin, R. J. Cava, and M. Z. Hasan, Science **332**, 560 (2011).

[67] T. Sato, K. Segawa, K. Kosaka, S. Souma, K. Nakayama, K. Eto, T. Minami, Y. Ando, and T. Takahashi, Nature Phys. **7**, 840 (2011).

[68] M. Brahlek, N. Bansal, N. Koirala, S.-Y. Xu, M. Neupane, C. Liu, M. Z. Hasan, and S. Oh, Physical Review Letters **109**, 186403 (2012).

[69] C. Martin, K. H. Miller, S. Buvaev, H. Berger, X. S. Xu, A. F. Hebard, and D. B. Tanner, arXiv:1209.1656 (2012).

[70] L. Demkó, G. A. H. Schober, V. Kocsis, M. S. Bahramy, H. Murakawa, J. S. Lee, I. Kézsmárki, R. Arita, N. Nagaosa, and Y. Tokura, Physical Review Letters **109**, 167401 (2012).

[71] A. Akrap, M. K. Tran, A. Ubaldini, J. Teyssier, E. Giannini, D. van der Marel, P. Lerch, and C. C. Homes, Phys. Rev. B **86**, 235207 (2012).

[72] X. Xi, C. Ma, Z. Liu, Z. Chen, W. Ku, H. Berger, C. Martin, D. B. Tanner, and G. L. Carr, Physical Review Letters **111**, 155701 (2013).

[73] Y. Chen, X. Xi, W.-L. Yim, F. Peng, Y. Wang, H. Wang, Y. Ma, G. Liu, C. Sun, C. Ma, Z. Chen, and H. Berger, The Journal of Physical Chemistry C **117**, 25677 (2013).

[74] Y. S. Ponosov, T. V. Kuznetsova, O. E. Tereshchenko, K. A. Kokh, and E. V. Chulkov, Jetp Letters **98**, 557 (2014).

[75] I. P. Rusinov, I. A. Nechaev, S. V. Eremeev, C. Friedrich, S. Bl ugel, and E. V. Chulkov, Phys. Rev. B **87**, 205103 (2013).

[76] O. V. Yazyev, E. Kioupakis, J. E. Moore, and S. G. Louie, Phys. Rev. B **85**, 161101 (2012).

[77] M. K. Tran, J. Levallois, P. Lerch, J. Teyssier, A. B. Kuzmenko, G. Autès, O. V. Yazyev, A. Ubaldini, E. Giannini, D. van der Marel, and A. Akrap, Physical Review Letters **112**, 047402 (2014).

[78] X. Xi, C. Ma, Z. Liu, Z. Chen, W. Ku, H. Berger, C. Martin, D. B. Tanner, and G. L. Carr, arXiv:1305.0959 (2013).

[79] D. VanGennep, S. Maiti, D. Graf, S. W. Tozer, C. Martin, H. Berger, D. L. Maslov, and J. J. Hamlin, Journal of Physics: Condensed Matter **26**, 342202 (2014).

[80] M. Z. Hasan and C. L. Kane, Rev. Mod. Phys. **82**, 3045 (2010).

[81] M. Greenblatt, Chemical Reviews **88**, 31 (1988).

[82] W. H. McCarroll and M. Greenblatt, Journal of Solid State Chemistry **54**, 282 (1984).

[83] M. Greenblatt, W. H. McCarroll, R. Neifeld, M. Croft, and J. V. Waszczak, Solid State Communications **51**, 671 (1984).

[84] M. Onoda, K. Toriumi, Y. Matsuda, and M. Sato, Journal of Solid State Chemistry **66**, 163 (1987).

[85] C. Jacobsen, D. Tanner, and K. Bechgaard, Physical Review Letters **46**, 1142 (1981).

[86] A. Schwartz, M. Dressel, G. Grüner, V. Vescoli, and L. Degiorgi, Phys. Rev. B **58**, 1261 (1998).

[87] C. E. Filippini, J. Beille, M. Boujida, and J. Marcus, Physica C: ... **162-164**, 427 (1989).

[88] B. Sipos, A. F. Kusmartseva, A. Akrap, H. Berger, and L. Forro, Nature materials **7**, 960 (2008).

[89] C. Berthod, T. Giamarchi, S. Biermann, and A. Georges, Physical Review Letters **97**, 136401 (2006).

[90] P. Chudzinski, T. Jarlborg, and T. Giamarchi, Phys. Rev. B **86**, 075147 (2012).

[91] C. dos Santos, B. White, Y.-K. Yu, J. Neumeier, and J. Souza, Physical Review Letters **98**, 266405 (2007).

[92] H. J. I. Filho, J. B. Le ao, and Q. Huang, Phys. Rev. B **84**, 014108 (2011).

[93] J. L. Cohn, P. Boynton, J. S. Triviño, J. Trastoy, B. D. White, C. A. M. dos Santos, and J. J. Neumeier, Phys. Rev. B **86**, 195143 (2012).

[94] J. F. Mercure, A. F. Bangura, X. Xu, N. Wakeham, A. Carrington, P. Walmsley, M. Greenblatt, and N. E. Hussey, Physical Review Letters **108**, 187003 (2012).

[95] T. Giamarchi, *Quantum physics in one dimension*, Internat. Ser. Mono. Phys. (Clarendon Press, Oxford, 2004).

[96] T. Jarlborg, P. Chudzinski, and T. Giamarchi, Phys. Rev. B **85**, 235108 (2012).

[97] J. Schlappa, K. Wohlfeld, K. J. Zhou, M. Mourigal, M. W. Haverkort, V. N. Strocov, L. Hozoi, C. Monney, S. Nishimoto, S. Singh, A. Revcolevschi, J. S. Caux, L. Patthey, H. M. Rønnow, J. van den Brink, and T. Schmitt, Nature **485**, 82 (2012).

[98] C. Kim, A. Matsuura, Z. X. Shen, N. Motoyama, H. Eisaki, S. Uchida, T. Tohyama, and S. Maekawa, Physical Review Letters **77**, 4054 (1996).

[99] B. J. Kim, H. Koh, E. Rotenberg, S. J. Oh, H. Eisaki, N. Motoyama, S. Uchida, T. Tohyama, S. Maekawa, and C. Kim, Nature Physics **2**, 397 (2006).

[100] S.-i. TOMONAGA, "Remarks on Bloch's Method of Sound Waves applied to Many-Fermion Problems," (1950).

[101] J. M. Luttinger, Journal of Mathematical Physics **4**, 1154 (1963).

[102] D. Orgad, Philosophical Magazine Part B **81**, 377 (2001).

[103] J. A. Hertz, Physical Review **B14**, 1165 (1976).

[104] S. Sachdev, *Quantum Phase Transitions* (Cambridge University Press, 2011).

[105] M. H. Whangbo and E. Canadell, Journal of the American Chemical Society **110**, 358 (1988).

[106] Z. Popović and S. Satpathy, Phys. Rev. B **74**, 045117 (2006).

[107] J. Denlinger, G. H. Gweon, J. W. Allen, C. Olson, J. Marcus, C. Schlenker, and L. S. Hsu, Physical Review Letters **82**, 2540 (1999).

[108] F. Wang, J. Alvarez, J. W. Allen, S. K. Mo, J. He, R. Jin, D. Mandrus, and H. Höchst, Physical Review Letters **103**, 136401 (2009).

[109] L. Dudy, J. D. Denlinger, J. W. Allen, F. Wang, J. He, D. Hitchcock, A. Sekiyama, and S. Suga, Journal of Physics: Condensed Matter **25**, 014007 (2012).

[110] G. Travaglini and P. Wachter, Phys. Rev. B **30**, 1971 (1984).

[111] J. Xue, L. C. Duda, K. Smith, A. Fedorov, P. Johnson, S. Hulbert, W. McCarroll, and M. Greenblatt, Physical Review Letters **83**, 1235 (1999).

[112] L. Degiorgi, P. Wachter, M. Greenblatt, W. H. McCarroll, K. V. Ramanujachary, J. Marcus, and C. Schlenker, Phys. Rev. B **38**, 5821 (1988).

[113] J. Choi, J. L. Musfeldt, J. He, R. Jin, J. R. Thompson, D. Mandrus, X. N. Lin, V. A. Bondarenko, and J. W. Brill, Phys. Rev. B **69**, 085120 (2004).

[114] J. Levallois, F. Lévy-Bertrand, M. K. Tran, D. Stricker, J. A. Mydosh, Y. K. Huang, and D. van der Marel, Phys. Rev. B **84**, 184420 (2011).

[115] J. Levallois, M. K. Tran, and A. B. Kuzmenko, Solid State Communications **152**, 1294 (2012).